Die approbierte Originalversion dieser Dissertation ist in der Hauptbibliothek der Technischen Universität Wien aufgestellt und zugänglich.
http://www.ub.tuwien.ac.at

The approved original version of this thesis is available at the main library of the Vienna University of Technology.
http://www.ub.tuwien.ac.at/eng

TECHNISCHE UNIVERSITÄT WIEN
Vienna University of Technology

ATOMINSTITUT
INSTITUTE OF ATOMIC AND SUBATOMIC PHYSICS
www.ati.ac.at

DISSERTATION

PHONON COOLING AND LASING WITH DEFECT CENTERS IN DIAMOND NANORESONATORS

ausgeführt zum Zwecke der Erlangung des akademischen Grades eines Doktors der Naturwissenschaften unter der Leitung von

ASS. PROF. DR. PETER RABL
E141
Atominsitut

eingereicht an der Technischen Universität Wien
Fakultät für Physik

von

KOSMAS KEPESIDIS, M.SC.
(Matrikelnummber: 1227528)
Erich-Klausener-Straße 11,
40474 Düsseldorf, Deutschland

Wien, am 00.00.2017 ....

Diese Dissertation haben begutachtet:

Prof. Dr. G. Morigi Prof. Dr. K. Hammerer

....

Phonon cooling and lasing with defect centers in diamond nanoresonators

Dissertation

KOSMAS KEPESIDIS, M.SC.

TECHNISCHE UNIVERSITÄT WIEN

©2016 – Kosmas Kepesidis
all rights reserved.

TO MY FAMILY

ABSTRACT

This doctoral thesis investigates potential phonon-cooling and phonon-lasing schemes as well as quantum applications with diamond nano-mechanical resonators also known as *phonon cavities*. These particular schemes are for the first time based on the exploitation of the multi-level energy structure of diamond's natural defects such as nitrogen-vacancy and silicon-vacancy centers. We develop microscopic models for defect-phonon interactions and use various quantum optical methods to explore different laser manipulation schemes under realistic experimental conditions. In particular, we investigate the strain-induced coupling between a nitrogen-vacancy impurity and resonant vibrational modes of diamond nano-mechanical resonators. This coupling can modify the state of the resonator and either cool a vibrational mode close to the quantum ground state or excite it into a large-amplitude coherent state, a phenomenon known as *phonon lasing*. In addition, we study a setup where a silicon-vacancy center is magnetically coupled to a low-frequency mechanical bending mode and via strain to the continuum of high-frequency longitudinal modes of a singly-clamped diamond beam. This setup can be used to induce cooling effects for the low-frequency mechanical vibrations, where the high-frequency longitudinal compression modes of the beam serve as an intrinsic low-temperature reservoir.

A natural extension of the above-described setups is a system of two-coupled resonators. Assuming that one of the oscillators is cooled and the other is heated with the same rate, such a gain-loss system offers an ideal setup for investigating the physics of so-called *parity-time-symmetric* systems, under realistic conditions. Specifically, we present a new type of parity-time-symmetry breaking, which occurs in the steady-state energy distribution of classical (and open quantum) systems with balanced gain and loss. We show that the combination of non-linear saturation effects and the presence of thermal or quantum noise in actual experiments results in unexpected behavior that differs significantly from the usual dynamical picture. We observe additional phases with preserved or broken parity-time symmetry as well as a transition from a very noisy thermal state to a low-energy lasing state with strongly reduced fluctuations.

ZUSAMMENFASSUNG

In dieser Doktorarbeit werden neue Methoden zur Kühlung und Anregung von mechanischen Schwingungen in Diamant-Nanoresonatoren theoretisch analysiert. Die untersuchten Techniken zur Kontrolle der mechanischen Moden basieren dabei zum ersten Mal auf der intrinsischen Deformationskopplung der Schwingungen an natürliche Stickstoff- und Siliziumstörstellen in Diamant. Ausgehend von einer mikroskopischen Modellierung solcher Kopplungen werden in dieser Arbeit verschiedene theoretische Methoden aus dem Bereich der Quantenoptik verwendet, um das Laserkühlen von mechanischen Resonatoren bis Nahe an den quantenmechanischen Grundzustand, als auch die Realisierung von sogenannten Phononenlaser, zu beschreiben. Dabei wird vor allem gezeigt, wie quasi-entartete Energiezustände dieser Defektzentren ausgenützt werden können, um diese Effekte zu optimieren und dadurch auch unter experimentell relevanten Bedingungen möglich zu machen. Darüber hinaus wird in dieser Doktorarbeit untersucht, wie Phononen-induzierte Dissipation gezielt dazu verwendet werden kann, um anderen mechanische Schwingungsmoden zu kühlen oder auch in einen stationären verschränkten Zustand zu pumpen.

Als eine interessante Erweiterung der oben beschriebenen Effekte werden im dritten Teil dieser Doktorarbeit Systeme mit zwei oder mehreren gekoppelten Resonatoren behandelt, wobei die mechanischen Moden abwechselnd gekühlt oder mit der selben Rate gepumpt werden. Im klassischen Grenzfall besitzt die Dynamik solcher Systeme eine sogenannte Paritäts-Zeitumkehr-Symmetrie, welche für bestimmte Systemparameter gebrochen wird. In dieser Arbeit werden zum ersten Mal die Konsequenzen dieser Symmetriebrechung für die stationären Zustände dieser Systeme unter realistischen Bedingungen beschrieben. Dabei zeigt sich, dass die Kombination von nichtlinearen Sättigungseffekten und der Einfluss von thermischen als auch Quantenrauschen zu unerwarteten Ergebnissen führt, die sich deutlich von der dynamischen Symmetriebrechung unterscheiden. Insbesondere findet man weitere Phasen mit teilweise erhaltener oder gebrochener Paritäts-Zeitumkehr-Symmetrie, sowie einem Übergang von einem thermischen Zustand in eine Lasing-Phase mit stark reduzierten Fluktuationen.

Contents

1 INTRODUCTION **1**
1.1 Optomechanics 1
1.2 Impurity centers in diamond 2
1.3 Defect-phonon coupling 3
1.4 Cooling and phonon lasing 4
1.5 Parity-time-symmetric systems 4
1.6 Outline of the thesis 6
1.7 Publications 6

2 MECHANICAL SYSTEMS AND DEFECT CENTERS IN DIAMOND **9**
2.1 Quantized mechanical vibrations 9
2.2 Defect centers in diamond 23
2.3 Defect-phonon coupling 27

3 COOLING OF MECHANICAL MOTION AND PHONON LASING **34**
3.1 Cooling of mechanical motion 34
3.2 Basic laser theory 43

4 PHONON COOLING AND LASING WITH NITROGEN-VACANCY CENTERS IN DIAMOND **48**
4.1 Introduction 48
4.2 Model 50
4.3 Ground state cooling of a mechanical resonator 51
4.4 Phonon lasing with nitrogen vacancy centers 57
4.5 Detection 66

5 PHONON-RESERVOIR ENGINEERING WITH SiV CENTERS **69**
5.1 Introduction 69
5.2 Model 70
5.3 Phonon reservoirs 72
5.4 Cooling 78
5.5 Two-mode squeezing 83

6 PARITY-TIME-SYMMETRY BREAKING IN THE STEADY STATE **94**
6.1 Introduction 95
6.2 $\mathcal{PT}$-symmetry breaking 96
6.3 $\mathcal{PT}$-symmetric phonon systems 97
6.4 Steady state of $\mathcal{PT}$-symmetric systems in the absence of noise 99
6.5 Steady state in noisy $\mathcal{PT}$-symmetric systems 105
6.6 Arrays 109

7 SUMMARY AND OUTLOOK **112**

APPENDIX A APPENDIX **115**
A.1 Numerical simulations 115

BIBLIOGRAPHY **128**

Science may be described as the art of systematic over-simplification. — Karl Popper

1

Introduction

In this doctoral thesis we analyse novel ways to cool or actuate nano-mechanical resonators using natural impurities of diamond. By exploring these ideas further we have discovered new interesting effects that can arise when extending these ideas to coupled mechanical systems. To motivate this study, we here briefly introduce the field of optomechanics and the concept of cooling of mechanical motion as well as diamond's natural impurities and the way they can couple to phonons.

1.1 OPTOMECHANICS

Optomechanics explores the interaction between electromagnetic radiation and mechanical motion. Its quantum version, quantum optomechanics, has to do with the interaction between photons and the phonons [1]. In this case the vibrating object needs to be small enough so that the quantum nature of its vibrations can be revealed. For this reason, the scale of these objects varies between a few microns to tens of nanometers. Such micro- and nano-mechanical systems [2] have the ability to respond very sensitively to weak electric, magnetic and optical signals. This ability makes them unique tools for scientists and engineers and they are often used in sensing applications such as biosensors and accelerometers. The cooling of a nano-mechanical oscillator close to the quantum ground state was experimentally demonstrated in 2011 [3, 4], opening up possibilities for probing quantum mechanical effects at a macroscopic scale. But even before this breakthrough was achieved, a new area of research was initiated with the goal to control massive mechanical objects to a single-phonon level. Optomechanical cooling schemes are used to cool vibrational modes of micro- and nano-mechanical resonators close to their quantum ground state [1]. Similar to laser cooling of atoms (and ions), optomechanical cooling is the process of converting phonons into photons, by making use the radiation pressure of the field of an optical cavity towards a moving mirror [4–7]. The created photons are then lost from the cavity into the surrounding environment, removing energy from the system. Various schemes alternative to radiation pressure use as tools quantum dots [8, 9] or superconducting two-level systems [10–12] and as we shall see in this thesis, diamond's natural impurities.

1.2 Impurity centers in diamond

Impurities in crystals are formed when external atoms occupy lattice sites. More interesting structures are created when such substituted atoms are located near lattice vacancies. These particular impurities have the ability to effectively behave as molecules. Their multi-level energy structure, which is dictated by the molecular symmetry, can be exploited in quantum-optics applications. The most well-studied natural defect of diamond is the negatively charged nitrogen-vacancy center [13, 14]. The interest in this particular color center, is due to the long-coherence times of its electronic spin [15] as well as the fact that its spin state can be prepared and detected in an all-optical way [16]. Also, all-diamond nanostructures can be fabricated with very high mechanical quality factors [17, 18]. Additionally, it has been theoretically proposed to exploit the coupling of nitrogen-vacancy centers to phonons, in addition to photons, for applications related to quantum information processing [19–21] and quantum enhanced magnetometry [22]. Another natural defect in diamond, that we shall consider in this work, is the silicon-vacancy center. This center is currently a topic of very active research. The interest in this defect arises mainly from the fact that it can be used as a narrow line-width optical emitter [23–26]. Our aim in this work is to exploit the multi-level energy structure of diamond defects and present novel schemes for cooling and actuating mechanical vibrations in diamond nanostructures. This is achieved by engineering schemes that take advantage of the strain-induced coupling between impurities and mechanical vibrations.

1.3 Defect-phonon coupling

The energy levels of defects in solids, are highly susceptible to deformations of the surrounding lattice. Such local deformations can be caused by permanent (static) lattice strain or mechanical vibrations. One consequence of this susceptibility to local strain is the broadening of optical lines. In the case of vibrational modes this broadening is phonon-induced. There has been significant interest in exploiting these defect-phonon interactions in a particular kind of nanomechanical systems, known as phonon cavities, where single defects may be strongly coupled to individual phonon modes [20–22, 27–32]. This opens up possibilities for research in cavity quantum electrodynamics (cavity QED) using phonons. Possible applications range from measurement and manipulation of single phonons, to the coupling between defects through phonons. One very fundamental way to exploit this defect-phonon interactions, is to use the defects as tools for manipulating the state of vibrational modes in phonon cavities. As a first step towards these quantum applications, this thesis analyses schemes that can either cool a mechanical mode to its ground state or amplify it.

1.4 Cooling and phonon lasing

The basic principle behind the cooling of nano-mechanical resonators using the defect-phonon coupling is the same as in the case of laser cooling of atoms and ions [33]. Identifying optical transitions within the level structure of the impurities is crucial for engineering a cooling scheme. The fact that the strain-induced coupling is (partially) dispersive, allows optical transitions to be phonon assisted. By setting up the laser detuning appropriately, this results in transitions occurring via either the absorption or emission of a single phonon. Repeated phonon absorption results in the cooling of a specific mechanical mode while the opposite results in amplification. In the case where the cooling rate is higher that the intrinsic mechanical dumping, the resonator mode can be cooled down to the quantum ground state. On the other hand, the amplification of the resonator first results in an increase of the temperature. However, if the amplification occurs at higher rates than the mechanical dissipation, the mechanical mode starts to self-oscillate in a large-amplitude coherent state. This phenomenon is commonly known as phonon lasing and it has been investigated in various physical settings [34–42]. As the name suggests, this process is in complete analogy to a strongly pumped optical mode undergoing a lasing transition.

1.5 Parity-time-symmetric systems

Having discussed cooling and amplification ideas for individual modes in nano-mechanical systems, a natural question to ask is ”what would happen in a setup where both cooling (loss) and heating (gain) were present?”. The simplest system in which the above question can be investigated is a pair of coupled oscillators, one with gain and the other with loss. In the special case where the gain and loss occur at equal rates, the system possesses a very interesting symmetry. This symmetry corresponds to simultaneous time and parity reversal. Such parity-time-symmetric systems are currently the topic of active research in many areas of physics, such as optical waveguides [43–46], lattices and resonators [47–50] as well as cold atoms [51–53] and optomechanical systems [54–56]. The interest in these gain-loss systems arises from their ability to break their symmetry under certain conditions. More specifically, these systems remain parity-time-symmetric so long as the gain and loss rates do not exceed the coupling rate between the oscillators. In this symmetric regime, the system undergoes energy oscillations. Energy is transferred back and forth between the two oscillators. On the other hand, above threshold, the eigenvectors of the system are no longer symmetric under parity-time inversion. In this symmetry-broken regime, one of the modes is amplified and the other is cooled. In this thesis, we go for the first time beyond this dynamical picture and we investigate this parity-time-symmetric setup under realistic conditions in a system of coupled mechanical oscillators. In fact, we no longer assume that the gain and loss rates are constant, but rather depend —in a non-linear way— on the energy of the oscillation modes. This is the case for optical induced gain and loss, using for instance impurities in diamond, but is also the case for any other system, since amplification is always limited by saturation effects. In addition to this nonlinearity, we take into account the effects of noise in the system. In fact, we consider classical thermal noise as well as quantum noise generated by the intrinsic radiative decay of a diamond impurity. To extend the notion of parity-time symmetry in these realistic setups, we generalize the concept and instead of eigenvectors, we use the steady states in order to determine the symmetry of the system in each regime. In particular, we find that the inclusion of nonlinearities results in unexpected behavior that differs significantly from the usual dynamical picture, including a new type of symmetry breaking. Also, by introducing noise in the system we observe that in this case, the parity-time-symmetry breaking takes the form of an unconventional phase transition from a very noisy thermal state to a low-energy lasing state.

1.6 Outline of the thesis

This doctoral thesis is the result of research work performed at the TU Wien during the years 2012-2016. The organization of this dissertation is the following. In chapter 2, we give a brief introduction to the quantum description of mechanical modes of thin rectangular beams that we shall consider throughout this thesis. In addition, we summarize the physics of defects in diamond, to the extent relevant for this thesis. In chapter 3, we review the theory of cooling of mechanical motion with a two-level system as well as the basic laser theory. In chapter 4, we investigate schemes for mechanical cooling and phonon lasing in diamond nano-scale beams using nitrogen-vacancy centers. In chapter 5, we develop a phonon-reservoir engineering method using silion-vacancy centers and analyze cooling and entanglement-generation schemes. Finally, in chapter 6, we discuss the phenomenon of parity-time-symmetry breaking in realistic systems, using as an example a system of coupled mechanical resonators.

1.7 Publications

In addition to this thesis, three papers have been published in peer-review journals describing the results of this research work.

PHYSICAL REVIEW B 88, 064105 (2013) [57]

Phonon cooling and lasing with nitrogen-vacancy centers in diamond

K. V. Kepesidis, S. D. Bennett, S. Portolan, M. D. Lukin, P. Rabl,

This paper was published in Physical Review B in 2013. In this article, we consider the strain coupling between a single nitrogen-vacancy center and a single resonant mechanical mode of a diamond nanoresonator, and analyze ground state cooling and phonon lasing techniques for manipulating the phonon mode in this system. For this work, I performed all calculations described in the paper under the supervision of S. Portolan and P. Rabl.

PHYSICAL REVIEW B 94, 214115 (2016) [58]

Cooling phonons with phonons: acoustic reservoir-engineering with silicon-vacancy centers in diamond

K. V. Kepesidis, M.-A. Lemonde, A. Norambuena, J. R. Maze, P. Rabl,

This paper was published in Physical Review B in 2016. In this work, we describe a new approach for mechanical cooling and dissipation engineering for the low-frequency vibrations of a mechanical beam, which uses of the naturally occurring low-temperature bath provided by the high-frequency compression modes of the beam structure. We illustrate this scheme for the example of a negatively charged silicon-vacancy center in a vibrating nano-scale diamond beam. For this work, I performed the calculations related to the cooling and two-mode squeezing while M.-A. Lemonde performed the analysis of the phonon spectral density.

New Journal of Physics 18 (2016) 095003 [59]

$\mathcal{PT}$-symmetry breaking in the steady state of microscopic gain loss systems

K. V. Kepesidis, T. J. Milburn, J. Huber, K. G. Makris, S. Rotter and P. Rabl,

This paper was published in New Journal of Physics in 2016. In this work, we generalize the concept of parity-time symmetry to realistic systems with nonlinearities and under the influence of thermal and quantum noise. We illustrate this generalization and investigate its implications for the specific model of coupled mechanical resonators with optically induced loss and gain. In this work, I performed most of the analytical as well as numerical calculations. The stability analysis was performed together with T. J. Milburn and the numerical data for Fig. 5 was provided by J. Huber.

2

Mechanical systems and defect centers in diamond

In this chapter, we present some background on the systems we consider in the following chapters. In section 2.1, we provide details on the mechanical systems we use and derive the fundamental equations of motion as well as their mode structure. In section 2.2, we discuss the energy-level structure of the most important natural defects of diamond and the ways they couple to mechanical modes.

2.1 QUANTIZED MECHANICAL VIBRATIONS

In this section, we present the theory of elastic waves that manifest themselves as mechanical oscillations of thin rectangular beams. A thin beam is a structure which has one of its dimensions much larger than the other two. Figure 2.1 illustrates the two types of mechanical systems that are considered in this work, namely cantilever (singly-clamped) and doubly-clamped beams. The types of vibrations we consider are flexural, i.e. the bending of the beam, and longitudinal, i.e. its compression along its large dimension. For each type of vibrations we derive the governing equation, provide solutions by imposing the necessary boundary conditions and finally proceed with their quantization. The following discussion is mainly based on references [2, 60].

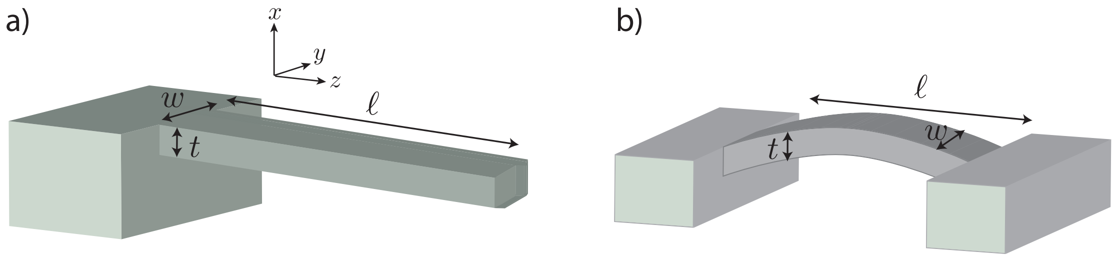

Figure 2.1 – Illustration of the two types of mechanical systems that are considered in this work, namely a) cantilever (singly-clamped) and b) doubly-clamped beams.

2.1.1 Bending vibrations

We first present a derivation of the Euler-Bernulli equation. This particular model which is also called *simple beam theory*, is a scalar theory for the beam's bending motion for more or less arbitrary forces. It is most accurate for thin beams, with small displacements. It is important to note that in this beam model the rotational inertia of the beam are not taken into account. Specifically, we consider a long rectangular beam of length ℓ along the z-axis, thickness t and width w, (cross-sectional area $A = w \times t$), and density ρ, as shown figure 2.2. The beam is assumed to be made of isotropic material with Young's modulus E. We assume displacements $\xi_x(z,t)$ causing the beam to flex along the x-direction. The force that this displacement generates on a differential element of mass dm, infinitesimal length dz is given by Newton's second law

$$F_x(z,t) = dm\frac{\partial^2}{\partial t^2}\xi_x(z,t) = \rho A \mathrm{d}z\frac{\partial^2}{\partial t^2}\xi_x(z,t), \tag{2.1}$$

where we have used the relation $\mathrm{d}m = \rho A \mathrm{d}z$ between the mass of the infinitesimal element and density of the material of the beam. In addition, the element is subject to forces $F_x(z + \mathrm{d}z)$ and $-F_x(z)$, on each respective face, along x-direction and torques $M_y(z + \mathrm{d}z)$ and $-M_y(z)$ along

y-direction from its two neighboring differential elements. Balancing the forces yields

$$F_x(z+\mathrm{d}z) - F_x(z) - \rho A \mathrm{d}z \frac{\partial^2}{\partial t^2}\xi_x(z,t) = 0. \tag{2.2}$$

Similarly assuming there is no net torque on the element, we obtain

$$F_x(z+\mathrm{d}z)\mathrm{d}z + M_y(z+\mathrm{d}z) - M_y(z) = 0. \tag{2.3}$$

We now expand the force $F_x(z+\mathrm{d}z)$ and torque $M_y(z+\mathrm{d}z)$ in a Taylor series to first order in z and keep only the the first two terms. By doing so, equations (2.2) and (2.3) take the forms

$$\frac{\partial F_x(z,t)}{\partial z} = \rho A \frac{\partial^2 \xi_x}{\partial t^2}, \tag{2.4}$$

$$F_x(z,t) = -\frac{\partial M_y(z,t)}{\partial z}. \tag{2.5}$$

In thin beam theory, the relation between pure torque and displacement is given by (see reference [2], chapter 6)

$$M_y = EI \frac{\partial^2 \xi_x}{\partial z^2}. \tag{2.6}$$

where $I = \int x^2 \mathrm{d}A = wt^3/12$ is the moment of inertial of the thin beam. Using this result we obtain the Euler-Bernoulli equation

$$\rho A \frac{\partial^2}{\partial t^2}\xi_x(z,t) + EI \frac{\partial^4}{\partial z^4}\xi_x(z,t) = 0. \tag{2.7}$$

This equation is solved by separation of variables, namely

$$\xi_x(z,t) = \sum_n q_n(t) u_n(z), \tag{2.8}$$

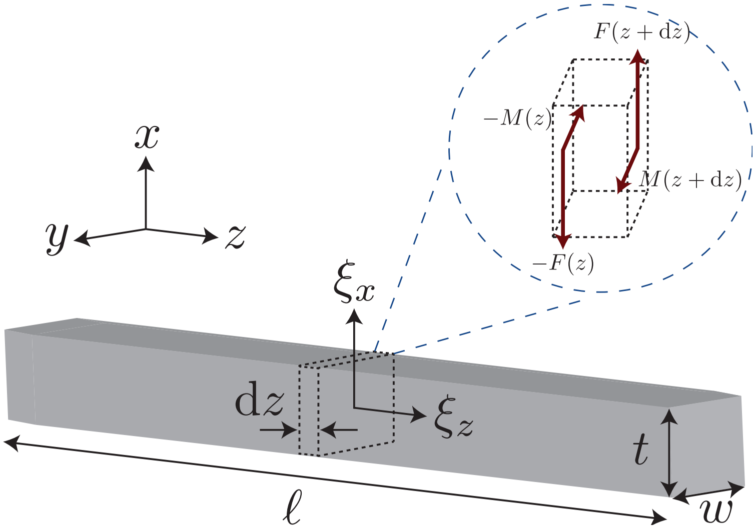

Figure 2.2 – Illustration of a long rectangular beam of length ℓ along the z-axis and cross-sectional area $A = w \times t$, with displacement $\xi(z)$. We consider two types of displacements, flexural in x-direction, due to forces along x-direction and torques along y-direction, related to the bending of the beam, and longitudinal along z-direction, related to the compression vibrations. The circular inset shows magnified the differential element of length $\mathrm{d}z$ and the corresponding forces and torques responsible for the flexural displacement.

where the displacement amplitudes q_n obey equations of harmonic oscillators $\ddot{q}_n + \omega_n^2 q_n = 0$ with frequencies

$$\omega_n = k_n^2 \sqrt{\frac{EI}{\rho A}} \tag{2.9}$$

and wave vectors k_n. The spatial part in the solution (2.8) takes the general form

$$u_n(t) = A\cos(k_n z) + B\sin(k_n z) + C\cosh(k_n z) + D\sinh(k_n z). \tag{2.10}$$

The coefficients A, B, C, D and the allowed wavevectors k_n are determined by the boundary conditions of the problem under consideration.

SINGLY-CLAMPED BEAM

For a cantilever beam of length ℓ and cross section $A = w \times t$, we impose the boundary conditions $u_n(0) = 0$, $u'_n(0) = 0$, $u''_n(\ell) = 0$, $u'''_n(\ell) = 0$; these constraints account for one fixed and one free end, assuming no transverse force and torque on the free end. Solving equation (2.7) one obtains

$$u_n(z) = \frac{1}{\sqrt{N_n}}\Big([\cos(k_n z) - \cosh(k_n z)] + \frac{\sin(\kappa_n) - \sinh(\kappa_n)}{\cos(\kappa_n) + \cosh(\kappa_n)}[\sin(k_n z) - \sinh(k_n z)]\Big), \tag{2.11}$$

where $\kappa_n = k_n \ell$ ($n = 1, 2, 3...$) and N_n is the appropriate normalisation factor. The allowed k-vectors are given by the condition

$$1 + \cos(\kappa_n)\cosh(\kappa_n) = 0. \tag{2.12}$$

By numerically solving this equation we obtain, we obtain the values $\kappa_n \approx 1.875,\ 4.694,\ 7.855, ...$ For $n > 1$, these values can be approximated by $\kappa_n \approx \pi(n - 0.5)$. The corresponding oscillation frequencies follow from equation (2.9). We chose a normalisation condition such that $u_n(\ell) = 1$, independently of n, i.e.

$$\int_0^\ell dz |u_n(z)|^2 = \frac{\ell}{4}. \tag{2.13}$$

We do so because we are mainly interested in the displacement of the free end of the beam. This results into the normalization constant $N_n = 2(\sinh^2(\kappa_n) - \sin^2(\kappa_n))$. To proceed with the quantization of the displacement and obtain a quantum model for the vibrating beam, we write down the Lagrangian function

$$L = \int_0^\ell dz \left[\frac{\rho A}{2}\left(\frac{\partial \xi_x}{\partial t}\right)^2 - \frac{EI}{2}\left(\frac{\partial^2 \xi_x}{\partial^2 z}\right)^2\right], \tag{2.14}$$

that reproduces the Euler-Bernoulli equation (2.7) using the Euler-Lagrange formalism. By inserting the mode decomposition given in equation (2.8), the Lagrangian can reduce to a sum of harmonic oscillators

$$L = \sum_n \frac{m_{\text{eff}}}{2}\dot{q}_n^2 - \frac{m_{\text{eff}}\omega_n^2}{2}q_n^2 \tag{2.15}$$

where we have introduced an effective mass m_{eff} defined by the normalization condition described above and given by

$$m_{\text{eff}} = \rho A \int_0^\ell dz |u_n(z)|^2 = \frac{m}{4}. \tag{2.16}$$

The right-hand side of the above equation is obtained by integration by parts and indicates that the effective mass is four times smaller than the real mass and is mode independent. The corresponding Hamiltonian is derived by applying Legendre transform and reads

$$H = \sum_n \frac{p_n^2}{2m_{\text{eff}}} + \frac{1}{2}m_{\text{eff}}\omega_n^2 q_n^2, \tag{2.17}$$

where $p_n = \partial L/\partial \dot{q}_n = m_{\text{eff}}\dot{q}_n$ are the canonical momenta. Following now the canonical quantization rules, we replace the displacement amplitudes q_n and the canonical momentum by operators obeying the usual commutation relation for position and momentum $[\hat{q}_n, \hat{p}_n] = i\hbar$ and can define harmonic-oscillator ladder operators for each mode

$$\hat{a}_n = \sqrt{\frac{m_{\text{eff}}\omega_n}{2\hbar}}\Big(\hat{q}_n + \frac{i}{m_{\text{eff}}\omega_n}\hat{p}_n\Big), \tag{2.18}$$

in terms of which, the Hamiltonian operator takes the form

$$\hat{H} = \sum_n \hbar\omega_n \Big(\hat{a}_n^\dagger \hat{a}_n + \frac{1}{2}\Big). \tag{2.19}$$

The displacement of the free end of the beam, in terms of ladder operators, is then given by

$$\hat{\xi}(\ell) = \sum_n u_n(\ell)\hat{q}_n = \sum_n \sqrt{\frac{\hbar}{2m_{\text{eff}}\omega_n}}\Big(\hat{a}_n + \hat{a}_n^\dagger\Big). \tag{2.20}$$

Doubly-clamped beam

Repeating the above procedure for a doubly-clamped beam, by imposing the boundary conditions $u_n(0) = 0$, $u_n'(0) = 0$, $u_n(\ell) = 0$, $u_n'(\ell) = 0$, yields

$$u_n(z) = \frac{1}{\sqrt{N_n}}\Big([\cos(k_n z) - \cosh(k_n z)] - \frac{\cos(\kappa_n) - \cosh(\kappa_n)}{\sin(\kappa_n) - \sinh(\kappa_n)}[\sin(k_n z) - \sinh(k_n z)]\Big). \tag{2.21}$$

The allowed k-vectors in this case are given by

$$\cos(\kappa_n)\cosh(\kappa_n) = 1, \tag{2.22}$$

with solutions $\kappa_n \approx 4.730,\ 7.853,\ 10.995, \ldots.$ The corresponding oscillation frequencies follow again from equation (2.9). Since there is no free end, we are mainly interested in the displacement at the middle of the beam. For this reason we choose a normalization such that $u_1(\ell/2) = 1$. This normalization condition defines an effective mass

$$m_{\text{eff}} = A\rho \int_0^\ell dz |u_1(z)|^2 \approx 0.4 \times m. \tag{2.23}$$

2.1.2 Compression modes

We consider again a rectangular beam, as shown in figure 2.2. We assume a displacements $\xi_z(z,t)$ causing the beam to be compressed and decompressed along the z direction. The force that is generated on an infinitesimal mass element dm is given by

$$F_z(z,t) = \rho A \mathrm{d}z \frac{\partial^2 \xi_z}{\partial t^2}. \tag{2.24}$$

Balancing the forces by neighboring differential elements, yields

$$F_z(z+\mathrm{d}z) - F_z(z) - \rho A \mathrm{d}z \frac{\partial^2}{\partial t^2} \xi_z(z,t) = 0. \tag{2.25}$$

We now expand $F_z(z+\mathrm{d}z)$ in a Taylor series and keep terms up to first order in z, obtaining

$$\rho A \frac{\partial^2 \xi_z}{\partial t^2} = \frac{\partial F}{\partial z}. \tag{2.26}$$

Using the relation between the strain and stress for longitudinal forces, i.e. $\partial \xi_z = F/EA$ (see reference [2], chapter 6), we obtain the 1-D wave equation for the longitudinal displacement,

$$\rho \frac{\partial^2 \xi_z(z,t)}{\partial t^2} = E \frac{\partial^2 \xi_z(z,t)}{\partial z^2}. \tag{2.27}$$

To solve the above equation, we perform separation of variables, which gives solutions of the form

$$\xi_z(z,t) = \sum_n q_n(t) u_n(z), \tag{2.28}$$

where the displacement amplitudes q_n obey equations of harmonic oscillators $\ddot{q}_n + \omega_n^2 q_n = 0$ with frequencies

$$\omega_n = k_n \sqrt{\frac{E}{\rho}} \tag{2.29}$$

and wave vectors k_n. The spatial part in the solution (2.28) is given by

$$u_n(z,t) = N\sin(k_n z) + M\cos(k_n z), \tag{2.30}$$

and N and M are normalization constants defined by the initial conditions.

Singly-clamped beam

We repeat the quantization procedure for compression waves in a cantilever using the boundary conditions $u(0) = u'(\ell) = 0$; these constraints account for one fixed and one free end, in the case of longitudinal waves. Under these conditions, the solution of equation (2.27) reads

$$u_n(z) = N_n \sin(k_n z) \tag{2.31}$$

where N_n are the normalization factors and the allowed wave-numbers are given by $k = (n-1/2)\pi/\ell$ $(n = 1, 2, 3...)$. We choose the following n-independent normalization

$$\int_0^\ell dz |u_n(z)|^2 = \frac{\ell}{2}. \tag{2.32}$$

To proceed to the quantization of the longitudinal waves and obtain a quantum model for the compression of the beam, we write down the Lagrangian function

$$L = \int_0^\ell dz \left[\frac{\rho A}{2} \left(\frac{\partial \xi_z}{\partial t} \right)^2 - \frac{EA}{2} \left(\frac{\partial \xi_z}{\partial z} \right)^2 \right], \tag{2.33}$$

which reproduces the equation (2.27), using the Euler-Lagrange formalism. Inserting the mode decomposition given in equation (2.28), the Lagrangian reduces again into the sum of harmonic oscillators

$$L = \sum_n \frac{m_{\mathrm{eff}}}{2}\dot{q}_n^2 - \frac{m_{\mathrm{eff}}\omega_n^2}{2} q_n^2, \tag{2.34}$$

and the effective mass in this case reads $m_{\mathrm{eff}} = m/2$. Following again the canonical quantization rules, we replace the displacement amplitudes q_n and the canonical momentum by operators obeying the usual commutation relation for position and momentum $[\hat{q}_n, \hat{p}_n] = i\hbar$ and can define harmonic-oscillator ladder operators for each mode.

DOUBLY-CLAMPED BEAM

Repeating the above procedure for a doubly-clamped beam, by imposing the boundary conditions $u(0) = u(\ell) = 0.$, yields

$$u_n(z) = N_n \sin(k_n z). \tag{2.35}$$

The allowed k-vectors in this case given by $k_n = n\pi/\ell$, where $n = 1, 2, 3, ...$ The corresponding oscillation frequencies follow again from equation (2.29). For the normalization we require $u_0(\ell/2) = 1$. In this case for the fundamental function we have $N_0 = 1$. The effective mass again reads $m_{\mathrm{eff}} = m/2$.

2.1.3 MECHANICAL DISSIPATION AND NOISE

Realistic systems are never isolated and are in general subject to environmental noise. Under experimental conditions though, the coupling of the system to the degrees of freedom of the environment can be low enough, to be treated as a small perturbation. Mechanical oscillation modes are considered to be coupled weakly to a bath of phonons in the beam's support or other uncontrolled noise sources. In the following we present the quantum master equation formulation for the evolution of the reduced density matrix ρ_m of a mechanical mode under the influence of a thermal phonon bath. The derivation of the particular master equation can be found in quantum optics [61–63] and nano-mechanics [2] textbooks. Notation-wise, we closely follow [64]. We start the derivation by specifying the Hamiltonians of the system and the phonon bath. The Hamiltonian of the mechanical modes is given by equation (2.19) and for a single mode (shifting the zero energy by $\bar{\omega}_0/2$) reads

$$H_S = \hbar\omega_0 a^\dagger a, \tag{2.36}$$

while the Hamiltonian of the bath is given by

$$H_B = \int_{\omega_0-\Delta_\mathrm{B}}^{\omega_0+\Delta_\mathrm{B}} d\omega\, \hbar\omega\, b^\dagger(\omega)b(\omega), \tag{2.37}$$

representing a continuum of bosonic modes with ladder operators obeying the commutation relation $[b_\omega, b^\dagger_{\omega'}] = \delta(\omega-\omega')$ and Δ_B denotes the bandwidth of the bath. The part of the Hamiltonian representing the interaction between the system and the bath is

$$H_\mathrm{int} = \hbar\sqrt{\gamma}\left(aB^\dagger + a^\dagger B\right), \tag{2.38}$$

where $\gamma = \omega_0/Q$ is the mechanical damping rate for a given mechanical quality factor Q. For simplification we have defined the collective bath operators

$$B = \frac{1}{\sqrt{2\pi}}\int_{\omega_0-\Delta_\mathrm{B}}^{\omega_0+\Delta_\mathrm{B}} d\omega\, b(\omega). \tag{2.39}$$

We assume that the bath is in thermal equilibrium and thus its two-time correlation functions read

$$\begin{aligned}
\langle B(\tau)B^\dagger(0)\rangle &\simeq (N_\mathrm{th}+1)e^{-i\omega_0\tau}\delta(\tau), && (2.40)\\
\langle B(\tau)^\dagger B(0)\rangle &\simeq N_\mathrm{th}e^{-i\omega_0\tau}\delta(\tau), && (2.41)
\end{aligned}$$

where $N_{\mathrm{th}} = (e^{\hbar\omega_0/k_BT} - 1)^{-1}$ is the (equilibrium) thermal occupation number of the modes with frequency $\omega \sim \omega_0$ for a support temperature T. Our goal is now to derive an effective equation for the evolution of the reduced system density operator $\rho_S(t) = \mathrm{Tr}_B\{\rho(t)\}$. As a first step we change into the interaction picture with respect to $H_0 = H_S + H_B$, i.e.,

$$\tilde{\rho}(t) = e^{iH_0t/\hbar}\rho(t)e^{-iH_0t/\hbar}. \tag{2.42}$$

In the interaction picture the von Neumann equation for $\tilde{\rho}(t)$ reads,

$$\dot{\tilde{\rho}}(t) = -\frac{i}{\hbar}[H_{\mathrm{int}}(t), \tilde{\rho}(t)] \tag{2.43}$$

where

$$H_{\mathrm{int}}(t) = e^{iH_0t/\hbar}H_{\mathrm{int}}e^{-iH_0t/\hbar} = \hbar\sqrt{\gamma}\left(cB^\dagger(t)e^{-i\omega_0t} + c^\dagger B(t)e^{i\omega_0t}\right). \tag{2.44}$$

The von-Neumann equation can be formally integrated and after tracing over the bath degrees of freedom we obtain

$$\begin{aligned}\tilde{\rho}_S(t) =& \tilde{\rho}_S(0) - \frac{i}{\hbar}\int_0^t dt'\,\mathrm{Tr}_B\{[H_{\mathrm{int}}(t'), \tilde{\rho}(0)]\}\\ &- \frac{1}{\hbar^2}\int_0^t dt'\int_0^{t'} dt''\,\mathrm{Tr}_B\{[H_{\mathrm{int}}(t'), [H_{\mathrm{int}}(t''), \tilde{\rho}(t'')]]\}.\end{aligned} \tag{2.45}$$

This result is still exact and we shall now proceed with the two approximations associated with the Born-Markov master equation.

Born approximation

To proceed we now assume that the system-bath interaction is sufficiently weak and in particular that it does not considerably alter the state of the reservoir. This means that to a good approximation we can write

$$\tilde{\rho}(t) \simeq \tilde{\rho}_S(t) \otimes \rho_B(0) \tag{2.46}$$

where $\rho_B(0)$ is the stationary state of the bath. Under the Born approximation the term (I) in equation (2.45) vanishes, since the coupling between system and bath is such that $\langle B(t) \rangle = \langle B^\dagger(t) \rangle = 0$. Then, after taking the time derivative, we end up with the Nakajima-Zwanzig equation

$$\dot{\tilde{\rho}}_S(t) = -\frac{1}{\hbar^2} \int_0^t dt' \, \mathrm{Tr}_B\{[H_{\mathrm{int}}(t), [H_{\mathrm{int}}(t'), \tilde{\rho}_S(t') \otimes \rho_B(0)]]\}. \tag{2.47}$$

This equation is non-local in time, i.e., the derivative of $\tilde{\rho}(t)$ at time t depends on $\tilde{\rho}(t')$ at all earlier times $0 < t' < t$.

Markov approximation

To simplify the Nakajima-Zwanzig further, we now make use of the fact that the bath (according to our definition) has a very short memory time, meaning that correlations between bath operators decay very fast. When evaluating the rhs. of equation (2.47) we encounter bath correlation functions of the form of equation (2.40) where the inverse correlation time, $\Delta_B = \tau_c^{-1}$, can be identified with the reservoir bandwidth. Note that in equation (2.40) the $\delta(\tau)$ is the delta-function on the scale of the inverse bandwidth. Then, for $t \gg \tau_c$ we can approximately set $\tilde{\rho}_S(t') \simeq \tilde{\rho}_S(t)$ and

$$\dot{\tilde{\rho}}_S(t) \simeq -\frac{1}{\hbar^2} \int_{-\infty}^t dt' \, \mathrm{Tr}_B\{[H_{\mathrm{int}}(t), [H_{\mathrm{int}}(t'), \tilde{\rho}_S(t) \otimes \rho_B(0)]]\}. \tag{2.48}$$

By substituting $\tau = t - t'$ we obtain

$$\dot{\tilde{\rho}}_S(t) \simeq -\frac{1}{\hbar^2}\int_0^\infty d\tau\,\mathrm{Tr}_B\{[H_{\mathrm{int}}(t),[H_{\mathrm{int}}(t-\tau),\tilde{\rho}_S(t)\otimes\rho_B(0)]]\} \tag{2.49}$$

which is the master equation for $\tilde{\rho}_S(t)$, still in a general form. Note that this equation is now local in time, i.e. $\dot{\tilde{\rho}}_S(t) \sim \tilde{\rho}_S(t)$. The evaluation of the double-commutator in equation (2.49) results into four terms. After taking the trace and using the properties of the correlation functions (2.40), we collect all the terms and change back into the Schrödinger picture. Then, after integrating over the time τ, we obtain the master equation for $\rho_S(t)$,

$$\begin{aligned}\dot{\rho}_S = -i\omega_0[a^\dagger a,\rho_S] &+ \frac{\gamma}{2}(N_{\mathrm{th}}+1)\left(2a\rho_S a^\dagger - a^\dagger a\rho_S - \rho_S a^\dagger a\right)\\ &+ \frac{\gamma}{2}N_{\mathrm{th}}\left(2a\rho_S a^\dagger - a^\dagger a\rho_S - \rho_S a^\dagger a\right).\end{aligned} \tag{2.50}$$

Using the above equation, one can derive equations of motion for expectation values, i.e.

$$\langle\dot{O}(t)\rangle = \mathrm{Tr}\{O\dot{\rho}(t)\} = \mathrm{Tr}\{O\mathcal{L}(\rho(t))\}. \tag{2.51}$$

The corresponding equation for the mean phonon occupation number is given by

$$\begin{aligned}\partial_t\langle a^\dagger a\rangle =& -\gamma(N_{\mathrm{th}}+1)\langle a^\dagger a\rangle + \gamma N_{\mathrm{th}}\langle a a^\dagger\rangle\\ =& -\gamma\langle a^\dagger a\rangle + \gamma N_{\mathrm{th}}.\end{aligned} \tag{2.52}$$

This means that if the mechanical mode is in its quantum ground state, the rate in which a first phonon will be absorbed from the environment is given by $\gamma N_{\mathrm{th}} \approx k_B T/\hbar Q$. Solving equation (2.52), yields

$$\langle a^\dagger a\rangle(t) = e^{-\gamma t}\langle a^\dagger a\rangle(0) + \left(1 - e^{-\gamma t}\right)N_{\mathrm{th}}, \tag{2.53}$$

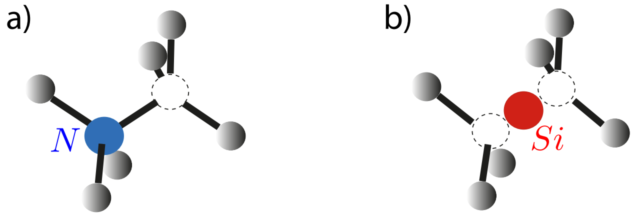

Figure 2.3 – Illustration of the two types of color centers in diamond that we consider in this work. a) Sketch of the nitrogen-vacancy center in diamond. It is formed by a substitutional nitrogen atom and an adjacent lattice vacancy. b) Sketch of the silicon-vacancy center in diamond. It is formed by a silicon atom and a split vacancy replacing two neighboring carbon atoms.

which describes relaxation towards thermal equilibrium.

2.2 DEFECT CENTERS IN DIAMOND

In this section, we introduce two of the most interesting types of natural defects in diamond [65], namely the nitrogen-vacancy (NV) and silicon-vacancy (SiV) color centers.

2.2.1 NV CENTERS

The negatively-charged nitrogen-vacancy (NV) color center is formed when a nitrogen atom has replaced a carbon atom of the diamond lattice and is located next to a lattice vacancy. Figure 2.3 a) illustrates a sketch of this color center. The whole structure constitutes an effective molecule with a C_{3v} symmetry. It has six outer electrons, three of them come from the carbon atoms, two from the nitrogen atom and one is captured from the environment. These electrons occupy four orbitals, as dictated by this specific symmetry type, which we shall label $a_1(1), a_1(2), e_x, e_y$. These orbitals are linear combinations of the electronic orbitals located near the carbon and the nitrogen atoms [66, 67]. The ground state of the system (minimizing the Coulomb interaction between the electrons) is a spin triplet which is formed when four electrons occupy the symmetric orbitals $a_1(1), a_1(2)$ and two occupy the degenerate e_x, e_y orbitals, as shown in figure 2.4 a). One can adopt a representation in terms of *holes* rather than electrons. In this picture, the ground state can be

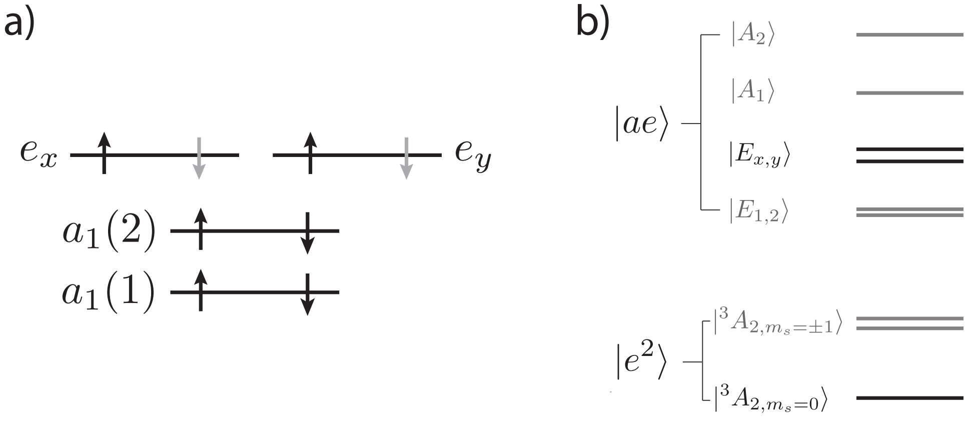

Figure 2.4 – Level structure of color centers in diamond. a) Ground state single particle configuration in the electron (black) and in the hole (grey arrows) representations. b) Energy level diagram of the nitrogen-vacancy center showing the spin sub-levels of the ground and the first excited triplet state. The energy levels important for this work are highlighted in black.

described by a pair of holes occupying the levels e_x and e_y, as indicated by the grey arrows in the figure 2.4 a) and can be written as [66]

$$|^3A_{2m_s}\rangle = |e_x e_y - e_y e_x\rangle \otimes |m_s\rangle, \tag{2.54}$$

where $m_s = \pm 1, 0$ accounts for the three possible spin projections. The degeneracy of states with $|m_s| = 1$ and $m_s = 0$ is lifted by spin-spin interactions. The first excitation corresponds to the transition of one of the holes from either e_x or e_y to the $a_1(2)$ orbital. This orbital is a doublet state and combined with the spin triplet yields in total six levels which make up the manifold of the first excited state. We label these levels as follows $|E_{1,2}\rangle$,$|E_{x,y}\rangle$ and $|A_{1,2}\rangle$, in consistency with references [66, 67]. The energy gap between these states is of the order of a few GHz. The degeneracy lifting is due to spin-orbit and spin-spin interactions. The level ordering of both the ground and the excited states is shown in figure 2.4 b). In this thesis we are mainly interested in the pair of excited levels

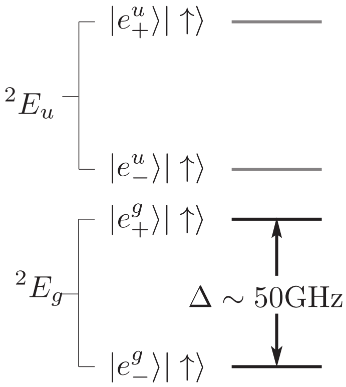
$|e_+^u\rangle|\uparrow\rangle$
^2E_u
$|e_-^u\rangle|\uparrow\rangle$
$|e_+^g\rangle|\uparrow\rangle$
^2E_g
$\Delta \sim 50\text{GHz}$
$|e_-^g\rangle|\uparrow\rangle$

Figure 2.5 – Energy levels of silicon-vacancy center. The levels illustrated here are spin-1/2 doublets and for simplicity only the spin-up levels are drawn.

corresponding to zero spin, namely

$$|E_{x,y}\rangle = |ae_{x,y} - e_{x,y}a\rangle \otimes |m_s = 0\rangle. \tag{2.55}$$

The interest in these states arises from the fact that, using linearly polarized light, one can selectively drive transitions to these levels from the $m_s = 0$ ground state. In the absence of strain (or external fields), these levels are degenerate. However the degeneracy is lifted by local strain caused by lattice distortions.

2.2.2 SiV CENTER

The negatively charged SiV color center in diamond is formed by a silicon atom and a split vacancy replacing two neighboring carbon atoms as shown in figure 2.3 b). The electronic ground state of this center consists of a single unpaired hole with spin $S = 1/2$, which can occupy one of the two degenerate orbital states $|e_x\rangle$ or $|e_y\rangle$ [68, 69]. The spin and orbital degeneracy is lifted by the spin-orbit coupling and by the Jahn-Teller (JT) effect [70, 71]. In the presence of an external magnetic field $\vec{B}$, the Hamiltonian for the electronic ground state of the SiV$^-$ center is ($\hbar = 1$) [69]

$$H^0_{\mathrm{SiV}} = -\lambda_{\mathrm{SO}} L_z S_z + H_{\mathrm{JT}} + f\gamma_L B_z L_z + \gamma_S \vec{B} \cdot \vec{S}. \tag{2.56}$$

Here L_z and S_z are the projections of the dimensionless angular momentum and spin operators $\vec{L}$ and $\vec{S}$ onto the symmetry axis of the center, which we assume to be aligned along the z-axis. $\lambda_{\mathrm{SO}} > 0$ is the spin-orbit coupling while γ_L and γ_S are respectively the orbital and spin gyromagnetic ratios. The parameter $f \approx 0.1$ accounts for the reduced orbital Zeeman effect in the crystal lattice [69, 70].

For weak external magnetic fields, the dominant interaction in equation (2.56) is set by the spin-orbit coupling, $\lambda_{\mathrm{SO}}/2\pi \approx 45$ GHz, which splits the ground state manifold into two lower states $\{|e_-, \downarrow\rangle, |e_+, \uparrow\rangle\}$ and two upper states $\{|e_+, \downarrow\rangle, |e_-, \uparrow\rangle\}$. Here $|e_\pm\rangle = (|e_x\rangle \pm i|e_y\rangle)/\sqrt{2}$ are eigenstates of the angular momentum operator, $L_z|e_\pm\rangle = \pm|e_\pm\rangle$. The JT interaction $\hat{H}_{\mathrm{JT}}$ with strength $\Upsilon < \lambda_{\mathrm{SO}}$ does not affect the spin degrees of freedom, but leads to a mixing between the orbital angular momentum states $|e_+\rangle$ and $|e_-\rangle$ (dynamical JT interaction [70, 71]). From a combined diagonalization of the spin-orbit and the JT interaction, we obtain a total splitting of the ground state of $\Delta = \sqrt{\lambda^2_{\mathrm{SO}} + 4\Upsilon^2} \approx 2\pi \times 50$ GHz and two sets of pairwise degenerate eigenstates $\{|1\rangle, |2\rangle\}$ and $\{|3\rangle, |4\rangle\}$. Specifically, in the basis spawned by the degenerate eigenstates $|e_x, \uparrow\rangle, |e_x, \downarrow\rangle, |e_y, \uparrow\rangle$ and $|e_y, \downarrow\rangle$, the different contributions to the SiV$^-$ energy levels, introduced in equation (2.56), read

$$\begin{aligned} (\gamma_S B_0 - \lambda_{SO} L_z) S_z &= \frac{1}{2}\begin{bmatrix} \gamma_S B_0 & i\lambda_{SO} \\ -i\lambda_{SO} & \gamma_S B_0 \end{bmatrix} \otimes \begin{bmatrix} 1 & 0 \\ 0 & -1 \end{bmatrix}, \\ H_{JT} &= \begin{bmatrix} \Upsilon_x & \Upsilon_y \\ \Upsilon_y & -\Upsilon_x \end{bmatrix} \otimes \begin{bmatrix} 1 & 0 \\ 0 & 1 \end{bmatrix}. \end{aligned} \tag{2.57}$$

Here, Υ_x (Υ_y) represents an energy shift due to local strain in the crystal along x (y), such that

$\Upsilon = \sqrt{\Upsilon_x^2 + \Upsilon_y^2}$. For the following analysis we consider small magnetic fields and we neglect the effect of the reduced orbital Zeeman interaction ($\sim f\gamma_L B_0$). Diagonalizing equation (2.57) leads to the eigenstates

$$\begin{aligned} |1\rangle &= \Big(\cos\theta|e_x\rangle - i\sin\theta e^{-i\phi}|e_y\rangle\Big)\,|{\downarrow}\rangle, \\ |2\rangle &= \Big(\cos\theta|e_x\rangle + i\sin\theta e^{i\phi}|e_y\rangle\Big)\,|{\uparrow}\rangle, \\ |3\rangle &= \Big(\sin\theta|e_x\rangle + i\cos\theta e^{-i\phi}|e_y\rangle\Big)\,|{\downarrow}\rangle, \\ |4\rangle &= \Big(\sin\theta|e_x\rangle - i\cos\theta e^{i\phi}|e_y\rangle\Big)\,|{\uparrow}\rangle, \end{aligned} \tag{2.58}$$

where

$$\tan(\theta) = \frac{2\Upsilon_x + \Delta}{\sqrt{\lambda_{\mathrm{SO}}^2 + 4\Upsilon_y^2}}, \qquad \tan(\phi) = \frac{2\Upsilon_y}{\lambda_{\mathrm{SO}}}. \tag{2.59}$$

The corresponding eigenenergies are:

$$E_{3,1} = (-\gamma_S B_0 \pm \Delta)/2, \quad E_{4,2} = (\gamma_S B_0 \pm \Delta)/2. \tag{2.60}$$

In figure 2.5 we illustrate the levels and for simplicity only the spin-up levels are drawn. For the cooling schemes described in chapter 5 we will neglect small distortions of the orbital states by the JT effect and use the approximation $|1\rangle \approx |e_-,{\downarrow}\rangle$, $|2\rangle \approx |e_+,{\uparrow}\rangle$, $|3\rangle \approx |e_+,{\downarrow}\rangle$ and $|4\rangle \approx |e_-,{\uparrow}\rangle$ [see figure 5.1 b) in chapter 5].

2.3 DEFECT-PHONON COUPLING

In this section, we discuss the effects of lattice distortions on the above-described diamond defects and derive the corresponding coupling Hamiltonians.

2.3.1 NV-PHONON INTERACTIONS

The effect of strain on the electronic states can be described by a Hamiltonian which can be split into two parts

$$H_{\text{strain}} = H_{\text{a}} + H_{\text{na}}. \tag{2.61}$$

The axial part H_{a} accounts for the lattice deformations which are symmetric, while the non-axial part H_{na} represents deformations which reduce the C_{3v} symmetry of the defect [70, 72, 73]. The ground state of the nitrogen-vacancy center is immune to lattice distortions and the effect of H_{strain} on $|^3A_{2m_s}\rangle$ can be neglected. On the other hand, due to their degeneracy the orbitals e_x and e_y are very susceptible to external perturbations [66, 67]. In terms of the states of interest, the strain-coupling Hamiltonian takes the following form

$$H_{\text{a}} = \epsilon_A \Xi_A \left(|E_x\rangle\langle E_x| + |E_y\rangle\langle E_y|\right), \tag{2.62}$$

for the axial part and

$$H_{\text{na}} =\epsilon_E \Xi_E \left(|E_x\rangle\langle E_x| - |E_y\rangle\langle E_y|\right) + \epsilon'_E \Xi'_E \left(|E_x\rangle\langle E_y| + |E_y\rangle\langle E_x|\right), \tag{2.63}$$

for the non-axial part, respectively. We denote with Ξ_A, Ξ_E and Ξ'_E the deformation-potential constants and with ϵ_A, ϵ_E and ϵ'_E the corresponding components of the strain tensor. These components can be derived through group-theoretic considerations (see reference [66] for more details). We see that H_{a} can only shift the energy of the entire excited state relatively to the ground state. The two contributions in H_{na} account for a strain-induced splitting of $|E_x\rangle$ and $|E_y\rangle$ relatively to each other (lifting of the degeneracy) and a strain-induced mixing of these two excited levels.

In chapter 4 we will be interested in the strain field associated with a single quantized mode of a nano-mechanical beam. For small displacements the induced strain at the position of the NV center is linear in the mode amplitudes and in second quantization the strain Hamiltonian given in equations (2.62) and (2.63) can be written in the form [72]

$$H_{\text{strain}} = \hbar \sum_{\nu=0,\|,\perp} \lambda_\nu \Sigma_\nu (a + a^\dagger). \tag{2.64}$$

Here a and $a^\dagger$ are the bosonic operators for the vibrational mode, λ_ν are the corresponding coupling constants. The operators $\Sigma_\| = |E_x\rangle\langle E_x| - |E_y\rangle\langle E_y|$, $\Sigma_\perp = |E_x\rangle\langle E_y| + |E_y\rangle\langle E_x|$ and $\Sigma_0 = |E_x\rangle\langle E_x| + |E_y\rangle\langle E_y|$ are the operators associated with a relative energy shift, a mixing between the excited states and a common shift of the excited states due to axial strain, respectively. The values of the corresponding coupling parameters λ_0, $\lambda_\|$ and $\lambda_\perp$ depend on details of the specific experimental setup, such as the resonator dimensions, the vibrational mode function of interest as well as the orientation of the NV center in the diamond lattice.

To estimate the absolute strength of the NV-phonon coupling we consider a doubly clamped diamond nanobeam of dimensions $(l, w, t) = (2, 0.2, 0.2)\,\mu\text{m}$. The fundamental bending mode of this beam has a frequency of $\omega_m/(2\pi) \approx 1$ GHz. For a NV center positioned at distance z_0 away from the axis of the beam, the induced stress per zero point oscillation a_0 is approximately given by $\sigma = [\partial^2 u(x)/\partial x^2] E z_0 a_0$, where $E \approx 1.2$ TPa is the Young's modulus and $u(x)$ is the displacement field of the fundamental mode [2, 8, 22]. Measurements of the NV energy level splitting as a function of applied stress [65, 74] give values around $\partial\omega/\partial\sigma \sim 2\pi \times 1$ kHz. This corresponds to a deformation potential coupling of $\Xi \approx 5$ eV and $\lambda/(2\pi) \approx 6$ MHz. Similarly, by considering the lowest order compression mode (along the long axis of the beam) we obtain a mechanical frequency of $\omega_m/(2\pi) \approx 4.5$ GHz. In this case the stress per zero-point motion is given by $\sigma = [\partial u(x)/\partial x] E a_0$, where $u(x) = \sin(\pi x/L)$, and results in a similar coupling constant of $\lambda/(2\pi) \approx 6.5$ MHz. These estimates show that in micron scale structures NV-phonon couplings of a few MHz are expected, while, for example, by using a compression mode, the NV center is still located sufficiently far from the surface.

2.3.2 SiV-PHONON INTERACTIONS

In Chapter 5 we will consider both magnetic as well as strain induced interactions between phonons and a SiV center in the electronic ground state. Since the levels structure and energy scales of the SiV center are quite different also these couplings will results in slightly different interactions and since these two types of coupling affect the various vibrational modes differently, we divide the phonon modes into low-frequency (l.f.) and high-frequency (h.f.) modes, i.e.

$$H_{\text{ph}} = \sum_{l}^{(\text{l.f.})} \omega_l b_l^\dagger b_l + \sum_{n}^{(\text{h.f.})} \omega_n c_n^\dagger c_n, \tag{2.65}$$

where the b_l and c_n are bosonic lowering operators. The first sum accounts for the lowest order vibrational modes of the beam. In particular, we are interested in the fundamental bending mode along z with frequency ω_{b}; for a rectangular beam of dimensions $(\ell, w, t) \approx (25, 0.1, 0.1)\mu$m, $\omega_{\text{b}} \approx \sqrt{Et^2/12\rho}(1.88/\ell)^2 \approx 2\pi \times 480$ kHz with E and ρ being the Young's modulus and the mass-density of diamond, respectively [see equation (2.7)]. This frequency is too low to induce transitions between the orbital states, but the bending motion leads to a large absolute displacement of the SiV$^-$ center located at the end of the beam. In the presence of a strong magnetic field gradient, $\partial_z B_z$, it results in a modulation of the Zeeman splitting and a magnetic spin-phonon interaction of the form [75]

$$H_{\text{mag}} = g_{\text{m}}(b^\dagger + b)S_z. \tag{2.66}$$

Here, $g_{\mathrm{m}} = \gamma_S z_{\mathrm{ZPF}} \partial_z B_z/\hbar$ denotes the coupling per phonon, where $z_{\mathrm{ZPF}} = \sqrt{\hbar/(2m_{\mathrm{eff}}\omega_{\mathrm{b}})}$ is the zero-point motion of the fundamental bending mode of the cantilever of volume $V = \ell wt$ and an effective vibrating mass of $m_{\mathrm{eff}} = \rho V/4$ [2]. For the beam dimensions given above and achievable magnetic gradients of up to 10^7 T/m [76, 77], the resulting coupling strength can be as large as $g_{\mathrm{m}}/2\pi \approx 80$ kHz, and scales as $g_{\mathrm{m}} \sim \sqrt{\ell/t^2 w}$ with the beam dimensions (the thickness t is along the magnetic gradient). Note that while higher order bending modes would couple to the spin as well, all applications discussed in chapter 5 rely on resonant excitation schemes that single out a specific vibrational mode. This justifies the assumed single-mode approximation in equation (2.66) for the magnetic coupling.

The second sum in equation (2.65) accounts for compression modes inside the beam with frequencies $\omega_n \sim \Delta$ of the order of the SiV$^-$ level splitting. These modes have a negligible effect on the absolute displacement of the beam, but they induce a local crystal strain which couples to the orbital states of SiV$^-$ center.

Local strain or local distortions in the SiV$^-$ structure generates a displacement of the defect atoms. This leads to a change in the potential seen by each atoms and result in a modification of the electronic distribution of the defect via electron-ion interaction. To first order in the ion displacements and in the Born-Oppenheimer approximation, this local distortion effect can be modeled by the strain Hamiltonian

$$H_{\mathrm{strain}} = \sum_{i,j,\alpha,\beta} |\alpha\rangle\langle\alpha|V_{ij}|\beta\rangle\langle\beta|\hat{\gamma}_{ij}. \tag{2.67}$$

Here, $|\alpha\rangle$ is the electronic basis and V_{ij} are couplings that involve the electron-ion Coulomb interaction [66]. The strain field tensor can be symmetrically decomposed as $\hat{\gamma} = \hat{\gamma}_{A_{1g}} + \hat{\gamma}_{E_g}$, where

$$\begin{aligned}
\hat{\gamma}_{A_{1g}} &= \begin{bmatrix} \frac{1}{2}\left(\hat{\gamma}_{xx} + \hat{\gamma}_{yy}\right) & 0 & 0 \\ 0 & \frac{1}{2}\left(\hat{\gamma}_{xx} + \hat{\gamma}_{yy}\right) & 0 \\ 0 & 0 & \hat{\gamma}_{zz} \end{bmatrix}, \\
\hat{\gamma}_{E_g} &= \begin{bmatrix} \frac{1}{2}\left(\hat{\gamma}_{xx} - \hat{\gamma}_{yy}\right) & \hat{\gamma}_{xy} & \hat{\gamma}_{xz} \\ \hat{\gamma}_{xy} & \frac{1}{2}\left(\hat{\gamma}_{yy} - \hat{\gamma}_{xx}\right) & \hat{\gamma}_{yz} \\ \hat{\gamma}_{xz} & \hat{\gamma}_{yz} & 0 \end{bmatrix}.
\end{aligned} \tag{2.68}$$

Due to the inversion symmetry of the SiV$^-$ [78], the orbital degrees of freedom of the states within the ground and excited subspace are characterized by parity [79]. As a consequence, expectation values $\langle\alpha|V_{iz}|\alpha\rangle$ and $\langle\alpha|V_{zz}|\alpha\rangle$ vanish in both ground and excited subspaces. Therefore, in the electronic basis spawned by $\{|e_{gx}\rangle, |e_{gy}\rangle\}$, the strain Hamiltonian can be written as [80]

$$H_{\text{strain}} = \begin{bmatrix} \delta & 0 \\ 0 & \delta \end{bmatrix} + \begin{bmatrix} \alpha & \beta \\ \beta & -\alpha \end{bmatrix}, \tag{2.69}$$

with $\delta = g_0\left(\hat{\gamma}_{xx} + \hat{\gamma}_{yy}\right)$, $\alpha = g_1\left(\hat{\gamma}_{xx} - \hat{\gamma}_{yy}\right)$ and $\beta = g_2\hat{\gamma}_{xy}$. Here, g_0, g_1 and g_2 are coupling constants. The first term of the strain Hamiltonian is the energy shift induced by symmetry local distortions and can be neglected. Finally, if we write the strain Hamiltonian using the basis spawned by the eigenstates of the spin-orbit coupling [see discussion after equation (2.56)], we obtain

$$\begin{aligned}
H_{\text{strain}} &= \begin{bmatrix} 0 & \alpha - i\beta \\ \alpha + i\beta & 0 \end{bmatrix} \otimes \begin{bmatrix} 1 & 0 \\ 0 & 1 \end{bmatrix} \\
&= g_1\left(\hat{\gamma}_{xx} - \hat{\gamma}_{yy}\right)\left(L_- + L_+\right) - ig_2\hat{\gamma}_{xy}\left(L_- - L_+\right).
\end{aligned} \tag{2.70}$$

Thus, within the framework of linear elasticity theory, the strain coupling is given by

$$H_{\text{strain}} = g_1(\hat{\gamma}_{xx} - \hat{\gamma}_{yy})(L_- + L_+) - 2ig_2\hat{\gamma}_{xy}(L_- - L_+), \tag{2.71}$$

where $L_+ = L_-^\dagger = |3\rangle\langle 1| + |2\rangle\langle 4|$ is the orbital raising operator within the ground state manifold and $g_{1,2}$ are the strength of the couplings to the strain field. From measurements of the related NV$^-$ defect, we expect the strain couplings $g_1 \approx g_2$ to be of the order of PHz [81]. The local strain fields are defined as

$$\hat{\gamma}_{ij} = \frac{1}{2}\left(\frac{\partial \hat{u}_i}{\partial x_j} + \frac{\partial \hat{u}_j}{\partial x_i}\right), \tag{2.72}$$

with u_1 (u_2, u_3) representing the quantized displacement fields along $x_1 = x$ ($x_2 = y, x_3 = z$) at the position of the SiV$^-$ center.

By decomposing the local displacement field $\vec{u} = \sum_n(\vec{u}_n c_n + \vec{u}_n^* c_n^\dagger)$ in terms of vibrational eigenmodes with normalized mode functions $\vec{u}_n$ and bosonic operators c_n, and after making a RWA, the resulting strain coupling can be written in the general form

$$H_{\text{strain}} \simeq \sum_n^{(\text{h.f.})} \left(g_{\text{s},n}\hat{c}_n J_+ + g_{\text{s},n}^*\hat{c}_n^\dagger J_-\right), \tag{2.73}$$

where $J_- = J_+^\dagger = |1\rangle\langle 3| + |2\rangle\langle 4|$. Note that while the operators $L_\pm$ induce transitions between the orbital states $|e_+\rangle$ and $|e_-\rangle$, the operators $J_\pm$ induce transitions between the higher and lower energy states. For a known set of mode functions $\vec{u}_n$, the couplings $g_{\text{s},n}$ can be derived by substituting in Eq. (2.71) the corresponding strain field $\gamma_{ij}^{(n)}$ for each mode.

3

Cooling of mechanical motion and phonon lasing

This chapter provides an introduction to the concepts of cooling and lasing. Specifically, we present a rigorous theory of cooling of a phonon cavity, i.e., a mechanical resonator mode, and a basic theory of phonon lasing, based on a semiclassical description. The results presented in this chapter are mainly a summary of standard quantum optical techniques for describing cooling [4–12, 33] or lasing phenoma [34–42]. In chapters 4-6, these techniques will be adapted and generalized for modeling these effects in various defect-phonon systems. For the presentations of the cooling and lasing theories, we rigorously derive standard master equations as well as Focker-Planck equations that can be found in various quantum-optics textbooks, such as [61, 62].

3.1 Cooling of mechanical motion

In this first section, we develop a rigorous theory of cooling of mechanical motion using an atom-like system, for example a defect center in a diamond nano-mechanical resonator. We will also use this example to discuss perturbative techniques within the master equation formalism. As a starting point, we consider a mechanical oscillator interacting with an atomic system, for example a defect center which is part of its lattice structure. Since the defect is a part of the resonator itself, it is possible to manipulate the motion of the resonator using the internal level structure of the defect,

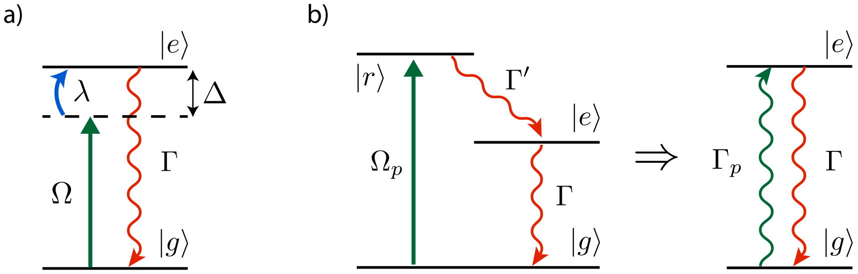

Figure 3.1 – a) Illustration of the two-level cooling scheme. The atomic state $|e\rangle$ is optically pumped with the simultaneous absorption of a phonon of frequency ω_m. b) Illustration of a three-level pumping scheme (lasing scheme), where the atomic state $|e\rangle$ is pumped via excitations to a third auxiliary level $|r\rangle$. In the limited $\Gamma' \gg \Omega_p$ this process can be modeled by an incoherent pumping process from $|g\rangle$ to $|e\rangle$ with rate $\Gamma_p \approx \Omega_p^2/(2\Gamma')$. This illustration is a reconstruction of a similar figure presented in reference [64].

which we shall assume for simplicity that consists of only two energy levels. Figure 3.1 a) shows the two-level cooling scheme, which is a single-phonon absorption mechanism. Specifically, the atomic state $|e\rangle$ is optically pumped with the simultaneous absorption of a phonon of frequency ω_m. Based on the discussions in the previous chapter, we consider a Hamiltonian for the combined system of the form

$$H = H_\mathrm{A} + \hbar\omega_\mathrm{m} a^\dagger a + \hbar\lambda(a^\dagger + a)\Sigma, \tag{3.1}$$

where H_A and the operator Σ depend on the type of the atomic system we use and the way it couples to the mechanical mode. Throughout our example in this chapter we shall assume that the atomic system is a two-level system. The atomic Hamiltonian in this case then reads

$$H_\mathrm{A} = -\hbar\Delta\sigma_z + \hbar\frac{\Omega}{2}\sigma_x \tag{3.2}$$

and the coupling operator simplifies to $\Sigma = \sigma_z$. This coupling type is associated with a relative energy shift between the energy levels. In particular this is the case for defects in materials, due to lattice distortion effects that can shift the levels. We note that in the case of atoms in optical cavities such an effect is absent and for the cooling purposes one would assume a σ_x type coupling. We can now write down the master equation in the following form,

$$\dot{\rho} = -i[H, \rho] + \mathcal{L}_{\Gamma}(\rho) + \mathcal{L}_{\gamma}(\rho), \tag{3.3}$$

where the second term accounts for the relaxation of the two-level system. Assuming that the transition is optical (either direct radiative decay or optical spin pumping processes), we can ignore the effects of temperature and write

$$\mathcal{L}_{\Gamma}(\rho) = \frac{\Gamma}{2}\left(2\sigma_-\rho\sigma_+ - \sigma_+\sigma_-\rho - \rho\sigma_+\sigma_-\right). \tag{3.4}$$

Finally, the third term in the master equation describes the mechanical dissipation (as described in chapter 2) of the resonator mode,

$$\begin{aligned}\mathcal{L}_{\gamma}(\rho) =& \frac{\gamma}{2}(N_{\text{th}}+1)(2a\rho a^\dagger - a^\dagger a\rho - \rho a^\dagger a)\\ &+ \frac{\gamma}{2}N_{\text{th}}(2a^\dagger\rho a - aa^\dagger\rho - \rho aa^\dagger),\end{aligned} \tag{3.5}$$

where N_{th} is the thermal equilibrium occupation number..

3.1.1 Lamb-Dicke regime

Following references [8, 82], one can go to the displaced oscillator basis by performing a (unitary) polaron transformation $H = UHU^\dagger$, defined by

$$U = e^{-iS}, \qquad S = \frac{\lambda}{2\omega_{\text{m}}}(a^\dagger + a)\sigma_z. \tag{3.6}$$

In this basis, one would obtain a Hamiltonian of the form

$$H = \hbar\omega_{\mathrm{m}} a^\dagger a - \hbar\Delta_L |e\rangle\langle e| + \frac{\hbar\Omega}{2}\left(e^{i(\lambda/\omega_{\mathrm{m}})(a^\dagger + a)}\sigma_+ + e^{-i(\lambda/\omega_{\mathrm{m}})(a^\dagger + a)}\sigma_-\right). \tag{3.7}$$

At this stage, one can define the Lamb-Dicke parameter $\eta = \lambda/\omega_{\mathrm{m}}$ and argue that for the experimentally most relevant regime $\eta \ll 1$, an approximate treatment of the system dynamics in close analogy to semiclassical laser cooling problems should also be applicable for the present system. In the following section we rigorously derive the corresponding cooling master equation in the low coupling limit by adiabatically eliminating the dynamics of the two-level system.

3.1.2 MASTER EQUATION FORMALISM

Since we are interested in the cooling processes of the resonator mode, we derive an effective master equation for its reduced density matrix. In the case where the dynamics of the two-level system is fast enough —namely when $\Gamma \gg \lambda$ and $\Gamma \gg \gamma$—, we can proceed with an adiabatic elimination of its degrees of freedom. We thus have two small parameters (compared to Γ), the effective coupling λ (Lamb-Dicke regime) and the damping rate γ of the resonator. Therefore, we can treat those processes as perturbations. In the frame rotating with ω_{m}, we write the master equation in the following restructured form

$$\dot{\rho} = \mathcal{L}_{\mathrm{A}}(\rho) + \mathcal{L}_{\lambda}(\rho) + \mathcal{L}_{\gamma}(\rho), \tag{3.8}$$

which is a more convenient form and will allow us to separate relevant and irrelevant parts and perform an *adiabatic elimination* of the atomic dynamics. The first term is of zeroth order in the two small parameters. It accounts for the total dynamics of the two-level system (unitary and relaxation)

$$\mathcal{L}_{\mathrm{A}}(\rho) = -\frac{i}{\hbar}[H_{\mathrm{A}}, \rho] + \mathcal{L}_{\Gamma}(\rho). \tag{3.9}$$

The second term correspond to first-order in λ, describing the interaction between the resonator and the two-level system

$$\mathcal{L}_\lambda(t)(\rho) = -i\lambda[(ae^{-i\omega_{\rm m}t} + a^\dagger e^{i\omega_{\rm m}t})\sigma_z, \rho]. \tag{3.10}$$

Finally, the last term, which is first order in γ, gives the dissipation of the resonator, given in equation (3.5). For cooling we are interested in the dynamics of the state of the resonator mode

$$\mu(t) = \mathrm{Tr}_{\rm A}\{\rho(t)\} \tag{3.11}$$

only, and in the following our goal is to derive an effective master equation for $\mu(t)$, by treating the couplings $\mathcal{L}_\lambda$ and $\mathcal{L}_\gamma$ in perturbation theory. In the absence of the coupling between mechanical and atomic states —as well as thermal dissipation—, the system evolves into a state

$$\rho(t) = e^{\mathcal{L}_{\rm A}t}\rho(t=0) \;\to\; \mu(t) \otimes \rho_0 \tag{3.12}$$

where ρ_0 is the steady state of the atomic dynamics, $\mathcal{L}_{\rm A}\rho_0 = 0$ (ρ_0 is the zero-eigenvalue state of the superoperator $\mathcal{L}_{\rm A}$). We define a projection operator

$$\mathcal{P}\rho = \mathrm{Tr}_{\rm A}\{\rho\} \otimes \rho_0, \qquad \mathcal{P}^2 = \mathcal{P} \tag{3.13}$$

which projects any density operator into the zero-eigenvalue subspace of $\mathcal{L}_{\rm A}$. Since ρ_0 is the only steady state of $\mathcal{L}_{\rm A}$ any other operator ρ' in the complementary subspace

$$\rho' = \mathcal{Q}\rho, \qquad \mathcal{Q} = (\mathbf{1} - \mathcal{P}), \qquad \mathcal{Q}^2 = \mathcal{Q} \tag{3.14}$$

evolves on a timescale set by the internal frequency scales Γ, Ω, Δ. In particular, any operator in the $\mathcal{Q}$-subspace will decay under the evolution of $\mathcal{L}_{\rm A}$ on a fast timescale Γ^{-1},

$$e^{\mathcal{L}_{\rm A}t}\mathcal{Q}\rho \to 0, \qquad t \gg \Gamma^{-1}. \tag{3.15}$$

Therefore, we can divide the whole density operator $\rho = \mathcal{P}\rho + \mathcal{Q}\rho$ into a slowly evolving part $\mathcal{P}\rho$ and a fast evolving part $\mathcal{Q}\rho$. Using the identity

$$(\mathcal{P}+\mathcal{Q})\dot{\rho} = (\mathcal{P}+\mathcal{Q})\left(\mathcal{L}_{\rm A}+\mathcal{L}_{\lambda}+\mathcal{L}_{\gamma}\right)(\mathcal{P}+\mathcal{Q})\rho \tag{3.16}$$

we obtain the two coupled equations, which to first order in λ and γ read

$$\textbf{(I)} \qquad \mathcal{P}\dot{\rho} \;=\; \mathcal{P}\mathcal{L}_{\lambda}\mathcal{Q}\rho + \mathcal{P}\mathcal{L}_{\gamma}\mathcal{P}\rho \tag{3.17}$$

$$\textbf{(II)} \qquad \mathcal{Q}\dot{\rho} \;=\; \mathcal{Q}\mathcal{L}_{\rm A}\mathcal{Q}\rho + \mathcal{Q}\mathcal{L}_{\lambda}\mathcal{P}\rho. \tag{3.18}$$

To derive this result we have used the fact that $\mathcal{P}\mathcal{Q} = \mathcal{P} - \mathcal{P}^2 = 0$ and since $\mathcal{L}_{\rm A}$ does not mix atomic and mechanical degrees of freedom it also follows that $\mathcal{P}\mathcal{L}_{\rm A}\mathcal{Q} = 0$, etc. and $\mathcal{L}_{\rm A}\mathcal{P}\rho$ vanishes by definition. Also, in **(I)** we have neglected a term

$$\mathcal{P}\mathcal{L}_{\lambda}\mathcal{P}\rho = -i\lambda\,\mathrm{Tr}_{\rm A}\{[(ae^{-i\omega_{\rm m}t} + a^{\dagger}e^{i\omega_{\rm m}t})\sigma_z, \mu]\} \otimes \rho_0. \tag{3.19}$$

This term simply represents a constant force on the resonator. This force can be absorbed by a shift of its equilibrium position and a redefinition of the coupling Liouvilian operator

$$\mathcal{L}_{\lambda}(t)(\rho) = -i\lambda[(ae^{-i\omega_{\rm m}t} + a^{\dagger}e^{i\omega_{\rm m}t})\bar{\sigma}_z, \rho], \tag{3.20}$$

where $\bar{\sigma}_z = \sigma_z - \langle \sigma_z \rangle$. The new coupling term then satisfies $\mathcal{P}\mathcal{L}_\lambda \mathcal{P}\rho = 0$.

ADIABATIC ELIMINATION OF THE ATOMIC STATES

The equation **(II)** for the fast subspace can be formally integrated,

$$\mathcal{Q}\rho(t) = e^{\mathcal{Q}\mathcal{L}_{\mathrm{A}}(t-t_0)}\mathcal{Q}\rho(t_0) + \int_{t_0}^{t} dt' e^{\mathcal{Q}\mathcal{L}_{\mathrm{A}}(t-t')}\mathcal{Q}\mathcal{L}_\lambda(t')\mathcal{P}\rho(t'). \tag{3.21}$$

Since for the adiabatic elimination of the NV center we are interested in timescales larger than $1/\Gamma$, we neglect the first term in the above equation. Also, the integral kernel (memory of the previous states) decays in a time-scale $1/\Gamma$, allowing us to perform the Markov approximation. Specifically, we make the variable change $t' \to t - t'$ and extend the upper limit of the integration to $t \to \infty$ (eliminating in this way the dependence on the initial state) and we replace the time t_0 in $\rho(t')$ by t. Also, without loss of generality, we make the convention $t_0 \to -\infty$ for the initial time.

$$\mathcal{Q}\rho(t) = \int_0^\infty dt' e^{\mathcal{Q}\mathcal{L}_{\mathrm{A}}t'}\mathcal{Q}\mathcal{L}_\lambda(t-t')\mathcal{P}\rho(t). \tag{3.22}$$

Now, we insert the above expression for the irrelevant part of the density matrix into equation **(I)**, obtaining,

$$\dot{\mu}(t) = \mathcal{L}_\gamma \mu + \int_0^\infty dt' \mathrm{Tr}_{\mathrm{A}}\left(\mathcal{L}_\lambda(t) e^{\mathcal{L}_{\mathrm{A}}t'}\mathcal{L}_\lambda(t-t')\mu \otimes \rho_0\right). \tag{3.23}$$

After careful calculation of the double commutator $\mathcal{L}_\lambda(t)e^{\mathcal{L}_{\mathrm{A}}t'}\mathcal{L}_\lambda(t-t')\mu \otimes \rho_0$, the above equation can be brought into the form

$$\begin{aligned}\dot{\mu}(t) =& \Big[\frac{\gamma}{2}(N_{\mathrm{th}}+1) + \frac{\Gamma_c}{2}(N_0+1)\Big](2a\mu a^\dagger - a^\dagger a\mu - \mu a^\dagger a) \\ &+ \Big[\frac{\gamma}{2}N_{\mathrm{th}} + \frac{\Gamma_c}{2}N_0\Big](2a^\dagger \mu a - aa^\dagger \mu - \mu a a^\dagger),\end{aligned} \tag{3.24}$$

where we have introduce the optical cooling rate $\Gamma_c = S(\omega_\mathrm{m}) - S(-\omega_\mathrm{m})$ and the minimal occupation number $N_0 = S(-\omega_\mathrm{m})/\Gamma_c$, which are determined by the correlation spectrum

$$S(\omega) = 2\lambda^2 \mathrm{Re} \int_0^\infty dt'(\langle \sigma_z(t')\sigma_z(0)_0\rangle - \langle \sigma_z\rangle_0^2)e^{i\omega t}. \tag{3.25}$$

From the effective master equation (3.24), one can derive the rate equation for the occupation number of the resonator mode $n_\mathrm{m}(t) = \mathrm{Tr}\{a^\dagger a \rho\}$. In the steady state of the system, the occupation number reads

$$n_0 = n_\mathrm{m}(t \to \infty) \approx \frac{\gamma N_\mathrm{th}}{\Gamma_c} + N_0. \tag{3.26}$$

Optical Bloch equations

To evaluate the cooling rate and final occupation number, we must evaluate the correlation spectrum $S(\omega)$ of the two level atom. To do so we derive the equations of motion for the expectation values of the atomic coherence

$$\partial_t \langle \sigma_- \rangle = \left(i\Delta - \frac{\Gamma}{2} \right) \langle \sigma_- \rangle + i\frac{\Omega}{2}\langle \sigma_z \rangle \tag{3.27}$$

and the population inversion

$$\partial_t \langle \sigma_z \rangle = -\Gamma\langle \sigma_z \rangle - i\Omega\langle \sigma_+ \rangle + i\Omega^*\langle \sigma_- \rangle - \Gamma. \tag{3.28}$$

Together with the conjugate equation for $\partial_t\langle \sigma_+ \rangle$ we can write these equations in a matrix form

$$\partial_t \langle \vec{S} \rangle = \mathbf{M}\langle \vec{S} \rangle - \vec{R} \tag{3.29}$$

where the dynamical matrix $\mathbf{M}$ is given by

$$\mathbf{M} = \begin{pmatrix} i\Delta - \frac{\Gamma}{2} & 0 & i\frac{\Omega}{2} \\ 0 & -i\Delta - \frac{\Gamma}{2} & -i\frac{\Omega^*}{2} \\ +i\Omega^* & -i\Omega & -\Gamma \end{pmatrix}, \qquad \vec{R} = \begin{pmatrix} 0 \\ 0 \\ \Gamma \end{pmatrix} \tag{3.30}$$

and grouped the Pauli-operators into a vector $\vec{S} = (\sigma_-, \sigma_+, \sigma_z)^T$. The set of equations (3.29) are called the optical Bloch equations (OBEs) and describe the dynamics of a driven two-level system in the presence of decay. The steady state values $\partial_t \langle S \rangle_0 = 0$ are given by

$$\langle \vec{S} \rangle_0 = \mathbf{M}^{-1} \vec{R}. \tag{3.31}$$

Explicitly, one obtains

$$\langle \sigma_- \rangle_0 = \langle \sigma_+ \rangle_0^* = \frac{\Omega(2\Delta - i\Gamma)}{4\Delta^2 + 2\Omega^2 + \Gamma^2} \tag{3.32}$$

and

$$\langle \sigma_z \rangle_0 = -1 + \frac{2\Omega^2}{4\Delta^2 + 2\Omega^2 + \Gamma^2}. \tag{3.33}$$

Evaluation of the correlation spectrum

For the evaluation of the spectrum and cooling rate, we write the spectrum as follows,

$$S(\omega) = 2\lambda^2 Re\{\vec{C}_3(s = -i\omega)\}, \tag{3.34}$$

where $\vec{C}(s)$ is the Laplace transform of $\vec{C}(\tau) = \langle \vec{S}(\tau)\sigma_z\rangle_0 - \langle \vec{S}\rangle_0 \langle \sigma_z\rangle_0$. Using the quantum regression theorem (for details see references [61, 62]), we obtain

$$\vec{C}(s) = \frac{1}{s\mathbb{I} - \mathbf{M}} \left[\begin{pmatrix} \langle \sigma_-\rangle_0 \\ -\langle \sigma_+\rangle_0 \\ 1 \end{pmatrix} - \langle \vec{S}\rangle_0 \langle \sigma_z\rangle_0 \right]. \tag{3.35}$$

The cooling rate is then given by

$$\Gamma_c = -2\lambda^2 Re \left\{ (0,0,1) \frac{1}{i\omega_m \mathbb{I} + \mathbf{M}} \left[\begin{pmatrix} \langle \sigma_-\rangle_0 \\ -\langle \sigma_+\rangle_0 \\ 0 \end{pmatrix} - \langle \vec{S}\rangle_0 \langle \sigma_z\rangle_0 \right] \right\}. \tag{3.36}$$

3.2 BASIC LASER THEORY

We consider a similar setup as in the case of cooling, discussed in the previous section. The actual phonon lasing scheme that we consider is illustrated in figure 3.1 b). This is a phonon-creation mechanism with an *effective* two-level system. Specifically, the atomic state $|e\rangle$ is pumped via excitations to a third auxiliary level $|r\rangle$. In the limit $\Gamma' \gg \Omega_p$ this process can be modeled by an incoherent pumping process from $|g\rangle$ to $|e\rangle$ with rate $\Gamma_p \approx \Omega_p^2/(2\Gamma')$. In this case we can again write a master equation of the same form as equation (3.8), namely

$$\dot{\rho} = \mathcal{L}_{\mathrm{A}}(\rho) + \mathcal{L}_{\lambda}(\rho) + \mathcal{L}_{\gamma}(\rho). \tag{3.37}$$

However, the Liouvilian operator $\mathcal{L}_{\mathrm{A}}$, associated to the atomic dynamics, is now given by

$$\mathcal{L}_{\mathrm{A}}(\rho) = \frac{\Gamma}{2}\left(2\sigma_-\rho\sigma_+ - \sigma_+\sigma_-\rho - \rho\sigma_+\sigma_-\right) + \frac{\Gamma_p}{2}\left(2\sigma_+\rho\sigma_- - \sigma_-\sigma_+\rho - \rho\sigma_-\sigma_+\right), \tag{3.38}$$

where Γ_p is the effective pumping rate. The second term in the master equation corresponds to a Jaynes-Cummings type coupling (different from what we used in the cooling section) of the form

$$\mathcal{L}_{\mathrm{A}}(\rho) = -i\lambda[(a\sigma_+ + a^\dagger\sigma_-), \rho]. \tag{3.39}$$

Finally, the third term in the master equation is the same as in the previous section and given by equation (3.5). We can now again continue with the adiabatic elimination of the atomic degrees of freedom. However, in this case, it is more convenient to derive a Fokker-Planck equation instead of an effective master equation.

3.2.1 Fokker-Planck equation

We expand the total density matrix in terms of coherent states of the harmonic oscillator, $\rho = \int d^2\alpha |\alpha\rangle\langle\alpha|\rho_{\mathrm{A}}(\alpha)$. Note that, $\rho_{\mathrm{A}}(\alpha)$ is still an operator in the atomic subspace. Taking the trace over the atomic degrees of freedom yields the reduced density matrix of the mechanics $\mu = \int d^2\alpha|\alpha\rangle\langle\alpha|P(\alpha)$ where $P(\alpha) = \mathrm{Tr}_{\mathrm{A}}\{\rho_{\mathrm{A}}(\alpha)\}$ is the Glauber-Sudarshan phase-space representation or P-distribution (for details see references [83] and [61]). The master equation for $\rho_{\mathrm{A}}(\alpha)$ is $\dot{\rho}_{\mathrm{A}}(\alpha) = \left(\mathcal{L}'_\gamma + \mathcal{L}'_{\mathrm{A}} + \mathcal{L}'_\lambda\right)\rho_{\mathrm{A}}(\alpha)$ where

$$\begin{aligned}
\mathcal{L}'_\gamma\rho_{\mathrm{A}}(\alpha) &= \frac{\gamma}{2}\left(\frac{\partial}{\partial\alpha}\alpha + \frac{\partial}{\partial\alpha^*}\alpha^*\right)\rho_{\mathrm{A}}(\alpha) + \gamma N_{\mathrm{th}}\frac{\partial^2}{\partial\alpha^*\partial\alpha}\rho_{\mathrm{A}}(\alpha)\\
&\quad + i\lambda\left(\frac{\partial}{\partial\alpha}\langle\sigma_-\rangle - \frac{\partial}{\partial\alpha^*}\langle\sigma_+\rangle\right)\rho_{\mathrm{A}}(\alpha),\\
\mathcal{L}'_{\mathrm{A}}\rho_{\mathrm{A}}(\alpha) &= \mathcal{L}_{\mathrm{A}}\rho_{\mathrm{A}}(\alpha) - i\lambda\left(\alpha^*[\sigma_-, \rho_{\mathrm{A}}(\alpha)] + \alpha[\sigma_+, \rho_{\mathrm{A}}(\alpha)]\right),\\
\mathcal{L}'_\lambda\rho_{\mathrm{A}}(\alpha) &= i\lambda\Big[\frac{\partial}{\partial\alpha}(\sigma_- - \langle\sigma_-\rangle)\rho_{\mathrm{A}}(\alpha) - \frac{\partial}{\partial\alpha^*}\rho_{\mathrm{A}}(\alpha)(\sigma_+ - \langle\sigma_+\rangle)\Big].
\end{aligned} \tag{3.40}$$

Here we have defined the stationary mean values of the atomic system's operators $\langle\sigma\rangle = \mathrm{Tr}_{\mathrm{A}}\{\sigma\rho_{\mathrm{A}}^{\mathrm{ss}}(\alpha)\}$ where $\rho_{\mathrm{A}}^{\mathrm{ss}}(\alpha)$ is the instantaneous stationary state of the atomic system defined via $\mathcal{L}'_{\mathrm{A}}\rho_{\mathrm{A}}^{\mathrm{ss}}(\alpha) = 0$

and $\mathrm{Tr}\{\rho_{\mathrm{A}}^{\mathrm{ss}}(\alpha)\} = 1$. This is reasonable because the dynamics due to $\mathcal{L}'_{\mathrm{A}}$ is much faster than the dynamics due to $\mathcal{L}'_{\gamma}$ and $\mathcal{L}'_{\lambda}$. Introducing the total gain function

$$\Gamma(\alpha) = \Gamma_{\mathrm{q}}(\alpha) - \frac{\gamma}{2}, \qquad \Gamma_{\mathrm{q}}(\alpha) = -\frac{i\lambda\langle\sigma_-\rangle}{\alpha}, \tag{3.41}$$

we may rewrite the new harmonic oscillator part as

$$\mathcal{L}'_{\gamma}\rho_{\mathrm{A}}(\alpha) = -\left(\frac{\partial}{\partial\alpha}\alpha + \frac{\partial}{\partial\alpha^*}\alpha^*\right)\Gamma(\alpha)\rho_{\mathrm{A}}(\alpha) + \gamma N_{\mathrm{th}}\frac{\partial^2}{\partial\alpha^*\partial\alpha}\rho_{\mathrm{A}}(\alpha). \tag{3.42}$$

The functional form of $\Gamma(\alpha)$ depends on the details of the atomic system's dynamics and will be evaluated after the derivation of the Fokker-Planck equation. We now observe that the coupling term $\mathcal{L}'_{\lambda}\rho_{\mathrm{A}}(\alpha)$ no longer scales with $\lambda\alpha$ but rather with $\lambda(\partial/\partial\alpha)$ and may therefore be treated as a small perturbation, even if the resonator undergoes large oscillations. Since we have already assumed that $\mathcal{L}_{\mathrm{A}}$ contains a fast relaxation rate Γ, this allows us to adiabatically eliminate the atomic system. The solution for the dynamics of the atomic system to first order is

$$\rho_{\mathrm{A}}(\alpha, t) \simeq \left[\rho_{\mathrm{A}}^{\mathrm{ss}}(\alpha) + \int_{-\infty}^{t} ds\, e^{\mathcal{L}'_{\mathrm{A}}(t-s)}\mathcal{L}'_{\lambda}\rho_{\mathrm{A}}^{\mathrm{ss}}(\alpha)\right] P(\alpha, t). \tag{3.43}$$

Inserting this into the master equation for $\rho_{\mathrm{A}}(\alpha)$ and taking the trace with respect to the atomic system's degrees of freedom yields

$$\dot{P}(\alpha) = \mathcal{L}'_{\gamma}P(\alpha, t) + \int_0^{\infty} d\tau\, \mathrm{Tr}_{\mathrm{A}}\left\{\mathcal{L}'_{\lambda}e^{\mathcal{L}'_{\mathrm{A}}\tau}\mathcal{L}'_{\lambda}\rho_{\mathrm{A}}^{\mathrm{ss}}(\alpha)\right\} P(\alpha, t). \tag{3.44}$$

A typical term in the second part of the right-hand-side reads

$$\lambda^2\frac{\partial}{\partial\alpha^*}\int_0^{\infty} d\tau\, \mathrm{Tr}_{\mathrm{A}}\left\{\bar{\sigma}_+ e^{\mathcal{L}'_{\mathrm{A}}\tau}\frac{\partial}{\partial\alpha}\bar{\sigma}_-\rho_{\mathrm{A}}^{\mathrm{ss}}(\alpha)\right\} P(\alpha, t), \tag{3.45}$$

where $\bar{\sigma} = \sigma - \langle\sigma\rangle$. To proceed, we make an approximation: we exchange the partial derivative $\partial/\partial\alpha$ with $\exp(\mathcal{L}'_{\mathrm{A}}\tau)$. These operators obviously do not commute with each other, but the corrections scale with λ and may therefore be neglected. The above term then becomes

$$\lambda^2 \frac{\partial^2}{\partial\alpha^*\partial\alpha} \int_0^\infty d\tau \, \langle\bar{\sigma}_+(\tau)\bar{\sigma}_-\rangle_{\mathrm{ss}}(\alpha) P(\alpha,t), \tag{3.46}$$

where $\langle\bar{\sigma}_+(\tau)\bar{\sigma}_-\rangle_{\mathrm{ss}} = \mathrm{Tr}_{\mathrm{A}}\{\bar{\sigma}_+ \exp(\mathcal{L}'_{\mathrm{A}}\tau)\bar{\sigma}_- \rho_{\mathrm{A}}^{\mathrm{ss}}(\alpha)\}$ is the two-time correlation function for the operators of the atomic system. We can now write down the Fokker-Planck equation for $P(\alpha,t)$:

$$\dot{P}(\alpha,t) = \left[-\left(\frac{\partial}{\partial\alpha}\alpha + \frac{\partial}{\partial\alpha^*}\alpha^* \right) \Gamma(\alpha) + \frac{\partial^2}{\partial\alpha^*\partial\alpha} D(\alpha) \right] P(\alpha,t), \tag{3.47}$$

where we have introduced the total diffusion function

$$\begin{aligned} D(\alpha) &= \gamma N_{\mathrm{th}} + D_{\mathrm{q}}(\alpha), \\ D_{\mathrm{q}}(\alpha) &= 2\lambda^2 \mathrm{Re} \int_0^\infty d\tau \, \langle\bar{\sigma}_+(\tau)\bar{\sigma}_-\rangle_{\mathrm{ss}}. \end{aligned} \tag{3.48}$$

The part γN_{th} encapsulates the effect of classical noise, whereas $D_{\mathrm{q}}(\alpha)$ that of quantum noise.

Drift and diffusion functions

The semi-classical Bloch equations for the vector $\vec{S} = (\sigma_+ \; \sigma_- \; \sigma_z)^T$ are

$$\frac{d}{dt}\langle\vec{S}(t)\rangle = \mathbf{M}\langle\vec{S}(t)\rangle - \vec{R}, \tag{3.49}$$

where

$$\vec{R} = \begin{pmatrix} 0 \\ 0 \\ \Gamma - \Gamma_p \end{pmatrix}, \qquad \mathbf{M} = \begin{pmatrix} -\frac{1}{2}\Gamma_{\mathrm{tot}} & 0 & -i\lambda\alpha^* \\ 0 & -\frac{1}{2}\Gamma_{\mathrm{tot}} & i\lambda\alpha \\ -2i\lambda\alpha & 2i\lambda\alpha^* & -\Gamma_{\mathrm{tot}} \end{pmatrix} \tag{3.50}$$

and $\Gamma_{\text{tot}} = \Gamma_p + \Gamma$. The stationary state is

$$\langle \sigma_z \rangle_{\text{ss}} = \frac{\Gamma_p^2 - \Gamma^2}{\Gamma_{\text{tot}}^2 + 8|\alpha|^2\lambda^2}, \qquad \langle \sigma_- \rangle_{\text{ss}} = \frac{2i\alpha\lambda(\Gamma_p - \Gamma)}{\Gamma_{\text{tot}}^2 + 8|\alpha|^2\lambda^2} \tag{3.51}$$

and $\langle \sigma_+ \rangle_{\text{ss}} = \langle \sigma_- \rangle_{\text{ss}}^*$. The gain function is thus $\Gamma(\alpha) = -\gamma + \Gamma_{\text{q}}(\alpha)$ where $\Gamma_{\text{q}}(\alpha)$ reads

$$\Gamma_{\text{q}}(\alpha) = \frac{\Gamma}{1 + |\alpha|^2/n_0} \tag{3.52}$$

and we have defined $\Gamma = 2\lambda^2(\Gamma_p - \Gamma)/\Gamma_{\text{tot}}^2$ and $n_0 = \Gamma_{\text{tot}}^2/8\lambda^2$. By choosing either $\Gamma_p > \Gamma$ or $\Gamma_p < \Gamma$ one obtains an effective non-linear gain or loss medium respectively with saturation threshold n_0. In order to calculate the total diffusion function we require the two-time correlation function $\langle \bar{\sigma}_+(\tau)\bar{\sigma}_- \rangle_{\text{ss}}$ where $\bar{\sigma}_i = \sigma_i - \langle \sigma_i \rangle$. Note that, $\langle (\bar{\sigma}_+ \ \bar{\sigma}_- \ \bar{\sigma}_z)^T(\tau)\bar{\sigma}_- \rangle_{\text{ss}} = \langle \vec{S}(\tau)\bar{\sigma}_- \rangle_{\text{ss}}$. By the quantum regression theorem [61, 62, 83] we obtain

$$\frac{d}{d\tau}\langle \vec{S}(\tau)\bar{\sigma}_- \rangle_{\text{ss}} = \mathbf{M}\langle \vec{S}(\tau)\bar{\sigma}_- \rangle_{\text{ss}}. \tag{3.53}$$

Recognising that the integral in (3.48) is simply the Laplace transform of $\langle \bar{\sigma}_+(\tau)\bar{\sigma}_- \rangle$ evaluated at $s = 0$, we find the total diffusion function. Explicitly, the resulting expression for N_a atoms reads

$$\begin{aligned} &D_{\text{q}}(\alpha) = \frac{4\lambda^2\Gamma_\uparrow}{\Gamma_{\text{tot}}^2} \times \\ &\frac{\Gamma_\uparrow\Gamma_{\text{tot}}^6 + 8\Gamma_\uparrow\Gamma_{\text{tot}}^3(\Gamma_\uparrow + 4\Gamma_\downarrow)\lambda^2|\alpha|^2 + 64\Gamma_{\text{tot}}^3\lambda^4|\alpha|^4 + 128\Gamma_{\text{tot}}\lambda^6|\alpha|^6}{\Gamma_\uparrow(\Gamma_{\text{tot}}^2 + 8\lambda^2|\alpha|^2)^3}. \end{aligned} \tag{3.54}$$

In the limit $\alpha \to 0$ this becomes $D_{\text{q}}(\alpha \to 0) = 4\lambda^2\Gamma_\uparrow/\Gamma_{\text{tot}}^2$ and for $\Gamma_\downarrow = 0$, which corresponds to gain, we obtain $D_{\text{q}}(\alpha \to 0) = 2\Gamma$, whilst for $\Gamma_\uparrow = 0$, which corresponds to loss, $D_{\text{q}}(\alpha \to 0) = 0$. Note that, however, in the very large amplitude limit $\alpha \to \bar{\infty}$ the diffusion function in this model approaches the constant value $D_{\text{q}}(\alpha \to \bar{\infty}) = \lambda^2/\Gamma_{\text{tot}} \approx \Gamma/2$ for both loss and gain processes.

4

Phonon cooling and lasing with nitrogen-vacancy centers in diamond

In this chapter, we investigate novel schemes for mechanical cooling and phonon lasing in diamond nano-scale beams using a single, optically-pumped NV defect. For the theoretical analysis of these schemes, the general cooling and lasing theory presented in chapter 3 is adapted for the specific level structure of the NV center, as described in chapter 2. The theory is also generalized to a Floquet representation in order to treat dispersive defect-phonon interactions. This generalization allows us to identify different cooling mechanisms and make accurate predictions for the expected cooling and gain rates in upcoming experiments. The development of these methods was done in collaboration with S. D. Bennett, S. Portolan, M. D. Lukin, P. Rabl and the theoretical results were published in Physical Review B [57]. For this work, I performed all calculations under the supervision of S. Portolan and P. Rabl.

4.1 Introduction

The basic idea of this part is illustrated by the schematic setup shown in Fig. 4.1 a), where a single NV center is embedded in a diamond nanobeam or other vibrating structure. As already described in chapter 2, section 2.2.1, the negatively charged NV^- center in diamond is formed by a substitutional nitrogen atom and an adjacent lattice vacancy; by ignoring spin degrees of freedom

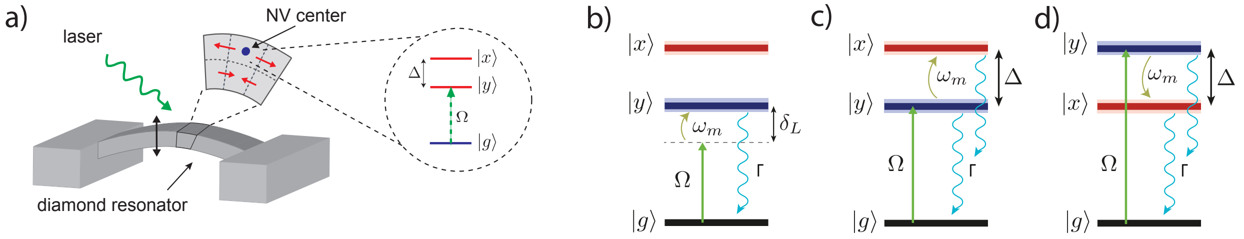

Figure 4.1 – a) Setup. A single NV$^-$ defect center is embedded in an all-diamond doubly clamped beam. Vibrations of the beam with frequency ω_m modulate the local strain and shift the energy levels of the electronically excited defect states. b)-d) Illustration of the phonon-assisted optical transitions for the case where the state $|y\rangle$ is driven by a laser of frequency ω_L and detuning $\delta_L = \omega_L - \omega_y$. The spacing between the two excited levels is defined as $\Delta = \omega_x - \omega_y$. b) Phonons coupled to $\Sigma_\parallel$ only affect the driven state $|y\rangle$ and lead to cooling (heating) effects for a laser detuning $\delta_L \approx -\omega_m$ ($\delta_L \approx +\omega_m$). c) For phonon-induced transitions between the excited states with coupling $\sim \Sigma_\perp$, a resonant cooling process occurs for $\Delta = \omega_m$ and with resonant excitation of the $|y\rangle$ state. d) For an opposite level ordering, i.e. $\Delta = -\omega_m$, the same process leads to resonant phonon emission, leading to heating and lasing effects discussed in section 4.4.

for the moment, the electronic level structure of this defect is well described by a single electronic ground state $|g\rangle$ and two optically excited states $|x\rangle \equiv |E_x\rangle$ and $|y\rangle \equiv |E_y\rangle$. Due to the C_{3v} symmetry of the NV center, the states $|x\rangle$ and $|y\rangle$ are degenerate in energy, but can be split by a few GHz in the presence of static lattice distortions or by applying external electric fields. At cryogenic temperatures, the linewidth of the excited states is sufficiently narrow such that they can be selectively addressed by laser fields of appropriate linear polarization [72, 84].

The degeneracy of the excited $|x\rangle$ and $|y\rangle$ orbitals makes these states highly susceptible to variation of the local strain near an NV center. Here, we are interested in the resulting coupling of the NV center to the quantized strain field associated with a single resonant vibrational mode of a diamond structure. In general, the strain field induced by this mode will break the symmetry of the NV center and cause energy shifts as well as a mixing of the states $|x\rangle$ and $|y\rangle$. As shown in more detail in section 2.3.1, the resulting NV-phonon coupling is of the form ($\hbar = 1$)

$$H_{\mathrm{NV-ph}} \simeq \left(\lambda_\parallel \Sigma_\parallel + \lambda_\perp \Sigma_\perp\right)(a^\dagger + a), \tag{4.1}$$

where a and $a^\dagger$ are the annihilation and creation operators for the vibrational mode and $\Sigma_\parallel = |x\rangle\langle x| - |y\rangle\langle y|$ and $\Sigma_\perp = |x\rangle\langle y| + |y\rangle\langle x|$ are the operators associated with a relative energy shift and a mixing between the excited states, respectively. As discribed in section 2.3.1, the coupling constants $\lambda_\parallel$ and $\lambda_\perp$ can reach values of several MHz. This is comparable to the radiative lifetime Γ of the excited states and can be even stronger in smaller structures [21, 28]. More importantly for the present work, the strength of the NV phonon coupling can by far exceed the mechanical damping rate $\gamma_m = \omega_m/Q$, which for realistic mechanical quality factors of $Q = 10^5 - 10^6$ is in the kHz regime.

4.2 MODEL

For the cooling and lasing effects discussed below we assume that the NV center is driven by a near resonant laser of frequency ω_L. For concreteness we assume that the excitation laser is linearly polarized along the y axis and detuned from the state $|y\rangle$ by δ_L. In the frame rotating with the laser frequency the resulting effective model Hamiltonian for our system is ($\hbar = 1$)

$$H = \omega_m a^\dagger a - \delta_L |y\rangle\langle y| - (\delta_L - \Delta)|x\rangle\langle x| + \frac{\Omega}{2}(|y\rangle\langle g| + |g\rangle\langle y|) + \lambda\bar{\Sigma}(a + a^\dagger), \tag{4.2}$$

where we have introduced the short notation $\lambda\bar{\Sigma} \equiv \sum_{\nu=0,\parallel,\perp} \lambda_\nu \Sigma_\nu$ and $\Delta = \omega_x - \omega_y \sim 1$ GHz is the frequency splitting between the two excited states $|x\rangle$ and $|y\rangle$ due to static lattice distortions. This splitting can be tuned by applying external electric fields [85] and in the following we treat Δ as an adjustable parameter.

To account for dissipation due to radiative and mechanical losses we model the system dynamics by the master equation

$$\dot{\rho} = -i\,[H, \rho] + \mathcal{L}_\Gamma \rho + \mathcal{L}_\gamma \rho, \tag{4.3}$$

for the system density operator ρ. The Liouville operator $\mathcal{L}_\Gamma$ is given by

$$\begin{aligned}\mathcal{L}_\Gamma\rho =& \frac{\Gamma}{2}\sum_{\xi=x,y}(2|g\rangle\langle\xi|\rho|\xi\rangle\langle g| - |\xi\rangle\langle\xi|\rho - \rho|\xi\rangle\langle\xi|) \\ &+ \frac{\Gamma_\phi}{2}\sum_{\xi=x,y}(2|\xi\rangle\langle\xi|\rho|\xi\rangle\langle\xi| - |\xi\rangle\langle\xi|\rho - \rho|\xi\rangle\langle\xi|),\end{aligned} \tag{4.4}$$

and describes the radiative decay of the excited states with an approximately equal decay rate $\Gamma/(2\pi) \approx 15$ MHz as well as an additional broadening $\sim \Gamma_\phi$ of the optical transitions due to spectral diffusion. In bulk diamond and low temperatures of $T < 10$ K, narrow optical lines with $\Gamma_\phi \sim \Gamma$ can be achieved [24, 86]. For shallow implanted NVs, surface impurities induce additional dephasing and significant experimental effort is devoted to understanding and mitigating this additional dephasing. For NV centers located a few tens of nanometers away from the surface, it is expected that sufficiently narrow lines with $\Gamma_\phi \lesssim 100$ MHz can be reached.

The last term in equation (4.3) describes mechanical dissipation due to the coupling of the resonant vibrational mode to the thermal bath of phonon modes in the support and it is given by equation (3.5). For mechanical frequencies $\omega_m/(2\pi) \approx 1$ GHz and realistic values of $Q \approx 10^5 - 10^6$ [17, 18] the corresponding damping rates are a few kHz and $N_{th} \approx 100$ at $T = 4$ K.

4.3 Ground state cooling of a mechanical resonator

In this section we apply the cooling theory of section 3.1 to the case of the NV center. We will first focus on the cooling effects induced by the $\sim \Sigma_\parallel$ and $\sim \Sigma_\perp$ type interactions and evaluate the conditions for ground state cooling of the mechanical mode.

4.3.1 Cooling: Theory

For the parameters of interest $\lambda < \Gamma$ and low mechanical occupation numbers, the dynamics of the NV center is only weakly perturbed by the phonon mode. This allows us to adiabatically eliminate the NV center degrees of freedom and derive an effective equation of motion for the mechanical degrees of freedom only [8, 9, 12, 82, 87, 88]. To do so, we follow the steps outlined in section 3.1 with NV-phonon coupling given by the Liouvilian

$$\mathcal{L}_\lambda \rho = -i\lambda[\bar{\Sigma}(ae^{-i\omega_m t} + a^\dagger e^{i\omega_m t}), \rho] \tag{4.5}$$

and we obtain the effective master equation for the mechanical mode [12, 82, 87]

$$\dot{\rho}_m = \mathcal{L}_\gamma \rho_m + \frac{\tilde{\Gamma}}{2}(N_0 + 1)\mathcal{D}[a]\rho + \frac{\tilde{\Gamma}}{2} N_0 \mathcal{D}[a^\dagger]\rho. \tag{4.6}$$

Here we have introduced the cooling rate $\tilde{\Gamma} = 2\lambda^2(\mathrm{Re}[S(\omega_m)] - \mathrm{Re}[S(-\omega_m)])$ and the minimal occupation number $N_0 = \mathrm{Re}[S(-\omega_m)]/(\mathrm{Re}[S(\omega_m)] - \mathrm{Re}[S(-\omega_m)])$, which are determined by the equilibrium fluctuation spectrum

$$S(\omega_m) = \int_0^\infty dt' \langle \bar{\Sigma}(t')\bar{\Sigma}(0)\rangle e^{i\omega_m t'}, \tag{4.7}$$

where $\langle\cdot\rangle$ denotes the average with respect to the stationary NV center state ρ_0.

To describe the dynamics of the NV center we use $\sigma_{gg} = \mathbf{1} - \sigma_{xx} - \sigma_{yy}$ and group the remaining independent expectation values into a vector, $\langle\vec{\chi}\rangle = (\langle\sigma_{xx}\rangle, \langle\sigma_{yy}\rangle, \langle\sigma_{gx}\rangle, \langle\sigma_{gy}\rangle, \langle\sigma_{xg}\rangle, \langle\sigma_{xy}\rangle, \langle\sigma_{yg}\rangle, \langle\sigma_{yx}\rangle)^T$. The expectation values evolve according to the Bloch equation

$$\langle\dot{\vec{\chi}}\rangle = \mathbf{M}\langle\vec{\chi}\rangle + \vec{V}, \tag{4.8}$$

where $\vec{V} = (0,0,0,-i\Omega/2,0,0,i\Omega/2,0)^T$ and the matrix $\mathbf{M}$ is explicitly given by

$$\mathbf{M} = \begin{pmatrix} -\Gamma & 0 & 0 & 0 & 0 & 0 & 0 & 0 \\ 0 & -\Gamma & 0 & i\frac{\Omega}{2} & 0 & 0 & -i\frac{\Omega}{2} & 0 \\ 0 & 0 & i(\delta_L-\Delta)-\frac{\Gamma}{2} & 0 & 0 & 0 & 0 & i\frac{\Omega}{2} \\ i\frac{\Omega}{2} & i\Omega & 0 & i\delta_L-\frac{\Gamma}{2} & 0 & 0 & 0 & 0 \\ 0 & 0 & 0 & 0 & -i(\delta_L-\Delta)-\frac{\Gamma}{2} & -i\frac{\Omega}{2} & 0 & 0 \\ 0 & 0 & 0 & 0 & -i\frac{\Omega}{2} & i\Delta-\Gamma & 0 & 0 \\ -i\frac{\Omega}{2} & -i\Omega & 0 & 0 & 0 & 0 & -i\delta_L-\frac{\Gamma}{2} & 0 \\ 0 & 0 & i\frac{\Omega}{2} & 0 & 0 & 0 & 0 & -i\Delta-\Gamma \end{pmatrix}.$$

For the evaluation of the cooling rate $\tilde{\Gamma}$ and the effective occupation number N_0, we need to calculate the spectrum $S(\omega_m)$ given in equation (4.7), which fully determines the cooling dynamics in the Lamb-Dicke regime. This is done using the quantum regression theorem [61, 62], and we obtain

$$S(\omega_m) = -\left(\frac{\lambda_0+\lambda_\parallel}{\lambda}, \frac{\lambda_0-\lambda_\parallel}{\lambda}, 0,0,0, \frac{\lambda_\perp}{\lambda}, 0, \frac{\lambda_\perp}{\lambda}\right) \frac{1}{i\omega_m\mathbf{1}+\mathbf{M}} \left(\langle\vec{\chi}\bar{\Sigma}\rangle_{ss} - \langle\vec{\chi}\rangle_{ss}\langle\bar{\Sigma}\rangle_{ss}\right). \tag{4.9}$$

From equation (4.6), the mean occupation number $\langle n\rangle = \langle a^\dagger a\rangle$ of the phonon mode satisfies

$$\partial_t\langle n\rangle = -\tilde{\Gamma}\left(\langle n\rangle - n_f\right), \tag{4.10}$$

where for $\tilde{\Gamma} \gg \gamma$ and $N_{th} \gg 1$ the final occupation number n_f is approximately given by equation (3.26). In the following discussion we are mainly interested in the sideband resolved regime $\Gamma, \Gamma_\phi \ll \omega_m$ where $N_0 \ll 1$ can be neglected. The final mode occupation number is then determined by the competition between the optical cooling rate $\tilde{\Gamma}$ and the rethermalization rate $\gamma N_{\rm th}$.

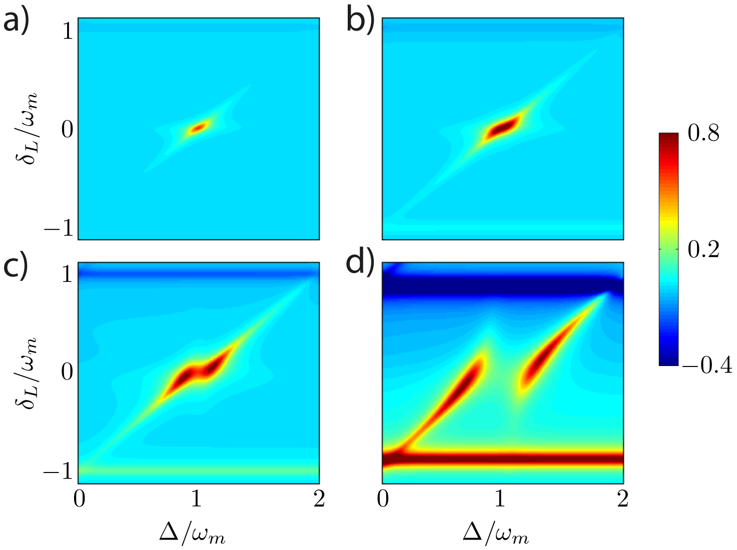

Figure 4.2 – Density plots of the Lamb-Dicke cooling rate (in units of λ^2/Γ) as a function of the detuning δ_L (y-axis) and the frequency difference Δ of the excited levels (x-axis) for four different values of the Rabi frequency: a) $\Omega/\Gamma = 0.5$, b) $\Omega/\Gamma = 1$, c) $\Omega/\Gamma = 2$ and d) $\Omega/\Gamma = 5$. For all plots it has been assumed that $\lambda_\perp = \lambda_\parallel = \lambda$, $\lambda_0 = 0$ and $\Gamma_\phi = 0$.

4.3.2 COOLING: RESULTS AND DISCUSSION

In figure 4.2 we numerically evaluate the cooling rate $\tilde{\Gamma}$ and plot the result as a function of Δ and δ_L and different values of the driving strength Ω. We find regions of strong cooling around $\delta_L \approx -\omega_m$ and around $\delta_L \approx 0$, $\Delta \approx \omega_m$, which can be associated with the two excitation processes indicated in figure 4.1 b) and c), respectively. In the first case the laser is tuned on the red sideband of the $|g\rangle \rightarrow |y\rangle$ transition and a mechanical energy of $\hbar\omega_m$ is absorbed to make this transition resonant. In the second case the laser excites the state $|y\rangle$ on resonance, and by absorbing an additional phonon, the NV center is further excited to the state $|x\rangle$ before it decays. For large $\Omega > \Gamma$, the cooling maximum is separated into two peaks as a result of the strong Rabi splitting.

Figure 4.2 shows that while at larger driving powers $\Omega \approx \omega_m$ both cooling mechanisms lead to appreciable rates of $\tilde{\Gamma} \sim \mathcal{O}(\lambda^2/\Gamma)$, the mechanism related to Σ_0- or $\Sigma_\parallel$-type coupling is strongly reduced at lower Rabi frequencies. To see this more explicitly we evaluate the cooling rate $\tilde{\Gamma}$ under weak-driving conditions ($\Omega < \Gamma, \omega_m$) and for the two types of couplings $\sim \Sigma_\parallel$ and $\sim \Sigma_\perp$ separately. In the first case we obtain

$$\tilde{\Gamma}_\parallel = \frac{4\Gamma\lambda_\parallel^2\Omega^2}{\Gamma^2 + 4\delta_L^2}\left[\frac{1}{\Gamma^2 + 4(\omega_m + \delta_L)^2} - \frac{1}{\Gamma^2 + 4(\omega_m - \delta_L)^2}\right], \tag{4.11}$$

in agreement with previous results for phonon-cooling schemes with two-level systems [82]. For sideband resolved conditions, $\Gamma \ll \omega_m$, this cooling rate is optimized for $\delta_L = -\omega_m$ and with a maximal value given by

$$\tilde{\Gamma}_\parallel \approx \frac{\lambda_\parallel^2}{\Gamma}\frac{\Omega^2}{\omega_m^2}. \tag{4.12}$$

On the other hand, by considering only the Σ_x coupling we obtain

$$\tilde{\Gamma}_\perp = \frac{4\Gamma\lambda_\perp^2\Omega^2}{\Gamma^2 + 4\delta_L^2}\left[\frac{1}{\Gamma^2 + 4(\Delta - \omega_m - \delta_L)^2} - \frac{1}{\Gamma^2 + 4(\Delta + \omega_m - \delta_L)^2}\right]. \tag{4.13}$$

Again under side-band resolved conditions, the maximal rate in this case occurs for $\delta_L = 0$ and $\Delta = \omega_m$, where the maximal value is given by

$$\tilde{\Gamma}_\perp \approx \frac{\lambda_\perp^2}{\Gamma}\frac{4\Omega^2}{\Gamma^2}. \tag{4.14}$$

We see that the requirement to maximize the cooling rate is now only $\Omega \sim \Gamma$, which corresponds to a saturation of the state $|y\rangle$ on resonance. This is a significant improvement compared to the much stronger requirement $\Omega \sim \omega_m$ in equation (4.12) when the mechanical frequency is high, $\omega_m \gg \Gamma$. For example, by comparing equations (4.12) and (4.14) for typical parameters considered in this work and assuming $\lambda_\perp \sim \lambda_\parallel$, we find that the optimal cooling rate for the same Ω is improved by a factor

$$\frac{\tilde{\Gamma}_\perp}{\tilde{\Gamma}_\parallel} \approx \frac{4\omega_m^2}{\Gamma^2} \approx 10^4. \tag{4.15}$$

In other words, the laser power that is needed to achieve the same cooling rate can be a factor 10^4 lower when making use of the multi-level structure of the NV center. This difference in the scaling has important practical implication when the laser power is limited by heating of the sample or by two-photon charging effects [89, 90]. Therefore, the near degenerate excited state manifold of the NV defect can provide a crucial ingredient for a first experimental demonstration of strain induced cooling effects for nanomechanical systems.

As mentioned above, the final occupation number n_f in the sideband resolved regime is mainly determined by the competition between the cooling rate $\tilde{\Gamma}$ and the rethermalization rate $\gamma N_{\mathrm{th}} \simeq k_B T/(\hbar Q)$. Under optimal driving the maximal achievable cooling rate approaches $\tilde{\Gamma}^{\max} \approx \bar{\lambda}^2/\Gamma$. This happens for laser powers $\Omega \sim \omega_m$ for the $\Sigma_\parallel$-type coupling and for $\Omega \sim \Gamma$ for the $\Sigma_\perp$-type coupling. The minimal achievable occupation numbers are then approximately given by $n_f \approx \gamma N_{\mathrm{th}} \Gamma/\lambda^2$. For $\lambda/(2\pi) \approx 5$ MHz, ground state cooling $n_f \lesssim 1$ can be achieved for realistic mechanical quality factors of $Q \approx 10^5$ and initial temperature of $T = 4$ K.

In our analysis so far we have considered the ideal case of purely radiatively broadened optical lines $\Gamma > \Gamma_\phi$, which is a realistic assumption in bulk diamond and at temperatures of a few Kelvin. In nanoscale structures, noise processes on the surface become important and can lead to additional spectral diffusion of the optical line. For the cooling to remain efficient, we require that $\Gamma_\phi < \omega_m$, such that the phonon sidebands are still well resolved. Based on rapid progress with shallow-implanted NVs and expected line widths of $\Gamma_\phi \sim 200$ MHz, this condition can be realistically achieved for $\sim$ GHz mechanical modes. Since spectral diffusion broadens the line without causing dissipation, the cooling rate is reduced by a factor $\tilde{\Gamma} \sim \Gamma/(\Gamma_\phi + \Gamma)$. This slightly degrades the cooling, but does not affect the mechanism itself.

It is important to point out that in our model in equations (4.4) a simple Markovian linebroading $\sim \Gamma_\phi$ is assumed. In practice the spectral diffusion of the excited states is often better described by a highly non-Marokvian, slow drift of the excited state energies. This can in principle be compensated by applying additional optical dressing or real-time feedback schemes to stabilize the optical transitions and a reduction of the remaining broadening to $\Gamma_\phi \sim \Gamma$ seems feasible.

4.4 Phonon lasing with nitrogen vacancy centers

As a second application we now consider the opposite regime, where the detuning of the optical driving field is chosen to enhance phonon emission processes. At low driving powers this simply leads to an increase of the mechanical energy, but at larger driving strengths the heating can overcome the intrinsic mechanical damping and drive the resonator into a large amplitude coherent state. In analogy to a strongly pumped optical mode undergoing a lasing transition, this effect is commonly referred to as 'phonon lasing' and has been investigated in different physical settings [34–42]. While mechanical systems can in principle be driven into a coherent state by applying a resonant external force, this becomes increasingly more difficult for high-frequency modes in small structures. In contrast to the cooling mechanism discussed above, the phonon-lasing scheme we now discuss amplifies the mechanical motion, providing an efficient way to probe NV-phonon interactions.

4.4.1 Semiclassical phonon-lasing theory

In the previous section we derived an effective rate equation for the resonator mode under the assumption $\lambda\sqrt{\langle n\rangle} \ll \Gamma$. In the opposite regime of amplification, the mean resonator occupation $\langle n\rangle$ can become very high and non-linear saturation effects —which eventually limit the maximal achievable occupation number— become important. Still assuming $\lambda \ll \Gamma$ these effects can be described within a semiclassical approach [83], where the effect of a large classical phonon amplitude $\sim \lambda\sqrt{\langle n\rangle}$ on the NV center dynamics is taken fully into account.

In section 3.2.1, the basic theory of lasers was discussed. Here we closely follow the phase-space approach, which was used in reference [82] to model phonon cooling effects at high initial temperatures, in order to account for the more general dispersive NV-phonon coupling. We introduce a set of quasi-probability distributions

$$P_{jk}(\alpha, t) = \frac{1}{\pi^2} \int d^2\beta \, e^{\alpha\beta^* - \alpha^*\beta} \mathrm{Tr} \left\{ e^{\beta a^\dagger} e^{-\beta^* a} \sigma_{jk} \rho(t) \right\}, \tag{4.16}$$

where $\sigma_{jk} = |j\rangle\langle k|$ and $j, k = g, x, y$. The $P_{jk}(\alpha, t)$ correspond to the expectation value of the operator σ_{jk} for a fixed coherent state amplitude α and $\langle \sigma_{jk} \rangle(t) = \int P_{jk}(\alpha, t) d^2\alpha$. The function $P(\alpha, t) = P_{gg}(\alpha, t) + P_{xx}(\alpha, t) + P_{yy}(\alpha, t)$ is the usual Glauber-Sudarshan P representation [61, 62, 83] of the mechanical resonator density matrix.

In the frame rotating with ω_m, the state of the mechanical mode changes slowly on the relaxation timescale Γ^{-1} of the NV excited states. This allows us to evaluate the quasi-stationary values of $P_{ij}(\alpha, t)$ for a fixed point α in phase space, and insert the result back into the equation of motion for the P-representation $P(\alpha, t)$. Starting from the set of distribution functions defined in equation (4.16), we use $P_{gg} = P - P_{xx} - P_{yy}$, and define a vector $\vec{P} = (P_{xx}, P_{yy}, P_{gx}, P_{gy}, P_{xg}, P_{xy}, P_{yg}, P_{yx})^T$, which for $\lambda \to 0$ evolves according to

$$\dot{\vec{P}}(\alpha, t) = \mathbf{M}\vec{P}(\alpha, t) + \vec{V} P(\alpha, t) + D_\gamma \vec{P}(\alpha, t). \tag{4.17}$$

The first two terms on the right-hand side correspond to the dissipative evolution of the NV center and $\mathbf{M}$ and $\vec{V}$ have been previously defined. The third term accounts for the mechanical damping of the oscillator, where

$$D_\gamma \vec{P}(\alpha,t) = \frac{\gamma}{2}\left(\frac{\partial}{\partial\alpha}\alpha + \frac{\partial}{\partial\alpha^*}\alpha^*\right)\vec{P}(\alpha,t) + \gamma N_{\mathrm{th}}\frac{\partial^2}{\partial\alpha\partial\alpha^*}\vec{P}(\alpha,t). \tag{4.18}$$

The coupling between the mechanical mode and the NV center is described by the term $\dot{\rho}(t) = -i[H_\lambda, \rho(t)]$ in the master equations, where the interaction Hamiltonian is $H_\lambda = \lambda\bar{\Sigma}(ae^{-i\omega_m t} + a^\dagger e^{i\omega_m t})$ and

$$\bar{\Sigma} = \frac{\lambda_\perp}{\lambda}\left(\sigma_{xy} + \sigma_{yx}\right) + \frac{\lambda_0 + \lambda_\parallel}{\lambda}\sigma_{xx} + \frac{\lambda_0 - \lambda_\parallel}{\lambda}\sigma_{yy}. \tag{4.19}$$

This coupling add the following terms to the equations of motion for the P-functions,

$$\dot{P}_{\sigma_{jk}} = -i\lambda\left(\alpha e^{-i\omega_m t} + \alpha^* e^{i\omega_m t}\right)P_{[\sigma_{jk},\bar{\Sigma}]} + i\lambda e^{i\omega_m t}\frac{\partial}{\partial\alpha}P_{\bar{\Sigma}\times\sigma_{jk}} - i\lambda e^{-i\omega_m t}\frac{\partial}{\partial\alpha^*}P_{\sigma_{jk}\times\bar{\Sigma}}, \tag{4.20}$$

where $P_{\sigma_{jk}} \equiv P_{jk}$. To remove the explicit time dependence we introduce a Floquet representation

$$P_{jk}(\alpha,t) = \sum_{n=-\infty}^{\infty} P_{jk}^n(\alpha,t)e^{-in\omega_m t}, \tag{4.21}$$

and we obtain

$$\dot{P}_{\sigma_{jk}}^n = i\omega_m n P_{\sigma_{jk}}^n - i\lambda\left(\alpha P_{[\sigma_{jk},\bar{\Sigma}]}^{n+1} + \alpha^* P_{[\sigma_{jk},\bar{\Sigma}]}^{n-1}\right) + i\lambda\frac{\partial}{\partial\alpha}P_{\bar{\Sigma}\times\sigma_{jk}}^{n+1} - i\lambda\frac{\partial}{\partial\alpha^*}P_{\sigma_{jk}\times\bar{\Sigma}}^{n-1}. \tag{4.22}$$

By replacing in this equation σ_{jk} by the identity operator **1**, we get the corresponding equation for the resonator P-function, which by including the mechanical damping, is given by

$$\dot{P}^n = D_\lambda P^n + i\omega_m n P^n + i\lambda\left(\frac{\partial}{\partial\alpha}P^{n+1}_{\bar{\Sigma}} - \frac{\partial}{\partial\alpha^*}P^{n-1}_{\bar{\Sigma}}\right). \tag{4.23}$$

For the other P-distributions we obtain

$$\begin{aligned}\dot{\vec{P}}^n =&(\mathbf{M} + i\omega_m n)\vec{P}^n + \vec{V}P^n + D_\gamma \vec{P}^n + i\lambda\left(\alpha\mathbf{A}\vec{P}^{n+1} + \alpha^*\mathbf{A}\vec{P}^{n-1}\right)\\ &+ i\lambda\frac{\partial}{\partial\alpha}\mathbf{B}\vec{P}^{n+1} - i\lambda\frac{\partial}{\partial\alpha^*}\mathbf{B}^\dagger\vec{P}^{n-1},\end{aligned} \tag{4.24}$$

where the 8×8 matrices **A** and **B** can be derived from equation (4.22). Following reference [82] we solve this set of equations by using $\lambda\times\partial/\partial\alpha$ as a formal expansion parameter, while keeping all orders in $\lambda\alpha$. To zeroth order, and assuming $\gamma N_{th} \ll \Gamma$ the stationary solution of equation (4.24) is given by

$$(\mathbf{M} + i\omega_m n)\vec{P}^n + i\lambda\left(\alpha\mathbf{A}\vec{P}^{n+1} + \alpha^*\mathbf{A}\vec{P}^{n-1}\right) = -\vec{V}P^n\delta_{n,0}. \tag{4.25}$$

We can numerically solve this equation by truncating the maximal value of n and write the result as

$$\vec{P}^n(\alpha,t) = \vec{X}^n(\alpha)P^0(\alpha,t). \tag{4.26}$$

By inserting this solution back into equation (4.23) we obtain

$$\dot{P}^0 = D_\gamma P^0 + i\lambda\left(\frac{\partial}{\partial\alpha}\bar{X}^{+1} - \frac{\partial}{\partial\alpha^*}\bar{X}^{-1}\right)P^0, \tag{4.27}$$

where

$$\bar{X}^n = \left(\frac{\lambda_0+\lambda_\parallel}{\lambda}, \frac{\lambda_0-\lambda_\parallel}{\lambda}, 0, 0, 0, \frac{\lambda_\perp}{\lambda}, 0, \frac{\lambda_\perp}{\lambda}\right)\vec{X}^n. \tag{4.28}$$

Now, we define parameters $\tilde{\Gamma}(\alpha)$ and $\Delta(\alpha)$ such that $i\lambda\bar{X}^{+1} = \alpha[\tilde{\Gamma}(\alpha) + i\Delta(\alpha)]$. Then the above equation reads

$$\dot{P}^0 = D_\gamma P^0 + \frac{1}{2}\left(\frac{\partial}{\partial\alpha}\alpha[\tilde{\Gamma}(\alpha) + i\Delta(\alpha)] + H.c.\right)P^0. \tag{4.29}$$

$\Delta(\alpha)$ corresponds to a small frequency shift and will be from now on neglected. By including in equation (4.25) the next order correction $\sim \lambda \times \partial P^0/\partial\alpha$ we would in equation (4.29) obtain additional correction to the diffusion terms [82]. However, a numerical estimate shows that these corrections are negligible for the high temperatures $N_{\text{th}} \gg 1$ and other parameters considered in this work, but must be taken into account when studying lasing effects at low thermal occupation numbers $N_{\text{th}} \sim 1$ [34–36, 39, 42]. Finally, we can write the effective Fokker-Planck equation for the mechanical mode as follows,

$$\dot{P}(\alpha,t) \simeq \frac{1}{2}\left(\frac{\partial}{\partial\alpha}\alpha\gamma(\alpha) + \frac{\partial}{\partial\alpha^*}\alpha^*\gamma(\alpha)\right)P(\alpha,t) + \gamma N_{\text{th}}\frac{\partial^2}{\partial\alpha\partial\alpha^*}P(\alpha,t), \tag{4.30}$$

where $\gamma(\alpha) = \tilde{\Gamma}(\alpha) + \gamma$. In the limit $\alpha \to 0$ the energy-dependent damping rate $\tilde{\Gamma}(\alpha) \equiv \tilde{\Gamma}(|\alpha|)$ reduces to $\tilde{\Gamma}$ defined below equation (4.6), and must be in general evaluated numerically.

Equation (4.30) preserves the radial symmetry of the initial thermal state; thus, by writing $\alpha = re^{i\phi}$, we can rewrite it in terms of a Fokker-Planck equation for the radial distribution,

$$\dot{P}(r,t) = \frac{1}{2}\left(\frac{\partial}{\partial r}r + 1\right)\gamma(r)P(r,t) + \frac{\gamma N_{\text{th}}}{4}\left(\frac{\partial^2}{\partial r^2} + \frac{1}{r}\frac{\partial}{\partial r}\right)P(r,t). \tag{4.31}$$

The steady-state solution of the radial equation is $P(r,\infty) = \mathcal{N}e^{-\phi(r)}$, where $\mathcal{N}$ is a normalization constant such that $2\pi\int_0^\infty rP(r)dr = 1$ and

$$\phi(r) = \frac{2}{\gamma N_{\text{th}}}\int_0^r r'\gamma(r')dr. \tag{4.32}$$

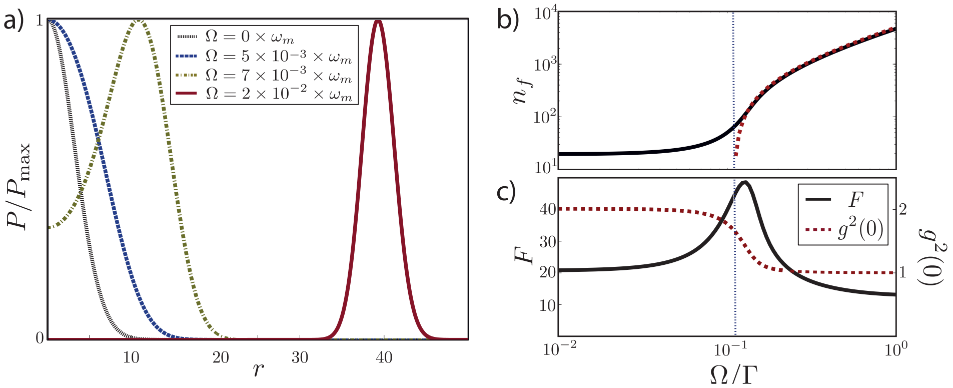

Figure 4.3 – a) The stationary P-function $P(r, \infty)$ is plotted for different values of the Rabi frequency Ω given in the inset. Each curve is rescaled by its maximal value $P_{\rm max}$ and the other parameters used for this plot are (in units of ω_m), $N_{\rm th} = 20$, $\gamma = 10^{-6}$, $\lambda_\perp = 0.001$, $\Gamma = 0.05$ and $\Gamma_\phi = 0$. b) The final phonon occupation number n_f is plotted as a function of Ω and other parameters as in a). The dashed line indicates the approximate result derived from the Gaussian P-function given in equation (4.37). c) Under the same conditions the Fano factor F (solid line) and the correlation function $g^2(0)$ (dashed line) are plotted as a function of the driving strength. In b) and c) the vertical dashed line indicates the position of the threshold given in equation (4.36).

In the absence of driving, $\gamma(r) = \gamma$ and we obtain the thermal distribution function $P(r, \infty) = e^{-r^2/N_{\rm th}}/(\pi N_{\rm th})$. For the cooling schemes described in section 4.3, we obtain $\tilde{\Gamma}(r \to 0) = \tilde{\Gamma} > 0$, but $\tilde{\Gamma}(r)$ decreases at larger values of r, where saturation effects set in and limit the cooling effect [82]. In the following, we are mainly interested in detuning such that for low occupations, $\gamma(r \to 0) < 0$ and energy is pumped into the mechanical mode. Again, due to saturation, this heating decreases at large oscillation amplitudes, where eventually $\gamma(r \to \infty) = \gamma > 0$.

4.4.2 From heating to lasing

In the previous section we have shown that resonant phonon interactions $\sim \Sigma_\perp$ provide an efficient way to cool high frequency phonons, and in the following we analyze the reverse process of phonon lasing. To do so, we set $\Delta \approx -\omega_m$ and obtain the inverted level structure shown in figure 4.1 d), where the driving laser excites the upper state $|y\rangle$, which can undergo a further transition to the lower state $|x\rangle$ by emitting a phonon.

In figure 4.3 a) we present the numerically-calculated P-functions for different values of the driving strength Ω. For very low driving, the optical heating rate is still smaller than the intrinsic mechanical damping rate. In this case the resonator mode remains in a thermal state, but with a higher effective temperature. Above a threshold driving strength, $\Omega > \Omega_c$, the P-function starts to deviate from a thermal distribution and reaches its maximum at a finite value $r_0 > 0$. This is the onset of the lasing transition. By further increasing Ω, the maximum shifts to larger and larger values and the P-function displays a narrow Gaussian shape, which approximates the sharp δ-function, $P(r) \sim \delta(r - r_0)$, expected for an ideal coherent state.

To further characterize the phonon lasing phenomenon, we plot in figure 4.3 b) the final phonon occupation number n_f as a function of Ω, starting from an equilibrium value of $N_{\rm th} = 20$. We see that around $\Omega_c/\Gamma \approx 0.11$ the phonon number starts to increase significantly; for the chosen parameters, it can reach values up to $n_f \approx 10^4$. In figure 4.3 c) we show the corresponding values for $g^2(0) = \langle a^\dagger a^\dagger a a\rangle / \langle n\rangle^2$ and the Fano factor $F = \langle n^2\rangle / \langle n\rangle$, which also show clear signatures of the transition from heating to lasing. For $\Omega < \Omega_c$ the Fano factor remains close to $F \approx n_f + 1$, as expected for a thermal distribution. Above Ω_c the Fano factor starts to decrease, indicating a more Poisson-like distribution. This is even more apparent by looking at $g^2(0)$, which changes from a value of $g^2(0) = 2$ for a thermal state to $g^2(0) \simeq 1$ of a coherent state.

Note that an increase of the driving strength $\Omega > \Gamma$ leads to a saturation of the optical transition and therefore also the lasing effect. In addition, for a very strong driving field $\Omega \gg \Gamma$, but otherwise fixed detunings, the resulting Rabi splitting between $|g\rangle$ and $|y\rangle$ will drive the system out of the resonance condition and the lasing effect breaks down.

Under weak driving conditions ($\Omega < \Gamma, \omega_m$) and assuming a dominantly $\Sigma_\perp$ coupling, we derive an approximate analytical form for the heating rate, which on resonance ($\Delta = \omega_m$, $\delta_L = 0$) is given by

$$\tilde{\Gamma}_{\perp}(r) = \frac{-4\lambda_{\perp}^2 \Gamma \Omega^2}{(\Gamma^2 + 4\lambda_{\perp}^2 r^2)^2}. \tag{4.33}$$

By direct integration of equation (4.32) we obtain

$$\phi(r) = \frac{r^2}{N_{\text{th}}} \left(1 - \frac{4\lambda_{\perp}^2 \Omega^2}{\gamma\Gamma(\Gamma^2 + 4\lambda_{\perp}^2 r^2)}\right), \tag{4.34}$$

and the position of the maximum of the P-function is found by solving $\phi'(r_0) = 0$,

$$r_0 = \frac{1}{2}\sqrt{-\frac{\Gamma^2}{\lambda_{\perp}^2} + \frac{2\sqrt{\Gamma}\Omega}{\sqrt{\gamma}\lambda_{\perp}}}. \tag{4.35}$$

Setting r_0 to zero yields the lasing-threshold,

$$\frac{\Omega_c}{\Gamma} = \frac{\sqrt{\Gamma\gamma}}{2\lambda_{\perp}}, \tag{4.36}$$

which is indicated in figure 4.3 by the vertical dotted line. Deep in the lasing regime, where $r_0 \gg 1$, we can further make a saddle-point approximation and obtain a Gaussian P-distribution of the form

$$P(r) \approx \frac{1}{r_0 \sigma \sqrt{8\pi^3}} e^{-\frac{(r-r_0)^2}{2\sigma^2}}, \tag{4.37}$$

where the variance is given by $\sigma^2 = 1/\phi''(r_0)$. From equation (4.33) we see that the requirement for lasing $|\tilde{\Gamma}_{\perp}(r \to 0)| \gg \gamma$ implies the condition $\lambda_{\perp}^2 \Omega^2 \gg \gamma\Gamma^3$, for which the variance of the Gaussian distribution is essentially determined by thermal fluctuations, $\sigma^2 \approx N_{\text{th}}/4$. In this limit, the mean occupation number $n_f \approx r_0^2 + 3\sigma^2$ derived from equation (4.37) is approximately given by

$$n_f \approx \frac{\Omega}{2\lambda_{\perp}}\sqrt{\frac{\Gamma}{\gamma}} + \frac{3}{4}N_{\text{th}}. \tag{4.38}$$

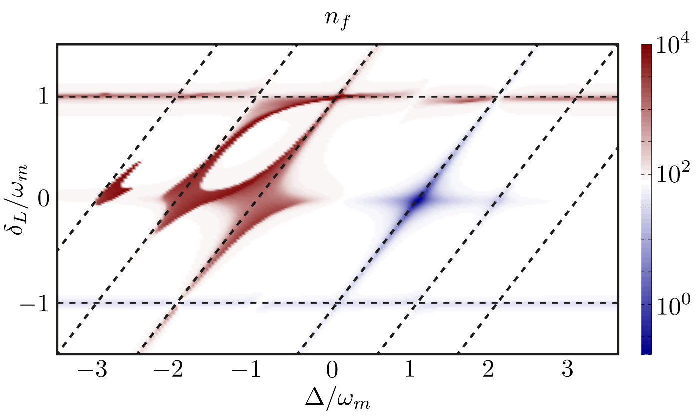

Figure 4.4 – Numerically evaluated final phonon occupation number n_f as function of Δ and δ_L and assuming an initial occupation of $N_{\text{th}} = 80$. The other parameters used for this plot are (in units of ω_m) $\Omega = 0.05$, $\Gamma = 0.05$, $\gamma = 10^{-6}$, $\lambda_\perp = \lambda_\parallel = 0.005$ and $\Gamma_\phi = 0$. The dashed lines indicate the resonance conditions for single and multi-phonon sidebands.

Our analytical results are compared to the numerically-computed final phonon occupation number in figure 4.3 b), and we find very good agreement above threshold.

4.4.3 Single- and multi-phonon regime

In general, the presence of both $\Sigma_\perp$- and $\Sigma_\parallel$-type NV-phonon interactions can lead to a rich interplay between cooling and heating mechanisms, as different single and multi-phonon processes become resonant depending on the laser detuning δ_L and the excited state splitting Δ. This is illustrated in figure 4.4, where we evaluate numerically the final phonon occupation number n_f for a large range of detunings δ_L and Δ. The plot shows the same cooling and heating processes discussed above, corresponding to $\Sigma_\perp$-type (maximized for $\Delta = \pm\omega_m$, $\delta_L = 0$) and $\Sigma_\parallel$-type (maximized for $\delta_L = \pm\omega_m$) interactions and associated with emission or absorption of single phonons. In addition, we observe heating and cooling features at multiple integers of the phonon frequency, i.e. under the condition $\delta_L - \Delta = \pm n\omega_m$, indicating multi-phonon processes. These effects are most pronounced in the lasing regime, where the mechanical mode is highly excited and higher order phonon-processes become relevant. Note that such multi-phonon effects (for example the two- and three-phonon lasing peaks at $\Delta = -2\omega_m$ and $\Delta = -3\omega_m$) appear only in the presence of *both* types of couplings. Similarly, two types of NV-phonon interactions are thought to be involved in the NV zero-phonon line broadening and its T^5 scaling [72]. In light of this, studying multi-phonon lasing may provide a useful tool to analyze the detailed nature of NV-phonon coupling.

4.5 DETECTION

In this last section we study the excitation spectrum of the NV center, which provides a direct way to probe the state of the mechanical resonator by measuring the light scattered from the NV center. By considering a polarization-selective photon detection setup, we calculate the photon flux $I_{\eta=x,y}(\delta_L) = \Gamma\langle\sigma_{\eta\eta}\rangle$ emitted from the two excited states and as a function of the laser detuning δ_L. According to the definition in equation (4.16) we obtain

$$I_\eta(\delta_L) = \Gamma \int d^2\alpha \, P_{\eta\eta}(\alpha), \tag{4.39}$$

and under the validity of our semiclassical approximation, $P_{\eta\eta}(\alpha) \simeq X^0_\eta(\alpha)P(\alpha,\infty)$. Here $X^0_\eta(\alpha)$ is an energy-dependent factor and $P(\alpha,\infty)$ is the stationary P-function as evaluated in the previous section.

In figure 4.5 a) we plot $I_y(\delta_L)$ for different driving strengths Ω and with only $\Sigma_\parallel$-type coupling. For clarity, we normalize each curve to $I_0 = \Gamma\Omega^2/(\Gamma^2+\Omega^2)$, which is the scattered photon flux at resonance and in the absence of the mechanical mode. At low driving powers, the influence of the NV center on the mechanical mode is small and the resonator mode remains in a thermal state, $\langle n\rangle \approx N_{\text{th}}$. In this case we obtain the familiar phonon sideband spectrum of a two level defect [91],

$$I_y(\delta_L) \approx \frac{\Gamma\,(\Omega/2)^2}{(\Gamma/2)^2+\delta_L^2} \sum_{n=-\infty}^{\infty} A_n e^{-\left(\lambda_\parallel/\omega_m\right)^2(2\langle n\rangle+1)}, \tag{4.40}$$

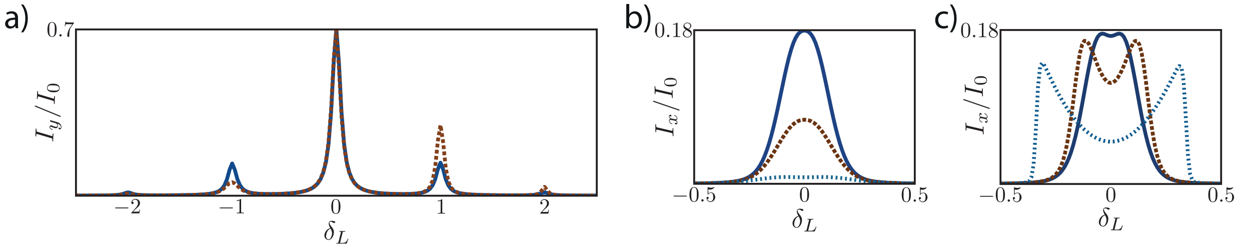

Figure 4.5 – Scattered photon flux $I_{\eta=x,y}$ as functions of the laser detuning δ_L and normalized to the resonant scattering rate I_0. a) Photon flux from the $|y\rangle$ state and assuming a dominant $\Sigma_{\|}$ coupling of strength $\lambda_{\|} = 0.05\omega_m$ and an equilibrium occupation number of $N_{th} = 80$. At low driving, $\Omega = 0.001\omega_m$ (solid line), phonon sideband at $\delta_L = \pm\omega_m$ are of approximately the same height. At larger probe strength, $\Omega = 0.01\omega_m$ (dashed line), the probe laser induces cooling and heating effects, which result in a pronounced asymmetry between the sidebands. The other parameters for this plot are (in units of ω_m) $\Gamma = 0.1$, $\Gamma_\phi = 0$, $\gamma = 10^{-6}$. In b) and c) the scattered photon flux from the $|x\rangle$ state is plotted for $\Delta = \omega_m$ and $\Delta = -\omega_m$, respectively. In b) the height of the scattered intensity peak provides a direct measurement of the phonon number $\langle n\rangle$. In c) the transition to the lasing regime at large Ω results in a phonon induced Rabi-splitting of the signal proportional to $\sim 2\lambda_\perp\sqrt{\langle n\rangle}$. For these two plots a $\Sigma_\perp$-type coupling with strength $\lambda_\perp = 0.01\omega_m$ has been assumed and $\Omega = 10^{-2.5}$ (solid lines), $\Omega = 10^{-2}$ (dashed lines) and $\Omega = 10^{-1.5}$ (dotted lines). The other parameters are as in a).

where $A_n = \mathcal{I}_n[2(\lambda_{\|}/\omega_m)^2\sqrt{\langle n\rangle(\langle n\rangle + 1)}] \times [(\langle n\rangle + 1)/\langle n\rangle]^{n/2}$ and $\mathcal{I}_n(x)$ is the nth order modified Bessel function. As we increase the driving strength we find deviations from this dependence: by probing the mechanical sidebands, we simultaneously generate significant cooling and heating, and the mean occupation $\langle n\rangle \equiv \langle n\rangle(\delta_L)$ varies as a function of the detuning. For example, for $\delta_L \approx -\omega_m$ the phonon modes is cooled, which leads to a reduction of the corresponding phonon peak. In the opposite case, i.e. $\delta_L \sim \omega_m$ the phonon sideband is amplified due to heating and lasing effects. The resulting asymmetry between red and the blue phonon sidebands, provides a clear signature for the backaction of the probing laser on the phonon modes.

In figure 4.5 b) and c) we plot the scattered light intensity $I_x(\delta_L)$ from the $|x\rangle$ level, still assuming that the NV center is excited on the $|g\rangle \rightarrow |y\rangle$ transition. In this case, there is no scattered light and $I_x(\delta_L) \approx 0$ in the absence of the mechanical mode, and therefore the measured signal is a direct consequence of phonon-induced transitions between $|y\rangle$ and $|x\rangle$. Figure 4.5 b) shows the signal for cooling conditions, $\Delta = \omega_m$. As above, we see that by probing the resonance with increasing driving strength, cooling sets in and reduces the height of the peak. For weak driving, $\Omega < \Gamma$ and $\lambda\sqrt{\langle n\rangle} \ll \Gamma$, the total photon flux is approximately given by

$$I_x(\delta_L) \approx \frac{4\lambda_\perp^2\Omega^2\Gamma}{(\Gamma^2 + 4\delta_L^2)^2} \times \langle a^\dagger a\rangle. \tag{4.41}$$

and it can be directly used to measure the final occupation number $\langle n\rangle$. Compared to the case of a two level system described above, where the phonon sidebands are reduced by $(\lambda_\parallel/\omega_m)^2$, the signal given in equation (4.41) remains significant even for large mechanical frequencies and provides a practical way to measure the temperature of high frequency phonon modes in experiments.

Finally, figure 4.5 c) shows the excitation spectrum $I_x(\delta_L)$ for heating conditions, $\Delta = -\omega_m$. In this case, the transition to a lasing state can substantially increase the phonon occupation number when probing the resonance with moderate laser power. Similar to cooling, the influence of phonon lasing on the excitation spectrum can also be used to determine the mean phonon number: here, it is no longer provided by the height of the resonance, but rather the splitting of the resonance into two peaks by $\sim 2\lambda_\perp\sqrt{\langle n\rangle}$. This splitting results from the mechanical system being driven into a large-amplitude oscillating state, which in turn acts like an additional strong driving field between the two excited NV states.

5

Phonon-reservoir engineering with SiV centers

In this chapter, we describe a new approach for mechanical cooling and dissipation engineering for the low-frequency vibrations of a mechanical beam, which uses the naturally occurring low-temperature bath provided by the high-frequency compression modes of the beam structure. We illustrate this scheme for the example of a SiV center in a vibrating nano-scale diamond beam. These schemes presented here are based on the defect-phonon interaction theory described in chapter 2. The development of these methods was done in collaboration with M.-A. Lemonde, A. Norambuena, J. R. Maze and P. Rabl and the theoretical results were published in Physical Review B [58]. For this work, I performed the calculations related to the cooling and two-mode squeezing while M.-A. Lemonde performed most of the analysis of the phonon spectral density presented in section 5.3.

5.1 Introduction

As previously discussed in the context of trapped ions, laser cooling can be viewed as a special case of the more general concept of *quantum reservoir engineering* [92], which refers to techniques for preparing a quantum system in a highly non-classical stationary state by an appropriately designed dissipation mechanism [93–95]. A basic example of such reservoir engineering concepts is the dissipative preparation of a squeezed motional state of a trapped ion via a two-tone driving [96, 97], but more elaborate schemes can be used to create, for example, highly nonclassical cat states [92, 98], stationary entangled states between separated systems [99–101], or even for the preparation of non-trivial many-body states [102–104]. Reservoir-engineering ideas have also been discussed and implemented for macroscopic mechanical objects [105–110], using again the optical or microwave radiation field as a low-entropy environment.

In this part, we describe an alternative approach for mechanical cooling and dissipation engineering for the low-frequency vibrations of a mechanical beam, which uses of the naturally occurring low-temperature bath provided by the high-frequency compression modes of the beam structure. Since intrinsic nonlinear interactions between mechanical modes are typically very weak, we propose here to mediate the coupling via a single electronic defect center embedded in the host lattice of the beam. Specifically, we illustrate this scheme for the example of a negatively charged silicon-vacancy (SiV^-) center in a vibrating diamond nanobeam, but the basic concept could be applicable for other defects and host materials as well. We analyze the application of this general scheme for the ground state cooling of the fundamental bending mode, as well as for the preparation of a stationary entangled state between two different mechanical resonator modes. These schemes rely solely on the intrinsic properties of the beam and do not require optical fields or strong optomechanical couplings to microwave circuits. Thus, such phononic reservoir engineering ideas could provide a valuable alternative for mechanical systems, where an efficient integration with optical or microwave photons is not available. In view of the recent progress in the fabrication of high-quality diamond structures and mechanical beams [17, 18, 31], and demonstrations of strain-induced control of defects [111–115], the proposed scheme could realistically be implemented in such systems.

5.2 MODEL

The setup that we shall consider in this chapter is depicted in figure 5.1 (a), which shows a singly-clamped diamond nanobeam with a single SiV^- center located near its freely vibrating end. In the presence of a strong magnetic field gradient, which is produced, for example, by a nearby magnetized tip, the bending motion of the beam modulates the local magnetic field and thereby

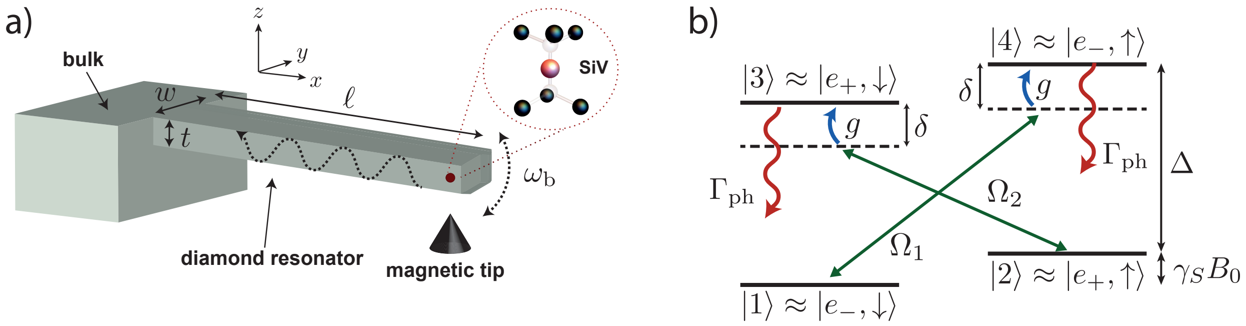
a)
z
y
x
bulk
w
t
ℓ
SiV
ω_b
diamond resonator
magnetic tip
b)
$|4\rangle \approx |e_-,\uparrow\rangle$
$|3\rangle \approx |e_+,\downarrow\rangle$
δ
g
δ
g
Γ_ph
Γ_ph
Δ
Ω_2
Ω_1
$|2\rangle \approx |e_+,\uparrow\rangle$
$\gamma_S B_0$
$|1\rangle \approx |e_-,\downarrow\rangle$

Figure 5.1 – a) Sketch of a single SiV$^-$ center embedded near the freely vibrating end of a diamond cantilever of length ℓ, width w and thickness t. In the presence of a strong magnetic field gradient produced by a nearby magnetized tip, the motion of the beam modulates the local magnetic field and results in a magnetic coupling between the electronic spin of the SiV$^-$ center and the fundamental bending mode with frequency ω_b. In addition, the orbital states of the defect are coupled via strain to a continuum of compression modes propagating along the beam (indicate by the curvy arrow). b) Level scheme of the SiV$^-$ ground state and the relevant microwave transitions used for ground state cooling of the bending mode.

couples to the electronic spin of the defect [116–118]. In addition, local lattice distortions associated with internal compression modes of the beam affect the defect's electronic structure and result in a strain coupling between these phonons and the orbital degrees of freedom of the center. The Hamiltonian for the whole system is given by

$$H = H_\mathrm{SiV} + H_\mathrm{ph} + H_\mathrm{mag} + H_\mathrm{strain}, \tag{5.1}$$

where the individual terms describe the bare SiV$^-$ center (discussed in section 2.2.2), the phonon modes of the diamond beam and the magnetic and strain-induced defect-phonon couplings, respectively. Under the validity of the different approximations outlined in the discussion of the SiV-phonon coupling in section 2.3.2 (see equation 2.73), we obtain the final Hamiltonian for the SiV$^-$ center and the vibrations of the beam,

$$H = H_\mathrm{SiV} + \omega_\mathrm{b} b^\dagger b + g_\mathrm{m}(b^\dagger + b)S_z + \sum_n \omega_n c_n^\dagger c_n + \sum_n \left(g_{s,n} c_n J_+ + g_{s,n}^* c_n^\dagger J_- \right), \tag{5.2}$$

which we will use as a starting point for the following analysis.

5.3 PHONON RESERVOIRS

In this part of the thesis, we are primarily interested in the steady state of the bending mode, which apart from the interaction with the SiV$^-$ center already included in equation (5.2), is also weakly coupled to the continuum of phonon modes in the cantilever support. This coupling is characterized by the damping rate γ_b and the thermal equilibrium occupation number N_b. For frequencies of $\omega_\mathrm{b} \sim$ MHz and temperatures $T \sim 1$ K, N_b is of the order of 10^4. In the absence of any other interaction, the bending mode will thus relax into a highly occupied thermal state. However, for realistic Q-values of $Q_\mathrm{b} \approx 10^5 - 10^6$, the thermalization with the phonon bath is very slow so that by engineering a more efficient coupling to an effective low-entropy reservoir, a cooling into a more pure quantum state can be achieved.

In our model, we consider only the electronic ground state of the SiV$^-$ center so that no radiative decay occurs, which is usually the main ingredient for atomic and mechanical laser cooling schemes. However, the orbital states are strongly coupled to the lattice vibrations at ~ 50 GHz. These modes dissipate very quickly and can thus serve as an efficient Markovian reservoir for the SiV states. The characteristic phonon-induced decay rate, Γ_ph, for the higher-energy orbital states $|3\rangle$ and $|4\rangle$ can be estimated from Fermi's Golden rule. At temperatures $T \to 0$, it is given by $\Gamma_\mathrm{ph} = J(\Delta)$, where

$$J(\omega) = 2\pi \sum_n |g_{\mathrm{s},n}|^2 \delta(\omega - \omega_n) \tag{5.3}$$

is the phonon spectral density. For temperatures $T > \hbar\Delta/k_B \approx 2.4$ K, the decay rate is enhanced by the thermal occupation number $N_\mathrm{c} = N_\mathrm{BE}(\Delta)$ and reverse transitions, e.g., from state $|1\rangle$ to state $|3\rangle$, become allowed. Experimental studies of SiV$^-$ centers in bulk at temperatures of few Kelvin observe a bare phonon induced decay rate of $\Gamma_\mathrm{ph}/2\pi \approx 1.6$ MHz [119].

5.3.1 MASTER EQUATION

Starting from the model given in equation (5.2), we can use a Born-Markov approximation to eliminate the fast dynamics of the compression modes and derive an effective master equation for the density operator ρ, which describes the SiV$^-$ degrees of freedom and the bending mode. We write the result as

$$\dot{\rho} = \left(\mathcal{L}_{\mathrm{b}} + \mathcal{L}_{\mathrm{SiV}} + \mathcal{L}_{\mathrm{int}}\right)\rho. \tag{5.4}$$

The first term describes the dynamics of the bending mode,

$$\dot{\rho} = -i\omega_{\mathrm{b}}[b^\dagger b, \rho] + \mathcal{L}_{\gamma_{\mathrm{b}}}\rho, \tag{5.5}$$

where $\mathcal{L}_{\gamma_{\mathrm{b}}}\rho$ is the standard thermal dissipator given in equation (3.5) and in this context describes the dissipation due to the coupling to the support of the cantilever. The second term in equation (5.4) represents the bare dynamics of the SiV$^-$ center including the phonon induced decay and excitation processes,

$$\mathcal{L}_{\mathrm{SiV}}\rho = -i[H_{\mathrm{SiV}}, \rho] + \frac{\Gamma_{\mathrm{ph}}}{2}(N_{\mathrm{c}} + 1)\mathcal{D}[J_-]\rho + \frac{\Gamma_{\mathrm{ph}}}{2}N_{\mathrm{c}}\mathcal{D}[J_+]\rho. \tag{5.6}$$

Finally, the last term,

$$\mathcal{L}_{\mathrm{int}}\rho = -i[g_{\mathrm{m}}(b + b^\dagger)S_z, \rho], \tag{5.7}$$

accounts for the magnetic spin-phonon interaction.

In view of $N_{\mathrm{c}} \ll N_{\mathrm{b}}$, it is our overall goal to use the driven SiV$^-$ center to mediate an effective coupling between the bending mode and the low-entropy reservoir of compression modes. The extent to which this is possible depends on various system parameters. A particularity of the current setting is that the bending mode of interest, as well as the phononic bath composed of the

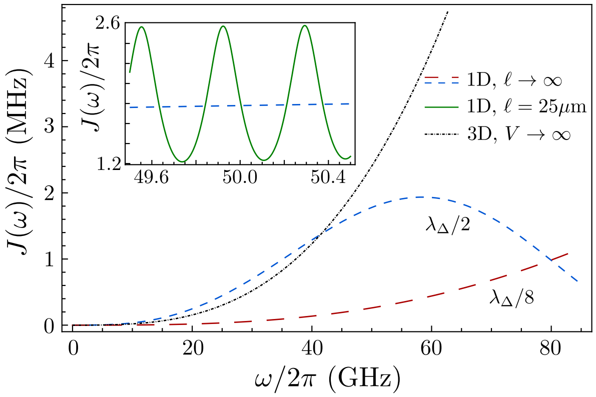

Figure 5.2 – Spectral density of the high frequency compression modes. The blue (short-) and red (long-) dashed lines represent the spectral density in the limit of a semi-infinite 1D-cantilever along x. The density of state of the phonons is linear in frequency while the sinusoidal envelope is due to the position-dependence of the strain field. The blue and red curves are obtained for a SiV$^-$ defect positioned at $x_{\mathrm{SiV}} = \lambda_\Delta/2$ and $x_{\mathrm{SiV}} = \lambda_\Delta/8$ of the free end, respectively. The black dotted line represents the opposite limit of an infinite 3D-crystal. In that case, transverse modes play an important role and the phonon density of state goes as ω^3. For a realistic cantilever, the 1D limit should be corrected toward the 3D-limit, due to contributions of transverse modes. In the inset, we show a finite size ($\ell = 25\mu$m) 1D-cantilever, where the frequencies of each mode can be resolved. The finite width of each peak is due to a finite lifetime modeling losses into the bulk of the support. We chose $w = t = 0.1\mu$m (1D limit), $Q_\Delta = 250$ and $g_1 = g_2 = 2\pi \times 1$ PHz.

continuum of the compression modes, are determined by the same beam structure. The coherent and incoherent processes described in equation (5.4) are thus not completely independent of each other.

5.3.2 Phonon spectral density

In general, an accurate evaluation of the relevant phonon density of states requires a full numerical calculation of the individual phonon modes of a specific beam structure. However, to obtain a basic estimate of the phonon-induced decay rate and its dependence on the systems parameters, we summarize here a few limiting cases, which have been derived in reference [58] to obtain approximate analytic expressions for $J(\omega)$. Furthermore, in the following analysis, we neglect the effect of the weak Poisson ratio in diamond [120].

As a reference, let us first consider the limit of an infinite 3D diamond crystal, which would correspond to the case where all beam dimensions are much larger than the characteristic phonon wavelength $\lambda_\Delta = \pi v/\Delta \approx 0.2\ \mu$m, where $v = \sqrt{E/\rho} \approx 1.8 \times 10^4$ m/s is the characteristic speed of sound in diamond. In the 3D limit, the phonon modes are plane waves propagating along all directions with three possible orthogonal orientations of the displacement (polarization): one parallel (longitudinal polarization) and two perpendicular (transverse polarizations) to the wave propagation. Consequently, for every propagation directions $\vec{q}$, there are three possible polarizations with the corresponding displacements

$$\begin{aligned}
\hat{\mathbf{u}}_l(\vec{r},t) &= \sum_{\vec{q}} \frac{1}{\sqrt{2\rho V \omega_{l,q}}} \vec{e}_q \left[\hat{c}^\dagger_{l,\vec{q}}(t) e^{-i\vec{q}\cdot\vec{r}} + \hat{c}_{l,\vec{q}}(t) e^{i\vec{q}\cdot\vec{r}} \right], \\
\hat{\mathbf{u}}_\theta(\vec{r},t) &= -\sum_{\vec{q}} \frac{1}{\sqrt{2\rho V \omega_{t,q}}} \vec{e}_\theta \left[\hat{c}^\dagger_{\theta,\vec{q}}(t) e^{-i\vec{q}\cdot\vec{r}} + \hat{c}_{\theta,\vec{q}}(t) e^{i\vec{q}\cdot\vec{r}} \right], \qquad (5.8) \\
\hat{\mathbf{u}}_\phi(\vec{r},t) &= \sum_{\vec{q}} \frac{1}{\sqrt{2\rho V \omega_{t,q}}} \vec{e}_\phi \left[\hat{c}^\dagger_{\phi,\vec{q}}(t) e^{-i\vec{q}\cdot\vec{r}} + \hat{c}_{\phi,\vec{q}}(t) e^{i\vec{q}\cdot\vec{r}} \right].
\end{aligned}$$

Here, l stands for the longitudinal mode, with a displacement along the unit vector $\vec{e}_q$, θ and ϕ denote the two transverse modes, with displacements along the unit vectors $\vec{e}_\theta$ and $\vec{e}_\phi$ respectively. The operators $\hat{c}_{i,\vec{q}}$ are bosonic lowering operator for the mode with wavevector $\vec{q}$ and polarization i, and V is the volume of the diamond structure. Neglecting the weak Poisson ratio of diamond, the mode frequencies are given by

$$\omega_{l,q} = v_l q \approx \sqrt{\frac{E}{\rho}} q, \qquad \omega_{t,q} = v_t q = \sqrt{\frac{E}{2\rho}} q, \qquad (5.9)$$

where v_l and v_t are sound velocities of the longitudinal and transverse modes, respectively.

It is straightforward to compute the strain fields $\hat{\gamma}_{ij} = (\partial \hat{u}_i/\partial x_j + \partial \hat{u}_j/\partial x_i)/2$ at the SiV$^-$ position for each of the phonon modes of equations (5.8) and substitute them in equation (2.73), leading to the strain interaction Hamiltonian $\hat{H}^{3D}_{\text{strain}} = \hat{H}^{l}_{\text{strain}} + \hat{H}^{\theta}_{\text{strain}} + \hat{H}^{\phi}_{\text{strain}}$. As an example, the contribution from the transverse modes $\hat{c}_{\theta,\vec{q}}$ reads

$$\begin{aligned} H^{\theta}_{\mathrm{strain}} &= \sum_{\vec{q}} i g_{1,\theta}(\vec{q}) \hat{J}_{+} \hat{c}_{\theta,\vec{q}} - g_{2,\theta}(\vec{q}) \hat{J}_{+} \hat{c}_{\theta,\vec{q}} + \mathrm{H.c.}, \\ g_{1,\theta}(\vec{q}) &= \frac{g_1}{v_t} \sqrt{\frac{\omega_{t,q}}{2\rho V}} \sin\theta \cos\theta (\sin^2\phi - \cos^2\phi), \\ g_{2,\theta}(\vec{q}) &= \frac{2g_2}{v_t} \sqrt{\frac{\omega_{t,q}}{2\rho V}} \sin\theta \cos\theta \sin\phi \cos\phi. \end{aligned} \tag{5.10}$$

The spectral density, $J^{3D}(\omega) = J^{l}(\omega) + J^{\theta}(\omega) + J^{\phi}(\omega)$, is obtained by substituting the different coupling constants $g(\vec{q})$ in equation (5.3),

$$J^{\theta}(\omega) = \sum_{\vec{q}} \left[|g_{1,\theta}(\vec{q})|^2 + |g_{2,\theta}(\vec{q})|^2 \right] \delta(\omega - \omega_{t,q}), \tag{5.11}$$

leading to the infinite 3D limit

$$J^{3D}(\omega) = \frac{g_1^2 + g_2^2}{\pi\rho} \left(\frac{1}{5v_t^5} + \frac{2}{15v_l^5} \right) \omega^3. \tag{5.12}$$

For identical coupling constants $g_1 = g_2 \equiv g_{\mathrm{s}}$ [cf. equation (2.71)] and $\sqrt{2}v_t = v_l = v$, the spectral density reads

$$J_{3\mathrm{D}}(\omega) = C \frac{\hbar g_{\mathrm{s}}^2}{\pi\rho v^5} \omega^3, \tag{5.13}$$

with a numerical constant $C \approx 2.5$. By using the value $g_{\mathrm{s}}/2\pi \approx 1$ PHz, we obtain $\Gamma_{\mathrm{ph}}/2\pi \approx 1.78$ MHz, which is in good agreement with the experimental results found in reference [81, 119].

The other limiting case, which is more appropriate for the considered transverse beam dimensions of $t, w \lesssim \lambda_{\Delta}$, is the limit of a quasi-1D beam, where the frequencies of all the transverse compression modes exceed Δ. The remaining compression modes along the beam direction x adopt the simple form $\vec{u}_n(\vec{r}) \propto \vec{e}_x \cos(\omega_n x/v)$, with $\omega_n = \pi v n/\ell$. In that case, the strain-induced coupling constant introduced in equation (2.73) is

$$g_{\mathrm{s},n} = \frac{g_{\mathrm{s}}}{v}\sqrt{\frac{\hbar\omega_n}{\rho V}}\sin\left(\frac{\omega_n}{v}x_{\mathrm{SiV}}\right), \tag{5.14}$$

where x_{SiV} is the position of the defect along the cantilever.

For a completely isolated beam, the longitudinal compression modes are equally spaced with mode spacing $\delta\omega = \pi v/\ell$; for a $\ell = 25\,\mu$m long beam, $\delta\omega/2\pi \approx 370$ MHz. However, it is expected that the reflection of a compression mode at the clamping boundary is rather poor and in a realistic system, the individual resonances ω_n will be broadened by the decay γ_n into the phonon modes of the support or by other dissipation channels. The resulting finite phonon lifetime can be captured by approximating the phonon spectral function as a sum of individual (zero dimensional) Lorentzian peaks

$$J_{\mathrm{0D}}(\omega) \simeq \sum_n \frac{|g_{\mathrm{s},n}|^2}{4}\frac{\gamma_n}{(\omega-\omega_n)^2+\gamma_n^2/4}, \tag{5.15}$$

with $g_{\mathrm{s},n}$ given in equation (5.14).

In the limit $\delta\omega \lesssim \gamma_\Delta$, where $\gamma_\Delta = \Delta/Q_\Delta$ is the decay rate of the compression mode with frequency Δ, the resonances of interest completely overlap and the beam can be approximated by a semi-infinite 1D beam. This limit corresponds to values of the quality factor $Q_\Delta \lesssim 100$ for $\ell = 25\mu$m. The phonon spectral density then becomes

$$J_{\mathrm{1D}}(\omega) = \frac{g_{\mathrm{s}}^2}{2v^3}\frac{\hbar\omega}{\rho w t}\sin^2\left(\frac{\omega}{v}x_{\mathrm{SiV}}\right). \tag{5.16}$$

We see that compared to the 3D limit, the resulting phonon induced decay rate, $\Gamma_{\mathrm{ph}} = J(\Delta)$, strongly depends on the position of the SiV$^-$ defect. This is illustrated in figure 5.2, where we compare the semi-infinite 1D limit for two different positions of the SiV$^-$ defect. It clearly shows the possibility to engineer smaller (larger) phonon induced decay rates by placing the SiV$^-$ close to a node (anti node) of the strain field generated by the phonon mode of frequency Δ. Compared to the 3D case, the phonon induced decay in the 1D limit scales as

$$\frac{\Gamma_{\rm ph}^{(1{\rm D})}}{\Gamma_{\rm ph}^{(3{\rm D})}} \sim \frac{1}{2\pi C}\left(\frac{\lambda_\Delta^2}{A}\right)\sin^2\left(\pi\frac{x_{\rm SiV}}{\lambda_\Delta}\right), \tag{5.17}$$

where $A = wt$ is the cross section of the beam. A crossover between the 1D and the 3D limit is expected for $w \sim t \sim \lambda_\Delta$, i.e. when the first transverse compression mode of frequency Δ appears.

In a system where high mechanical quality factors even in the 50 GHz regime can be achieved, i.e., $Q_\Delta \gtrsim \Delta/\delta\omega$, the individual compression modes become spectrally resolved and equation (5.15) applies. In this limit, the phonon spectral density can be significantly enhanced or reduced by tuning the splitting Δ in resonance or off-resonance with a compression mode. Using this tunability, the phonon induced decay could be further varied over the range

$$\frac{4}{\pi}\left(\frac{\Delta}{\delta\omega Q_\Delta}\right) < \frac{\Gamma_{\rm ph}^{(0{\rm D})}}{\Gamma_{\rm ph}^{(1{\rm D})}} < \frac{2}{\pi}\left(\frac{\delta\omega Q_\Delta}{\Delta}\right). \tag{5.18}$$

The dependence of $J(\omega)$ is plotted in figure 5.2 in the different limiting regimes. For the reservoir-engineering schemes discussed below, we are interested in the so-called sideband-resolved regime $\Gamma_{\rm ph} \lesssim \omega_{\rm b}$. This can be achieved in general for small beams $\ell \sim 10\,\mu$m, where $\omega_{\rm b} \approx 3$ MHz. In cases where the 1D limit is reached, one can further make use of the SiV$^-$ positioning and frequency tuning to reach the well-resolved sideband regime.

5.4 Cooling

As a first application, we now analyze a cooling scheme —in accordance with the cooling theory described in chapter 3— for the low frequency bending mode. The basic idea is illustrated in figure 5.1 (b). At low temperatures, the SiV$^-$ center is predominantly in one of the lower states $|1\rangle$

or $|2\rangle$, but coupled to the excited states $|3\rangle$ or $|4\rangle$ by two microwaves fields detuned by the same amount $\delta = \omega_1 - (\Delta + \gamma_S B_0) = \omega_2 - (\Delta - \gamma_S B_0)$. In the presence of the magnetic field gradient, vibrations of the beam lead to phonon-induced processes, where the excitation of the internal state is accompanied by the absorption or emission of a motional quanta of frequency $\omega_{\rm b}$. The energy of the states $|3\rangle$ or $|4\rangle$ is then dissipated into the high frequency phonon reservoir at a rate $\Gamma_{\rm ph}$ and the cycle repeats. If the microwave fields are detuned to the red, i.e. $\delta < 0$, the phonon-absorption process dominates and the mechanical mode is cooled.

5.4.1 Reservoir engineering

It is instructive to also look at this cooling scheme from a more general perspective by first considering the magnetic coupling [equation (2.66)] in the interaction picture with respect to the free oscillator and the SiV$^-$ Hamiltonian,

$$\hat{H}_{\rm m}(t) = \left(\hat{b}e^{-i\omega_{\rm b}t} + \hat{b}^\dagger e^{i\omega_{\rm b}t}\right)\hat{F}(t). \tag{5.19}$$

The operator $\hat{F}(t) = g_{\rm m}\hat{S}_z(t)$ represents a force acting on the oscillator. If we assume that the dynamics of the SiV$^-$ center is only weakly perturbed by the resonator, i.e., $g_{\rm m}\sqrt{\langle b^\dagger b\rangle + 1} < \Gamma_{\rm ph}$ (a more detailed analysis shows that the weaker condition, $g_{\rm m}\sqrt{\bar{n}_{\rm b} + 1} < \Gamma_{\rm ph}$, is sufficient to correctly predict the final occupation number $\bar{n}_{\rm b}$ [82]), the fluctuations $\delta\hat{F}(t) = \hat{F}(t) - \langle\hat{F}(t)\rangle_0$ of this force are fully characterized by the spectrum

$$S_{\rm FF}(\omega) = 2{\rm Re}\int_0^\infty dt\,\langle\delta\hat{F}(t)\delta\hat{F}(0)\rangle_0 e^{i\omega t}. \tag{5.20}$$

Here, $\langle\ldots\rangle_0$ denotes the expectation value with respect to the stationary state of the SiV$^-$ center in absence of the magnetic coupling. From equation (5.19), we can deduce that the rates at which phonons are absorbed and emitted by the SiV$^-$ defect are proportional to the force spec-

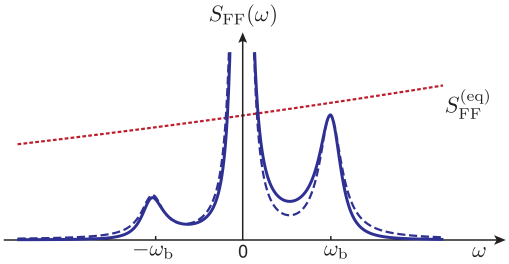

Figure 5.3 – The force fluctuation spectrum $S_{\mathrm{FF}}(\omega)$ defined in Eq. (5.20) is plotted for an SiV$^-$ center driven on the red sideband, $\delta = -\omega_{\mathrm{b}}$, and for $N_{\mathrm{c}} = 0.5$ and $\Gamma_{\mathrm{ph}}/\omega_{\mathrm{b}} = 0.15$. The dashed line corresponds to the approximate analytic result given in Eq. (5.24). For comparison, the red dotted line illustrates the fluctuation spectrum $S_{\mathrm{FF}}^{\mathrm{eq}}(\omega) \sim \omega\,[\coth(\hbar\omega/(2k_BT)) + 1]$ for an ohmic environment in equilibrium with a temperature $k_BT/(\hbar\omega_{\mathrm{b}}) = 5$.

trum evaluated at $+\omega_{\mathrm{b}}$ and $-\omega_{\mathrm{b}}$, respectively. For systems in thermal equilibrium, the ratio $S_{\mathrm{FF}}(-\omega)/S_{\mathrm{FF}}(\omega) = \exp(-\hbar\omega/k_BT)$ is fixed by the temperature T. However, in the present case of a driven SiV$^-$ center, the system is out of thermal equilibrium and the above detailed balance equation does not hold. The ratio $S_{\mathrm{FF}}(-\omega_{\mathrm{b}})/S_{\mathrm{FF}}(\omega_{\mathrm{b}})$ is instead used to define an effective temperature T_{eff} of the defect. If the asymmetry of $S_{\mathrm{FF}}(\pm\omega_{\mathrm{b}})$ is sufficiently high, this effective temperature becomes significantly lower than the temperature of the environment, allowing the defect to act as a cold reservoir for excitations of frequency ω_{b}. This is illustrated in figure 5.3, where $S_{\mathrm{FF}}(\omega)$ is plotted for a SiV$^-$ center driven on the red sideband ($\delta = -\omega_{\mathrm{b}}$) and compared to the equilibrium spectral density of an ohmic bath.

The above arguments can be derived more rigorously from an adiabatic elimination of the SiV$^-$ degrees of freedom —as described in chapter 3, section 3.1.2— and obtain an effective master equation for the reduced density operator of the bending mode, of the form

$$\dot{\hat{\rho}}_{\mathrm{b}} = (\mathcal{L}_{\mathrm{th}} + \mathcal{L}_{\mathrm{eff}})\,\hat{\rho}_{\mathrm{b}}, \tag{5.21}$$

where the second term describes the effect of the engineered effective reservoir (similar to the one derived in the case of the NV center, given in equation 4.6)

$$\mathcal{L}_{\text{eff}}\hat{\rho} = \frac{\Gamma_{\text{eff}}}{2}(N_{\text{eff}}+1)\mathcal{D}[\hat{b}]\hat{\rho} + \frac{\Gamma_{\text{eff}}}{2}N_{\text{eff}}\mathcal{D}[\hat{b}^{\dagger}]\hat{\rho}, \tag{5.22}$$

where $\Gamma_{\text{eff}} = S_{\text{FF}}(\omega_{\text{b}}) - S_{\text{FF}}(-\omega_{\text{b}})$ and $N_{\text{eff}} = S_{\text{FF}}(-\omega_{\text{b}})/\Gamma_{\text{eff}}$. From equation (5.21) we can derive the steady-state occupation number of the fundamental bending mode and obtain a form similar to equation (3.26)

$$\bar{n}_{\text{b}} = \frac{\gamma_{\text{b}}N_{\text{b}} + N_{\text{eff}}\Gamma_{\text{eff}}}{\gamma_{\text{b}} + \Gamma_{\text{eff}}} \simeq \frac{\gamma_{\text{b}}N_{\text{b}}}{\Gamma_{\text{eff}}} + N_{\text{eff}}, \tag{5.23}$$

where $\gamma_{\text{b}}N_{\text{b}} \simeq k_B T/(\hbar Q_{\text{b}})$ is the rate at which the mechanical system in the ground state would absorb a single phonon from the environment. The last equality is valid in the limit $\Gamma_{\text{eff}} \gg \gamma_{\text{b}}$.

5.4.2 Ground state cooling

The force spectrum $S_{\text{FF}}(\omega)$ can be evaluated numerically for all parameters using the quantum regression theorem. To obtain more insights, we restrict the following discussion to a fully symmetric situation $\Omega_1 = \Omega_2 = \Omega$ under weak driving conditions $\Omega \ll |\Gamma_{\text{ph}} + i\delta|$. In this limit, the spectrum is approximately given by

$$\begin{aligned} S_{\text{FF}}(\omega) = \epsilon g_{\text{m}}^2 \Gamma_{\text{ph}} \Bigg\{ & \frac{N_{\text{c}}+1}{(\delta+\omega)^2 + [(2N_{\text{c}}+1)\Gamma_{\text{ph}}/2]^2} \\ & + \frac{N_{\text{c}}}{(\delta-\omega)^2 + [(2N_{\text{c}}+1)\Gamma_{\text{ph}}/2]^2} + \frac{2N_{\text{c}}+1}{\omega^2 + [\epsilon(2N_{\text{c}}+1)\Gamma_{\text{ph}}/2]^2} \Bigg\}, \end{aligned} \tag{5.24}$$

where we have defined the probability to excite the higher-energy states via the drives

$$\epsilon = \frac{\Omega^2/4}{\delta^2 + [(1+2N_{\text{c}})\Gamma_{\text{ph}}/2]^2}. \tag{5.25}$$

An example of the spectrum is illustrated in figure 5.3 and exhibits three peaks at frequencies $\omega = 0, \pm\delta$. For red-detuned driving fields, the first term in equation (5.24) corresponds to the process where an excitation of the bending motion is absorbed, while the second term corresponds to the Stokes process where a phonon is emitted. Note that for a reservoir at finite temperature, the ratio between the heating and the cooling process scales as $N_\mathrm{c}/(N_\mathrm{c}+1)$. The peak at $\omega = 0$ arises from random spin-flip processes which are induced by the driving fields even in the absence of the phonon mode. These random spin flips occur at a rate $\Gamma_\mathrm{sf} \simeq \epsilon(2N_\mathrm{c}+1)\Gamma_\mathrm{ph}$ and create a fluctuating force symmetric in frequency. Therefore, they only contribute to N_eff and not to the cooling rate Γ_eff.

From this expression and in view of equation (5.23), we identify three basic conditions for achieving ground state cooling, i.e. $\bar{n}_\mathrm{b} < 1$. First, the system must be in the well-resolved sideband regime (i) $\Gamma_\mathrm{ph}(2N_\mathrm{c}+1) \lesssim \omega_\mathrm{b}$. Provided that $S_\mathrm{FF}(\omega)$ [cf. equation (5.24)] is a sum of three Lorentzian peaks centered at $\omega = 0$ and $\omega = \pm\delta$ with width $\sim \Gamma_\mathrm{ph}(2N_\mathrm{c}+1)$, this condition is necessary to have a large asymmetry between the positive-frequency and negative-frequency domain of the force spectrum in the ideal case $\delta = -\omega_\mathrm{b}$. As a consequence, Γ_eff is enhanced while the minimal occupancy N_eff is decreased. If this condition is satisfied, the remaining asymmetry is determined by N_c, which sets the limit $\bar{n}_\mathrm{b} \geq N_\mathrm{c}$. In terms of the effective temperature, this limit means that the cooling ratio can reach

$$\frac{T_\mathrm{eff}}{T} = \frac{\omega_\mathrm{b}}{\Delta} \approx 10^{-5} - 10^{-4}. \tag{5.26}$$

The high-frequency phonon reservoir must then also be close to the ground state, i.e. (ii) $N_\mathrm{c} < 1$. Finally, the engineered cooling rate,

$$\Gamma_\mathrm{eff} = \epsilon g_\mathrm{m}^2 \Gamma_\mathrm{ph} \left\{ \frac{1}{(\delta+\omega_\mathrm{b})^2 + [(1+2N_\mathrm{c})\Gamma_\mathrm{ph}/2]^2} - \frac{1}{(\delta-\omega_\mathrm{b})^2 + [(1+2N_\mathrm{c})\Gamma_\mathrm{ph}/2]^2} \right\}, \tag{5.27}$$

must overcome the rethermalization rate of the natural bath (iii) $\Gamma_\mathrm{eff} > \gamma_\mathrm{b} N_\mathrm{b}$. For a phononic bath in its ground state ($N_\mathrm{c} < 1$) coupled to a SiV$^-$ center driven on a very well-resolved red sideband ($\delta = -\omega_\mathrm{b}$, $\Gamma_\mathrm{ph} \ll \omega_\mathrm{b}$), the effective damping rate is maximized to $\Gamma_\mathrm{eff} = g_\mathrm{m}^2 \Omega^2/(\Gamma_\mathrm{ph}\omega_\mathrm{b}^2)$. Note that this result is derived under the assumption of weak coupling and the cooling rate is always bounded by $\Gamma_\mathrm{eff} \lesssim g_\mathrm{m}$.

While condition (ii) is solely determined by the temperature of the support, the competition between the coupling strength $g_\mathrm{m} \propto \sqrt{\ell}$ and the mechanical frequency $\omega_\mathrm{b} \propto 1/\ell^2$ may prevent one from fulfilling (i) and (iii) at the same time. This is illustrated in figure 5.4, where we show the final occupancy of the fundamental bending mode $\bar{n}_\mathrm{b}$ [cf. equation (5.23)] as a function of the beam length ℓ for different values of Γ_ph and T. We see that already for temperatures $T \lesssim 1$ K and a moderate suppression of the phonon spectral density below the 3D limit, ground state cooling becomes feasible.

Let us finally remark that in our analysis we have neglected coherent frequencies shifts as well as coherent couplings to other vibrational modes that are induced by the driven SiV$^-$ center. Such coherent interaction induced by the effective reservoir are at most as large as $\Gamma_\mathrm{eff} \ll \omega_\mathrm{m}$ and therefore under usual conditions will only lead to minor correction in the above described dynamics. However, for a highly symmetric resonator the SiV$^-$ center could potentially also be used to induce a switchable coupling between two nearly degenerate modes.

5.5 TWO-MODE SQUEEZING

As a second application of the scheme described in this chapter, we now discuss an extension of the previous scheme for the dissipative preparation of an entangled two-mode squeezed (TMS) state $|\psi_\mathrm{TMS}\rangle$, which is shared between two low-frequency mechanical modes $\hat{a}$ and $\hat{b}$. A pure TMS state

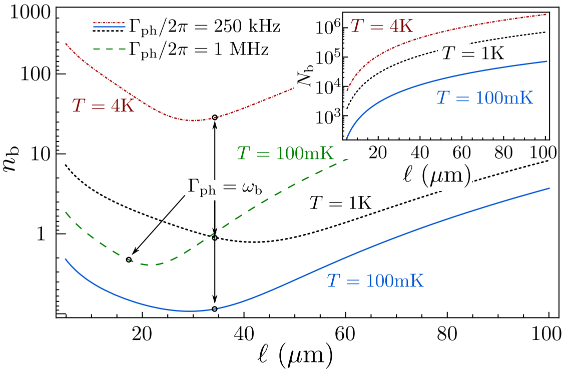

Figure 5.4 – Final occupation of the bending mode $\bar{n}_{\mathrm{b}}$ as function of the beam length ℓ for different values of Γ_{ph}. We considered a diamond cantilever at $T = 4$K (dotted-dashed red line), which corresponds to an occupation of the compression mode of frequency $\Delta/2\pi = 50$ GHz of $N_{\mathrm{c}} \approx 1.2$. The blue solid line shows the results for $\Gamma_{\mathrm{ph}}/2\pi = 250$ kHz and a lower temperature $T = 100$mK ($N_{\mathrm{c}} \simeq 0$) while the dotted black line corresponds to an intermediate temperature of $T = 1$K ($N_{\mathrm{c}} \simeq 0.1$). In the inset, we plot the initial occupation ($g_{\mathrm{m}} = 0$) of the bending mode. It shows that even for initial occupancy $N_{\mathrm{b}} \sim 10^4$, it is possible to reach the ground state ($\bar{n}_{\mathrm{b}} < 1$) using experimentally accessible parameters. These results are obtained using a driving strength $\epsilon = 0.2$ [cf. equation (5.27)] and the full expression of $S_{\mathrm{FF}}(\omega)$ that includes the drive at every order; we use the corresponding optimal detuning $\delta \approx -\omega_{\mathrm{b}}/\sqrt{1+4\epsilon}$. The remaining parameters are the bending mode quality factor $Q_{\mathrm{b}} = 10^6$, the transverse beam dimension $w = t = 0.1$ μm and a magnetic field gradient of 10^7 T/m.

is defined by the conditions

$$\begin{aligned}\hat{A}|\psi_{\mathrm{TMS}}\rangle &= (\mu\hat{a}+\nu\hat{b}^\dagger)|\psi_{\mathrm{TMS}}\rangle = 0,\\ \hat{B}|\psi_{\mathrm{TMS}}\rangle &= (\mu\hat{b}+\nu\hat{a}^\dagger)|\psi_{\mathrm{TMS}}\rangle = 0,\end{aligned} \tag{5.28}$$

where μ and ν are complex parameters satisfying $|\mu|^2-|\nu|^2=1$. This implies that these parameters can be written as $\mu=\cosh(r)$ and $\nu=e^{i\theta}\sinh(r)$, where r is the squeezing parameter. The TMS state belongs to the family of Gaussian states for which entanglement can be verified from a violation of the separability criteria [121, 122]

$$\xi = \frac{1}{2}\left[\mathrm{Var}(\hat{x}_a+\hat{x}_b)+\mathrm{Var}(\hat{p}_a-\hat{p}_b)\right] \geq 1, \tag{5.29}$$

where $\hat{x}_a = (\hat{a}^\dagger+\hat{a})/\sqrt{2}$ and $\hat{p}_a = i(\hat{a}^\dagger-\hat{a})/\sqrt{2}$ are the normalized position and momentum operators ($a\to b$ for the $\hat{b}$ mode). For a pure TMS state and $\theta=0$, the amount of entanglement increases exponentially with the squeezing parameter, i.e. $\xi=e^{-2r}$.

For mechanical oscillators prepared in a pure TMS state, the thermal noise coming from their coupling to the environment rapidly degrades such a fragile entangled state. It is thus intriguing to consider engineered processes, where the TMS state emerges as a steady state of a purely dissipative dynamics. From the dark state conditions (5.28), one can readily see that $|\psi_{\mathrm{TMS}}\rangle$ is the stationary state of a master equation of the form

$$\mathcal{L}_{\mathrm{sq}}\hat{\rho} = \frac{\Gamma_{\mathrm{sq}}}{2}\left(2\hat{A}\hat{\rho}\hat{A}^\dagger-\hat{A}^\dagger\hat{A}\hat{\rho}-\hat{\rho}\hat{A}^\dagger\hat{A}\right)+\frac{\Gamma_{\mathrm{sq}}}{2}\left(2\hat{B}\hat{\rho}\hat{B}^\dagger-\hat{B}^\dagger\hat{B}\hat{\rho}-\hat{\rho}\hat{B}^\dagger\hat{B}\right). \tag{5.30}$$

The implementation of such a dissipation process has previously been discussed and experimentally implemented in the context of two separated spin ensembles coupled to a common optical channel [100, 101] and closely related schemes have been proposed for optomechanical sys-

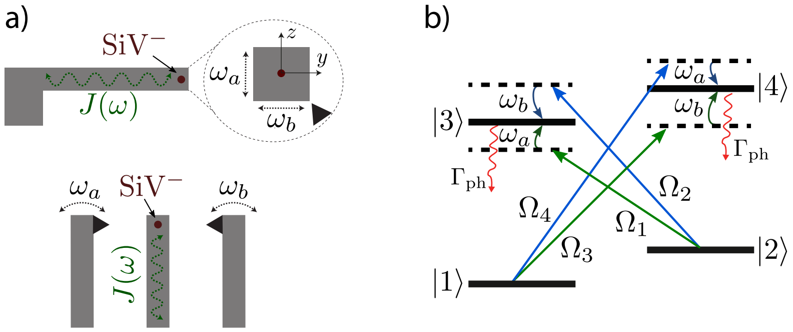
a)
SiV^-
ω_a
z
y
$J(\omega)$
ω_b
ω_a
SiV^-
ω_b
$J(\omega)$
b)
$|3\rangle$
ω_b
ω_a
Γ_{ph}
ω_a
$|4\rangle$
ω_b
Γ_{ph}
Ω_4
Ω_2
Ω_1
Ω_3
$|1\rangle$
$|2\rangle$

Figure 5.5 – Setup for the dissipative preparation of a mechanical two-mode squeezed state. a) Two possible configurations, where two vibrational modes, representing either orthogonal vibration modes of the same beam (left) or the fundamental bending modes of two different beams (right), are coupled magnetically to the same SiV^- center. b) Energy level diagram of the SiV^- defect. The green and blue arrows indicate the four driving fields which are detuned from resonance by $\pm\omega_a$ and $\pm\omega_b$. See text for more details.

tems [108, 109, 123]. In the following, we show how such an effective dissipation can be realized in the present setup and evaluate its robustness with respect to finite temperature effects and deviations from the ideal side-band resolved limit.

5.5.1 DRIVING SCHEME

We consider two low-frequency mechanical modes $\hat{a}$ and $\hat{b}$ with two different frequencies ω_a and ω_b, respectively. As shown in figure 5.5 (a), these two modes could be two bending modes of the same beam, or the fundamental modes of two independent beams coupled magnetically to the same SiV^- center. In contrast to the cooling scheme, engineering the jump operators $\hat{A}$ and $\hat{B}$ requires driving the transitions $|1\rangle \rightarrow |4\rangle$ and $|2\rangle \rightarrow |3\rangle$ by two near-resonant microwave fields. As indicated in figure 5.5 (b), those drives are detuned by $-\omega_a$ and $+\omega_b$ in one half of the cycle (e.g. transitions $2 \rightarrow 3$) where a phonon is added to the mode a and removed from the mode b, and by $+\omega_a$ and $-\omega_b$ in the other half (e.g. transitions $1 \rightarrow 4$) where the opposite processes take place.

The total Hamiltonian for this system is then given by

$$\hat{H}_{\mathrm{sq}} = \hat{H}_{\mathrm{res}} + \hat{H}_{\mathrm{SiV}} + \hat{H}_{\mathrm{m}}, \tag{5.31}$$

where $\hat{H}_{\mathrm{res}} = \omega_a \hat{a}^\dagger \hat{a} + \omega_b \hat{b}^\dagger \hat{b}$ is the Hamiltonian of the two mechanical resonator modes and

$$\begin{aligned} \hat{H}_{\mathrm{SiV}} = \sum_{j=1,4} E_j |j\rangle\langle j| &+ \left(\frac{\Omega_1}{2} e^{-i\omega_1 t} - \frac{\Omega_2}{2} e^{-i\omega_2 t} \right) |3\rangle\langle 2| + \mathrm{H.c.} \\ &- \left(\frac{\Omega_3}{2} e^{-i\omega_3 t} - \frac{\Omega_4}{2} e^{-i\omega_4 t} \right) |4\rangle\langle 1| + \mathrm{H.c.} \end{aligned} \tag{5.32}$$

is the Hamiltonian for the internal states, where $E_1 = 0$, $E_2 = \gamma_S B_0$, $E_3 = \Delta$ and $E_4 = \Delta + \gamma_S B_0$. Note that in equation (5.32) all Rabi frequencies Ω_i are assumed to be real and positive and the minus signs have been chosen to reproduce the correct effective interaction in the analysis below. Finally,

$$\hat{H}_{\mathrm{m}} = \left[g_a(\hat{a} + \hat{a}^\dagger) + g_b(\hat{b} + \hat{b}^\dagger) \right] \hat{S}_z \tag{5.33}$$

is the Zeeman coupling as introduced in equation (2.66).

5.5.2 SIDEBAND-RESOLVED REGIME

For the implementation of the TMS state master equation (5.30), it is instructive to first follow a simplified approach that is valid in the well-resolved sideband regime. In this regime, only the resonant processes play an important role and, as we show, are responsible for the mechanical entanglement. In order to identify those dominant processes, we first perform a polaron transformation $\hat{H} \to \hat{U} \hat{H} \hat{U}^\dagger$ [8], where

$$\hat{U} = \exp \left\{ \sum_{\eta=a,b} \frac{g_\eta}{\omega_\eta} (\hat{\eta}^\dagger - \hat{\eta}) \hat{S}_z \right\}. \tag{5.34}$$

This transformation eliminates the coupling $\hat{H}_{\rm m}$, but generates an infinite series of phonon sidebands in the driving processes, i.e.

$$\begin{aligned} |3\rangle\langle 2| &\rightarrow |3\rangle\langle 2| e^{-\sum_{\eta=a,b}\frac{g_\eta}{\omega_\eta}(\hat{\eta}^\dagger-\hat{\eta})}, \\ |4\rangle\langle 1| &\rightarrow |4\rangle\langle 1| e^{\sum_{\eta=a,b}\frac{g_\eta}{\omega_\eta}(\hat{\eta}^\dagger-\hat{\eta})}. \end{aligned} \tag{5.35}$$

For $g_\eta/\omega_\eta \ll 1$, we can expand the exponential to first order and thus neglect the contribution of higher-order phonon processes. By going into the interaction picture with respect to $\hat{H}_{\rm res} + \hat{H}_{\rm SiV}$ and making a RWA, only the resonant processes remain so that $\hat{H}_{\rm sq}$ adopts the form

$$\hat{H}_{\rm sq} \simeq \frac{\tilde{g}}{2}(\hat{A}|3\rangle\langle 2| + \hat{B}|4\rangle\langle 1|) + {\rm H.c.} \tag{5.36}$$

In the particular case of a symmetric driving cycle (cf. figure 5.5), where the cooling (heating) processes for both mechanical modes occur at the same rates, i.e. $\Omega_1 g_a/\omega_a = \Omega_3 g_b/\omega_b$ ($\Omega_2 g_b/\omega_b = \Omega_4 g_a/\omega_a$), the new jump operators $\hat{A}$ and $\hat{B}$ are defined as in equation (5.28) with

$$\tilde{g}\mu = \frac{\Omega_1 g_a}{\omega_a} = \frac{\Omega_3 g_b}{\omega_b}, \qquad \tilde{g}\nu = \frac{\Omega_4 g_a}{\omega_a} = \frac{\Omega_2 g_b}{\omega_b}. \tag{5.37}$$

The condition $|\mu|^2 - |\nu|^2 = 1$, which imposes the proper commutation relations for $\hat{A}$ and $\hat{B}$, is fulfilled when the coupling constant $\tilde{g}$, given by

$$\tilde{g} = \frac{g_a}{\omega_a}\sqrt{\Omega_1^2 - \Omega_4^2} = \frac{g_b}{\omega_b}\sqrt{\Omega_3^2 - \Omega_2^2}, \tag{5.38}$$

remains real. One can show that for drive strengths that lead to an imaginary coupling constant $\tilde{g}$, the coherent dynamics described by $\hat{H}_{\rm sq}$ becomes unstable. Physically, it corresponds to heating processes ($\sim \Omega_2, \Omega_4$) that exceed the rates at which the drives cool down the mechanical modes

($\sim \Omega_1, \Omega_3$), leading to a parametric instability of the mechanical system. The squeezing parameter is also determined by the ratio between the driving strengths for the two mechanical modes:

$$\tanh(r) = \frac{\Omega_2}{\Omega_3} = \frac{\Omega_4}{\Omega_1}. \tag{5.39}$$

As expected, the squeezing parameter diverges when the heating and cooling rates become equal.

As a final step, we can adiabatically eliminate the internal degrees of freedom of the SiV$^-$, given that $\Gamma_{\mathrm{ph}} \gg g_a, g_b$, and obtain the master equation

$$\dot{\hat{\rho}} = \left(\mathcal{L}_{\mathrm{th}} + \mathcal{L}_{\mathrm{sq}}\right)\hat{\rho}. \tag{5.40}$$

The first term describes the coupling of the mode $\hat{a}$ and $\hat{b}$ to their respective thermal environment with damping rates $\gamma_{a/b}$ and thermal occupation numbers $N_{a/b}$. The second term describes the engineered dissipative processes that lead to entanglement, and in the limit of $N_c = 0$, it reduces to equation (5.30) with the corresponding rate $\Gamma_{\mathrm{sq}} = \tilde{g}^2/(2\Gamma_{\mathrm{ph}})$. Note that in the sideband-resolved and weak driving limit this rate scales as $\Gamma_{\mathrm{sq}} \simeq \Gamma_{\mathrm{eff}}/(2\cosh(r))$ compared to the optimized single mode cooling rate, assuming $g_a \approx g_b$ and $\omega_a \approx \omega_b$.

As a consequence, the amount of steady-state entanglement between the two mechanical modes is a results of the competition between the squeezing rate Γ_{sq} and the rates at which the thermal noise perturbs the system, $(N_b+1)\gamma_b$, $(N_a+1)\gamma_a$. To make this statement more precise, one can explicitly solve equation (5.40) for the steady-state ($\dot{\hat{\rho}} = 0$), resulting in:

$$\xi = \frac{\gamma_a N_a + \Gamma_{\mathrm{sq}}\nu^2}{\gamma_a + \Gamma_{\mathrm{sq}}} + \frac{\gamma_b N_b + \Gamma_{\mathrm{sq}}\nu^2}{\gamma_b + \Gamma_{\mathrm{sq}}} - \frac{2\Gamma_{\mathrm{sq}}\mu\nu}{\frac{\gamma_a+\gamma_b}{2} + \Gamma_{\mathrm{sq}}} + 1. \tag{5.41}$$

A pure TMS state can only be achieved in the limit where Γ_{sq} greatly exceeds the thermal noise rate. On the other hand, the larger is $\Gamma_{\mathrm{sq}} \sim (\Omega_1^2 - \Omega_4^2)/\Gamma_{\mathrm{ph}}$, the smaller is the final amount of

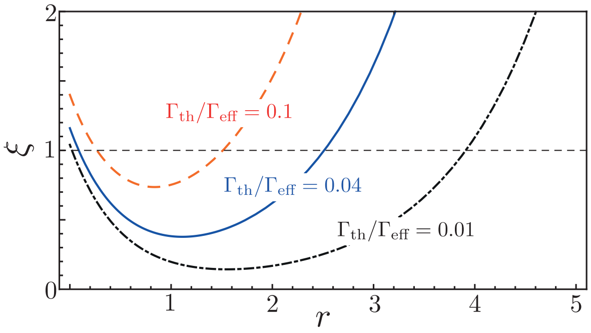

Figure 5.6 – The separability parameter ξ is plotted as a function of the squeezing parameter r for three values of the ratio $\Gamma_{\text{th}}/\Gamma_{\text{eff}}$, in the limit $\gamma_{a,b} \ll \Gamma_{\text{sq}}$ and $\gamma_a N_a = \gamma_b N_b = \Gamma_{\text{th}}$. Vertical dotted line indicates the threshold bellow which the two bending modes are entangled, as given by equation (5.29). For this plot ideal sideband resolved conditions and $N_{\text{c}} = 0$ have been assumed.

squeezing $\tanh r \sim \Omega_4/\Omega_1$. By assuming $\gamma_{a,b} \ll \Gamma_{\text{sq}}$ and $\gamma_a N_a = \gamma_b N_b = \Gamma_{\text{th}}$, the separability criterion can be approximated by

$$\xi \approx \frac{4\Gamma_{\text{th}}}{\Gamma_{\text{eff}}} \cosh(r) + e^{-2r}, \tag{5.42}$$

where again $\Gamma_{\text{eff}} = g_b^2 \Omega_3^2/(\omega_b^2 \Gamma_{\text{ph}})$ is the single mode cooling rate in the well-resolved sideband limit. The dependence of ξ on r is plotted in figure 5.6 for different values of $\Gamma_{\text{th}}/\Gamma_{\text{eff}}$.

5.5.3 Two-mode squeezing by a finite-temperature reservoir

Up to now, in our discussion on two-mode squeezing, we have assumed $N_{\text{c}} = 0$ and the sideband-resolved regime, such that the temperature of the engineered reservoir is zero. We now want to evaluate how sensitive the entanglement is with respect to small deviations from these conditions. In principle, one can use a similar approach as in section 5.5.2 to derive an effective master equation for the two mechanical modes. All the rates are then determined by the fluctuation spectrum $S_{\text{FF}}(\omega)$ (including the four drives) evaluated at the relevant frequencies $\omega = \pm\omega_a, \pm\omega_b$. However, outside the sideband-resolved regime the result would be quite involved and not very illuminating.

Instead, we will here analyze an approximated master equation, which nevertheless captures the most essential effects of a finite effective temperature on the entanglement generation and can thus be adopted to other systems as well.

Let us first point out that when generalized to a finite N_c, the above approach introduces for every dissipation processes associated with the jump operator $\hat{A}$ ($\hat{B}$), a reverse process with operator $\hat{A}^\dagger$ ($\hat{B}^\dagger$). The rates of the original and the reverse processes scale like $(N_\mathrm{c}+1)$ and N_c, respectively. More generally, we can replace N_c by an effective occupation number N_eff, which, similar as in the cooling discussion, also takes into account of the finite overlap of the spectral peaks. Under this assumption we obtain a 'thermal' two-mode squeezing master equation of the form

$$\mathcal{L}_\mathrm{sq}\hat{\rho} \simeq \frac{\Gamma^a_\mathrm{sq}}{2}(N^a_\mathrm{eff}+1)\mathcal{D}[\hat{A}] + \frac{\Gamma^a_\mathrm{sq}}{2}N^a_\mathrm{eff}\mathcal{D}[\hat{A}^\dagger] + \frac{\Gamma^b_\mathrm{sq}}{2}(N^b_\mathrm{eff}+1)\mathcal{D}[\hat{B}] + \frac{\Gamma^b_\mathrm{sq}}{2}N^b_\mathrm{eff}\mathcal{D}[\hat{B}^\dagger]. \tag{5.43}$$

The rates $\Gamma^{a,b}_\mathrm{sq}$ and the effective occupation numbers $N^{a,b}_\mathrm{eff}$ can be estimated from the fluctuation spectrum given in equation (5.20) as

$$\Gamma^{\eta=a,b}_\mathrm{sq} = \frac{S_\mathrm{FF}(\omega_\eta) - S_\mathrm{FF}(-\omega_\eta)}{2\cosh(r)}, \tag{5.44}$$

and

$$N^{\eta=a,b}_\mathrm{eff} = \frac{S_\mathrm{FF}(-\omega_\eta)}{S_\mathrm{FF}(\omega_\eta) - S_\mathrm{FF}(-\omega_\eta)} \geq N_\mathrm{c}. \tag{5.45}$$

Then equation (5.43) becomes exact in the sideband-resolved regime $\omega_{a,b} \gg \Gamma_\mathrm{ph}$ and reproduces as well the correct cooling dynamics in the limit $r \to 0$. While under general conditions equation (5.43) is only a crude approximation, it is still expected to give accurate predictions for the squeezing parameter in the relevant regime $N^{a/b}_\mathrm{eff} < 1$.

In the simplest case of identical mechanical modes, i.e. $\gamma_a N_a = \gamma_b N_b = \Gamma_\mathrm{th}$, $N^a_\mathrm{eff} \simeq N^b_\mathrm{eff} \simeq N_\mathrm{eff}$, $\Gamma^{\eta=a,b}_\mathrm{sq} = \Gamma_\mathrm{eff}/(2\cosh r)$, and assuming again that $\gamma_{a,b} \ll \Gamma_\mathrm{sq}$, we can derive from equation (5.43) a

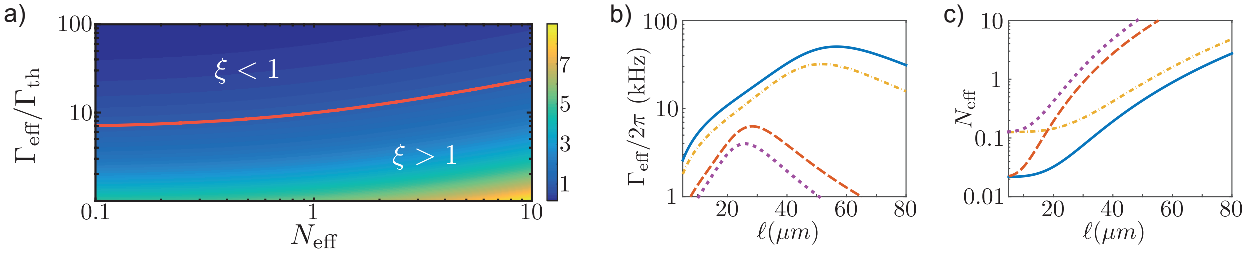

Figure 5.7 – Contour plot of the minimal achievable separability parameter $\xi_{\rm min} = \min\{\xi(r)|r\}$ as a function of the ratio $\Gamma_{\rm eff}/\Gamma_{\rm th}$ and the effective occupation $N_{\rm eff}$. The red line corresponds to the threshold given by the condition $\xi_{\rm min} = 1$. For this plot the parameter $\xi(r)$ has been evaluated using equation (5.46), where equal parameters for the two modes and $\gamma_a = \gamma_b \ll \Gamma_{\rm sq}$ have been assumed. The values of $\Gamma_{\rm eff}$ and $N_{\rm eff}$ are plotted in b) and c) as a function of the length ℓ of the beam. For both plots the values of $T = 100$ mK, $\Gamma_{\rm ph}/(2\pi) = 250$ kHz (solid line), $T = 100$ mK, $\Gamma_{\rm ph}/(2\pi) = 1$ MHz (dashed line), $T = 1$ K, $\Gamma_{\rm ph}/(2\pi) = 1$ MHz (dotted line) and $T = 1$ K, $\Gamma_{\rm ph}/(2\pi) = 250$ kHz (dashed-dotted line) have been assumed. All the other parameters are the same as in figure 5.4.

generalized expression for the separability parameter,

$$\xi \approx \frac{4\Gamma_{\rm th}}{\Gamma_{\rm eff}} \cosh(r) + (1 + 2N_{\rm eff})e^{-2r}, \tag{5.46}$$

which reproduces equation (5.42) for $N_{\rm eff} = 0$. In figure 5.7 (a) we plot the value of ξ minimized with respect to r for different ratios $\Gamma_{\rm eff}/\Gamma_{\rm th}$ and effective reservoir occupation numbers $N_{\rm eff}$. This plot provides a general overview on the minimal conditions required for the dissipative preparation of entangled mechanical states. In particular, it shows that the two-mode squeezing scheme does not rely on a strict zero reservoir temperature. Indeed, the steady-state entanglement is rather robust with respect to $N_{\rm eff}$, which is related to the fact that the thermal fluctuations of the environment become squeezed as well. However, note that for $N_{\rm eff}^{a/b} \gtrsim 1$ the current approach can only provide a crude approximation for the squeezing parameter.

For the current setup, the expected values for $\Gamma_{\rm eff}$ and $N_{\rm eff}$ are plotted in figures 5.7 (b) and (c) as a function of the beam length and for different values of $\Gamma_{\rm ph}$ and the support temperature T. For $T = 100$ mK and $Q = 10^6$ the relevant thermalization rate is $\Gamma_{\rm th}/2\pi \approx 2$ kHz, which shows that for $\ell \approx 30 - 70\,\mu$m the conditions for steady-state entanglement can be reached. Importantly, since the fundamental limit, $N_{\rm eff} \simeq N_{\rm c}$, remains small for temperatures up to $T \approx 4$K, a slightly improved coupling constant or Q-value would enable the dissipative generation of entanglement at these more convenient temperatures.

6

Parity-time-symmetry breaking in the steady state

In this chapter, we consider a system of coupled mechanical oscillators (similar to the ones discussed throughout this thesis), one with loss and the other with gain. This mechanical loss and gain could be realised via optically-induced cooling and heating respectively. In this sense, the methods and schemes described in chapters 3, 4 and 5 constitute prominent candidates for the realisation of such a system. These mechanical gain-loss systems provide a playground for exploring interesting phenomena, such as the breaking of patity-time ($\mathcal{PT}$) symmetry, previously investigated mainly in the context of optical waiveguides. The fact that nano-mechanical systems are subject to nonlinearities and they operate under the influence of thermal and quantum noise, provides access to previously unexplored regimes where surprising new effects come to play. The analysis of these systems were done in collaboration with T. J. Milburn, J. Huber, K. G. Makris, S. Rotter and P. Rabl and the theoretical results were published in New Journal of Physics [59]. For this work, I performed most of the analytical as well as numerical calculations, while the dynamical analysis presented in section 6.4.1 was done together with T. J. Milburn.

6.1 INTRODUCTION

In 1998 Bender and Boettcher [124] described a class of non-Hermitian 'Hamiltonians' that exhibit a purely real energy spectrum, a surprising fact which they attributed to the underlying $\mathcal{PT}$ (parity- and time-reversal) symmetry. Their observation triggered considerable interest in discrete and continuous systems with $\mathcal{PT}$ symmetry along with alternative non-Hermitian formulations of quantum theory [125]. Such fundamental considerations remain speculative, but there exist many classical systems in which $\mathcal{PT}$-symmetric dynamics can be obtained with appropriately engineered loss and gain. This was first pointed out in the context of photonic waveguides [43–46], lattices, and resonators [47–50]. Other examples include cold atoms [51–53] and optomechanical devices [54–56]. Of particular interest in such systems is the *breaking* of $\mathcal{PT}$ symmetry, i.e., when by tuning a parameter the energy spectrum becomes complex and the eigenvectors no longer exhibit the underlying $\mathcal{PT}$ symmetry. This phenomenon was first experimentally observed in optical waveguides [45, 46], and is currently the subject of intense experimental and theoretical research.

Our focus in this chapter is to discuss a way to go beyond this dynamical picture and address an interesting and still open question: what are the *steady* states of actual physical systems with $\mathcal{PT}$ symmetry? This question is mainly motivated by the types of systems that we consider in this work. Specifically, nano-mechanical resonators are subject to nonlinear saturation effects and they operate under the presence of thermal and quantum noise. These features have a crucial influence on the system's dynamics and the long-time behavior can no longer be inferred from an eigenvalue analysis only. By focusing on the experimentally relevant example of coupled mechanical resonators with optically-induced gain and loss (see Fig. 6.2) we show that $\mathcal{PT}$-symmetry breaking in the steady state exhibits various unexpected features and in general occurs via additional intermediate phases with retained or 'weakly' broken $\mathcal{PT}$ symmetry. Most importantly, we identify an unconventional transition from a high-noise balanced energy distribution to a parity-broken lasing state with strongly reduced fluctuations. This transition generalizes the phenomenon of $\mathcal{PT}$-symmetry breaking—hitherto defined only for eigenstates—to steady-state distributions of noisy systems. The mechanisms described here occur in systems of two coupled modes as well as in multi-resonator arrays, and will thus be of relevance for a large range of $\mathcal{PT}$ symmetric systems operated at low amplitudes and close to the quantum regime.

6.2 $\mathcal{PT}$-SYMMETRY BREAKING

We consider a simple but relevant example of two linearly-coupled mechanical oscillators. One of these oscillators is subject to gain and the other to loss, both with the same rate Γ, as shown in figure 6.1 a). In the frame rotating with the bare oscillation frequency ω_0, such a system can be described by a pair of coupled differential equations of the form

$$\begin{pmatrix} \dot{\alpha} \\ \dot{\beta} \end{pmatrix} = -i \begin{pmatrix} i\Gamma & g \\ g & -i\Gamma \end{pmatrix} \begin{pmatrix} \alpha \\ \beta \end{pmatrix}, \tag{6.1}$$

where α and β correspond to the complex oscillation amplitudes for each resonator while g is the coupling strength between them. It is easy to check that the (non-Hermitian) dynamical matrix in the above equation is invariant under parity- and time-reversal. The parity-reversal operation in general corresponds to the operation $\mathcal{P} : x \leftrightarrow -x$, where x a position coordinate. However, since our system is discrete in space, i.e. it can be understood as a two-site lattice, the parity-reversal operation in this case corresponds to the position exchange of the two oscillators, i.e. $\mathcal{P} : (\alpha, \beta)^T \leftrightarrow (\beta, \alpha)^T$. The time-reversal operation is as usual $\mathcal{T} : i \to -i$. The eigenvalues and (unnormalized) eigenstates of this dynamical matrix are given by [126]

$$\lambda_{1,2} = \pm\sqrt{g^2 - \Gamma^2}. \tag{6.2}$$

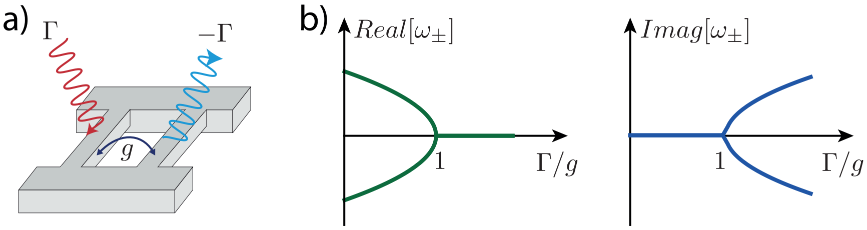

Figure 6.1 – a) Illustration of a PT-symmetric system, consisting of two coupled resonators one with gain and the other with loss of the same magnitude. b) Real (left) and imaginary (right) part of the eigenvalues as function of Γ/g. A transition occurs at $\Gamma/g = 1$, where the PT-symmetry is broken.

and

$$\psi_1 = \begin{pmatrix} e^{i\frac{\theta}{2}} \\ e^{-i\frac{\theta}{2}} \end{pmatrix}, \qquad \psi_2 = \begin{pmatrix} ie^{-i\frac{\theta}{2}} \\ -ie^{i\frac{\theta}{2}} \end{pmatrix}, \qquad \sin(\theta) = \Gamma/g, \tag{6.3}$$

respectively. We observe that for $\Gamma \leq g$ both eigenvalues $\lambda_\pm$ are real and the eigenvectors are also eigenstates of the symmetry operator, i.e. $\mathcal{PT}v_{1,2} = v_{1,2}$. Above that point, both eigenvalues are imaginary indicating the existence of a gain and a loss eigenmode. In this parameter regime the angle θ is complex and $v_{1,2}$ no longer posses the same symmetry as the Hamiltonian, i.e. the parity-time symmetry. Thus one speaks of a parity-time symmetry breaking transition occurring at $\Gamma = g$ [see figure 6.1 b)]. This particular feature is related to surprising —and often counterintuitive— effects first observed in the context of photonic waveguides [43–46], lattices, and resonators [47–50].

Up to now, we have assumed that the gain and loss rate Γ is a constant. However, in realistic physical systems, this cannot be true. In fact, Γ is generally expected to be a non-linear function of the oscillation energy, due to saturation effects. In addition, the background noise to which such classical systems are normally subject needs also to be taken into account.

6.3 $\mathcal{PT}$-SYMMETRIC PHONON SYSTEMS

To motivate our further analysis in this chapter by a concrete physical system, we consider a setup of two micro-mechanical resonators—similar to the systems described in chapter 2—as shown in figure 6.2 a). The main findings discussed below, however, are more general and can be studied in other equivalent realizations, e.g., with coupled optical or microwave resonators. The mechanical resonators have a bare vibrational frequency ω_{m} and they are mutually coupled, e.g., mechanically via the support, with strength g. In addition, optical or electrical cooling [5, 6, 8, 10, 57] and pumping [34–38, 40, 41, 57] schemes, similar to the ones described in chapters 3, 4 and 5 are used to induce mechanical loss for one resonator and an *equal* amount of mechanical gain for the other. In a frame rotating with ω_{m}, the semiclassical dynamics of the system is then described by the Itô stochastic differential equation [61, 127]

$$\begin{pmatrix} \dot{\alpha} \\ \dot{\beta} \end{pmatrix} = \begin{pmatrix} \Gamma_{+}(\alpha) & -ig \\ -ig & \Gamma_{-}(\beta) \end{pmatrix} \begin{pmatrix} \alpha \\ \beta \end{pmatrix} + \begin{pmatrix} F_{+}(t) \\ F_{-}(t) \end{pmatrix}, \tag{6.4}$$

where α and β are the dimensionless amplitudes of the pumped and cooled mode respectively.

The optically-induced gain and loss rates considered here are of the form

$$\Gamma_{\pm}(\alpha) = \pm \frac{\Gamma}{(1 + |\alpha|^2/n_0)^{\nu}} - \gamma, \tag{6.5}$$

where Γ is the maximal rate and $\sqrt{n_0}$ is the saturation amplitude. The value of ν characterizes the underlying heating or cooling mechanism and will be treated here as an adjustable parameter. For the three-level scheme depicted in figure 6.2 b)—discussed in detail in chapter 4—this parameter takes the value $\nu = 2$ [see equation (4.33)]. Instead, for conventional laser amplification with inverted two-level systems we would obtain $\nu = 1$ [see equation (3.52)]. Finally, γ is the bare mechanical damping rate. Since we are interested in the $\mathcal{PT}$-symmetric limit (defined below), we assume $\gamma/\Gamma \rightarrow 0$. However, in all our calculations we retain a finite $\gamma > 0$, which describes the actual physical situation and results in a well-defined steady state for all parameter regimes.

In equation (6.4) the (complex) stochastic forces $F_{\pm}(t)$ represent two independent white-noise

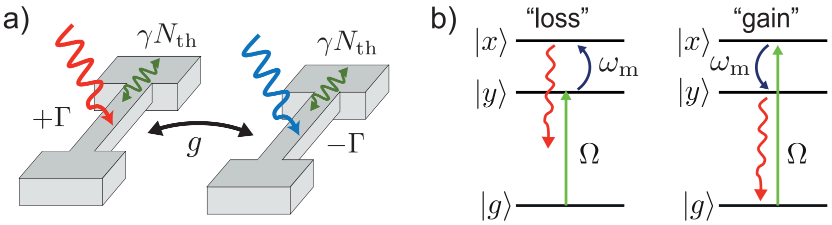

Figure 6.2 – a) Setup of two coupled mechanical resonators with optically-induced gain and loss. b) Scheme for engineering mechanical gain or loss via an optically-driven three-level defect. Depending on the detuning of the pump (green arrow), phonon-induced transitions between the two near-degenerate excited states $|x\rangle$ and $|y\rangle$ lead to a net absorption or emission of phonons of frequency $\omega_{\rm m}$ (see chapter 4 for more details).

processes with $\langle F_\pm^*(t)F_\pm(t')\rangle = D_\pm\delta(t-t')$. For resonators coupled to a reservoir of temperature T the diffusion rates are $D_+(\alpha) = D_{\rm q}(\alpha)+2\gamma N_{\rm th}$ and $D_- = 2\gamma N_{\rm th}$, where $N_{\rm th} = (e^{\hbar\omega_{\rm m}/k_BT}-1)^{-1}$. As shown in section 3.2.1 in chapter 3, the contribution $D_{\rm q}(\alpha\to 0) = 2\Gamma$ for the gain mode represents the intrinsic quantum noise associated with any amplification process and suggests that noise is a fundamental property of $\mathcal{PT}$-symmetric systems [128–130].

6.4 Steady state of $\mathcal{PT}$-symmetric systems in the absence of noise

We now evaluate the stationary state $\psi_{\rm ss} = (\alpha_{\rm ss}, \beta_{\rm ss})^T$ of equation (6.4), first in the absence of noise. Figures 6.3 a) and b) show the mode occupation numbers $|\alpha_{\rm ss}|^2$ and $|\beta_{\rm ss}|^2$ as a function of Γ/g, and for the two relevant cases $\nu = 2$ and $\nu = 1$. Firstly, we observe in both plots the expected transition at $\Gamma/g|_{\mathbf{I}\to\mathbf{II}} = 1$. Below this point (phase **I**) the system dynamics is oscillatory, as expected from the discussion of the $\mathcal{PT}$-symmetric phase above.

Above this transition point (phase **II**) the linearized system dynamics becomes unstable and both resonators reach a finite steady-state occupation number, determined by the saturation of $\Gamma_\pm(\alpha)$. However, this steady state is still an eigenstate of the symmetry operator, $\mathcal{PT}\psi_{\rm ss} \propto \psi_{\rm ss}$, and contrary to our naïve expectation the system remains $\mathcal{PT}$-symmetric beyond the conventional transition point. The existence of a $\mathcal{PT}$-symmetric steady-state with non-vanishing amplitude can

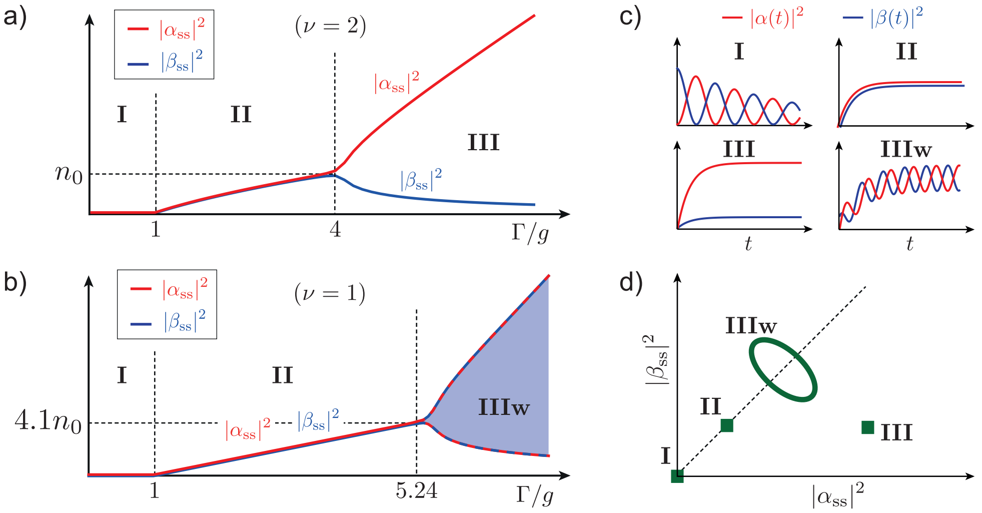

Figure 6.3 – Steady state $\psi_{\rm ss} = (\alpha_{\rm ss}, \beta_{\rm ss})^T$ of the $\mathcal{PT}$-symmetric phonon system in the absence of noise. The steady state occupation numbers $|\alpha_{\rm ss}|^2$ and $|\beta_{\rm ss}|^2$ of the two modes are plotted for a) $\nu = 2$ and b) $\nu = 1$ and $\gamma/g = 10^{-3}$. In the limit-cycle phase **IIIw** both modes oscillate over the range indicated by the shaded area. c) Illustration of the relaxation dynamics of $|\alpha|^2$ (red) and $|\beta|^2$ (blue). d) The resulting steady state (green square) for each phase.

be traced back to the fact that in the present model the $\mathcal{PT}$-symmetry is retained even in the nonlinear regime. This means that for equal amplitudes, $\alpha = \beta$, the gain and the loss rate are still exactly the same, i.e., $\Gamma_+(\alpha) = -\Gamma_-(\alpha)$, $\forall\alpha$ [see equation (6.5)]. This property of the nonlinear system implies that there exists a symmetric state $\psi_{\rm ss}(\alpha_{\rm ss}, \beta_{\rm ss})^T$, with $|\alpha_{\rm ss}| = |\beta_{\rm ss}|$, which satisfies $\dot{\psi}_{\rm ss} = 0$ for *all* values of Γ/g. However, as one can see in figure 6.3, at larger values of Γ the system eventually switches to a different, symmetry-broken state.

6.4.1 Dynamical analysis

More specifically, by moving to polar coordinates $\alpha = re^{i\theta_\alpha}$ and $\beta = ze^{i\theta_\beta}$, equation (6.4) can be rewritten as

$$\dot{r} = -[\gamma - \Gamma(r)]r - g\sin(\phi)z, \tag{6.6}$$

$$\dot{z} = -[\gamma + \Gamma(z)]z + g\sin(\phi)r, \tag{6.7}$$

$$\dot{\phi} = g\left(\frac{r}{z} - \frac{z}{r}\right)\cos(\phi), \tag{6.8}$$

where $\phi = \theta_\alpha - \theta_\beta$. Note that the system is invariant under a combined rotation of α and β and therefore the evolution of the total phase $\theta_\alpha + \theta_\beta$ can be neglected. For the last equation we see that there are two fixed points for the phase, $\phi_{\text{ss}} = \pm\pi/2$. Due to finite γ, the stationary occupation number of the gain mode $|\alpha|^2$ is always slightly larger than that of the loss mode $|\beta|^2$, therefore $\phi_{\text{ss}} = \pi/2$ is the stable. We therefore set $\phi = \pi/2$ and study the two-dimensional dynamical system with variables r and z. We now apply standard dynamical analysis to understand the phases mentioned above and predict the transition points. To do so we first evaluate the possible stationary solutions r_{ss} and z_{ss} of equations (6.6) and (6.7), which are given by the solutions of

$$gz_{\text{ss}} = [\Gamma(r_{\text{ss}}) - \gamma]r_{\text{ss}}, \qquad gr_{\text{ss}} = [\Gamma(z_{\text{ss}}) + \gamma]z_{\text{ss}}. \tag{6.9}$$

The stability of these fixed points is then analyzed using the trace-determinant plane of the Jacobian, i.e. the dynamical matrix of the system linearized about the stationary state. The Jacobian for our system is

$$\mathbf{J} = \begin{pmatrix} \Gamma'(r_{\text{ss}})r_{\text{ss}} + \Gamma(r_{\text{ss}}) - \gamma & -g \\ g & -\Gamma'(z_{\text{ss}})z_{\text{ss}} - \Gamma(z_{\text{ss}}) - \gamma \end{pmatrix}, \tag{6.10}$$

where the prime denotes the derivative. The trace and determinant of $\mathbf{J}$ are

$$\tau = \operatorname{Tr}\mathbf{J} = -2\gamma + \Gamma'(r_{\rm ss})r_{\rm ss} - \Gamma'(z_{\rm ss})z_{\rm ss} + \Gamma(r_{\rm ss}) - \Gamma(z_{\rm ss}), \tag{6.11}$$

$$\delta = \det\mathbf{J} = g^2 - [\Gamma'(r_{\rm ss})r_{\rm ss} + \Gamma(r_{\rm ss}) - \gamma][\Gamma'(z_{\rm ss})z_{\rm ss} + \Gamma(z_{\rm ss}) + \gamma] \tag{6.12}$$

respectively. Since the eigenvalues of $\mathbf{J}$ may be written entirely in terms of τ and δ thus

$$\lambda_{\pm} = \tfrac{1}{2}(\tau \pm \sqrt{\tau^2 - 4\delta}), \tag{6.13}$$

evaluating τ and δ at a particular stationary state fully characterizes its stability and local dynamical structure. As we shall discuss now, the details of this $\mathcal{PT}$-symmetry-breaking mechanism and the resulting state depend on the actual form of the saturable gain, which is here determined by the parameter ν.

The state $|\alpha_{\rm ss}|^2 = |\beta_{\rm ss}|^2 = 0$ is an obvious stationary state of equations (6.6) and (6.7) and is guaranteed by the inclusion of a finite $\gamma > 0$, which leads to a slow overall decay towards a well-defined steady state. Substituting this into equations (6.11) and (6.12) yields (first order in γ)

$$\tau = -2\gamma, \qquad \delta = g^2 - \Gamma^2. \tag{6.14}$$

This corresponds to a stable spiral for $\Gamma < g$, but for $\Gamma > g$ becomes a saddle node. We thus conclude that phase **I** is stable for

$$0 < \frac{\Gamma}{g} < 1, \tag{6.15}$$

independently from the parameter ν.

In phase **II** the two occupation numbers are roughly equal, however simply assuming $r_{\rm ss} = z_{\rm ss}$ yields an inconsistency due to finite γ. Let us therefore substitute the ansatz $r_{\rm ss} = r_{\rm ss}^{(0)} + \gamma r_{\rm ss}^{(1)} + \ldots$

and $z_{\rm ss} = r_{\rm ss}^{(0)} + \gamma r_{\rm ss}^{(1)} + \ldots$ and equate alike-orders in γ. The result is

$$\begin{aligned} r_{\rm ss}^{(0)} &= \sqrt{n_0} \times \sqrt{(\Gamma/g)^{1/\nu} - 1}, \\ r_{\rm ss}^{(1)} &= -z_{\rm ss}^{(1)} = r_{\rm ss}^{(0)} [\Gamma'(r_{\rm ss}^{(0)}) r_{\rm ss}^{(0)} + \Gamma(r_{\rm ss}^{(0)}) + g]^{-1}, \end{aligned} \tag{6.16}$$

and in terms of occupation numbers $|\alpha_{\rm ss}|^2/n_0 = |\beta_{\rm ss}|^2/n_0 = (\Gamma/g)^{1/\nu} - 1 + \mathcal{O}(\gamma)$, in accordance with figure 6.3. We neglect terms of order γ^2 and higher. Note that, this stationary state only exists for $\Gamma/g \geq 1$. Substituting equation (6.16) into equations (6.11) and (6.12) yields

$$\tau = -2\gamma \left(1 - \frac{\Gamma''(r_{\rm ss}^{(0)}) r_{\rm ss}^{(0)2} + 2\Gamma'(r_{\rm ss}^{(0)}) r_{\rm ss}^{(0)}}{\Gamma'(r_{\rm ss}^{(0)}) r_{\rm ss}^{(0)} + \Gamma(r_{\rm ss}^{(0)}) + g} \right) \tag{6.17}$$

$$= -2\gamma \left(1 - \frac{2\nu[(\Gamma/g)^{1/\nu} - 1][(2\nu - 1)(\Gamma/g)^{1/\nu} - 2(\nu + 1)]}{2\nu(\Gamma/g)^{1/\nu} + 2(1 - \nu)(\Gamma/g)^{2/\nu}} \right) \tag{6.18}$$

and

$$\delta = g^2 - [\Gamma'(r_{\rm ss}^{(0)}) r_{\rm ss}^{(0)} + \Gamma(r_{\rm ss}^{(0)})]^2 = g^2 - g^2[2\nu - 1 - 2\nu(\Gamma/g)^{-1/\nu}]^2. \tag{6.19}$$

We see that $\delta > 0$ only for $1 < \Gamma/g < [\nu/(\nu - 1)]^\nu$. However, unlike the previous analysis of phase **I**, in this case τ can be positive while δ is positive. This is the case if $[\nu/(\nu - 1)]^\nu > [(\nu + 2\nu^2 + \sqrt{2\nu + 3\nu^2})/(2\nu^2 - 1)]^\nu$. As Γ/g is increased the stationary state (6.16) goes from a stable spiral to an unstable spiral and then to a saddle node. We thus conclude that phase **II** is stable for

$$1 < \frac{\Gamma}{g} < \min\left\{ \left(\frac{\nu + 2\nu^2 + \sqrt{2\nu + 3\nu^2}}{2\nu^2 - 1} \right)^\nu, \left(\frac{\nu}{\nu - 1} \right)^\nu \right\}. \tag{6.20}$$

Considering the case $\nu = 2$, this gives $1 < \Gamma/g < 4$, while for $\nu = 1$ one obtains $1 < \Gamma/g < 5.2$, in consistency with figure 6.3.

In a similar fashion, we analise the phases in regimes **IIIw** and **III**. In particular, we conclude that phase **IIIw** is a limit cycle exhibited for

$$\left(\frac{\nu + 2\nu^2 + \sqrt{2\nu + 3\nu^2}}{2\nu^2 - 1}\right)^{\nu} < \frac{\Gamma}{g} < \left(\frac{\nu}{\nu - 1}\right)^{\nu}. \tag{6.21}$$

Since it is only possible that $[\nu/(\nu-1)]^{\nu} > [(\nu+2\nu^2+\sqrt{2\nu + 3\nu^2})/(2\nu^2-1)]^{\nu}$ if $1 \leq \nu < 2$, this phase cannot be observed for $\nu \geq 2$. The limit cycle does not admit a simple analytic form, however by assuming that it is small and centered on stationary state (6.16), one may approximate its frequency ω_{osc} by the imaginary part of the eigenvalue of the Jacobian evaluated at equation (6.16). One finds $\omega_{\text{osc}} \approx 2\sqrt{g^3(\Gamma - g)}/\Gamma$; this result has been numerically verified for the case $\nu = 1$. On the other hand, the phase **III** corresponds two extra stationary states one unstable and the other stable. We conclude that phase **III** is exhibited for

$$\frac{\Gamma}{g} > \left(\frac{\nu}{\nu - 1}\right)^{\nu}. \tag{6.22}$$

Note that this phase cannot be observed for $\nu = 1$. For $\nu = 2$ one may easily check that, given $\Gamma/g > [\nu/(\nu - 1)]^{\nu} = 4$, the stable stationary amplitudes are

$$r_{\text{ss}}/\sqrt{n_0} = \{[\Gamma + \sqrt{\Gamma(\Gamma - 4g)}]/(2g) - 1\}^{1/2}, \tag{6.23}$$

$$z_{\text{ss}}/\sqrt{n_0} = \{[\Gamma - \sqrt{\Gamma(\Gamma - 4g)}]/(2g) - 1\}^{1/2}, \tag{6.24}$$

or in terms of occupation numbers

$$\left.\begin{matrix} |\alpha_{\text{ss}}|^2 \\ |\beta_{\text{ss}}|^2 \end{matrix}\right\} = n_0 \times \left(\frac{\Gamma \pm \sqrt{\Gamma(\Gamma - 4g)}}{2g} - 1\right). \tag{6.25}$$

While similar nonlinear phenomena are in general expected for gain-loss systems [56, 131–133], our specific interest here is to understand the role of dynamical instabilities in the breaking of a steady-state symmetry. In particular, the above analysis shows that $\mathcal{PT}$-symmetry breaking occurs even in systems where the symmetry is fully retained in the nonlinear regime and a symmetric steady-state would be permitted in principle for all parameters.

6.5 STEADY STATE IN NOISY $\mathcal{PT}$-SYMMETRIC SYSTEMS

We now show how the above picture changes in the presence of noise. For clarity we restrict ourselves to a system which is dominated by thermal diffusion, i.e. $D_\pm = D = 2\gamma N_{\rm th}$. For $\Gamma = 0$ thermal noise induces additional amplitude fluctuations of about $(\Delta\alpha)^2 \approx D/(2\gamma) = N_{\rm th}$, and we expect that as long as $N_{\rm th} < n_0$ the characteristic features shown in figure 6.3, which scale with the saturation number n_0, will only be smeared out, but not change significantly. This is confirmed numerically (not shown) and means that figure 6.3 is a good representation of the steady states of the system in the weakly nonlinear or low-noise regime. Therefore, we will now address the opposite regime $N_{\rm th} \gg n_0$.

Figure 6.4 a) shows the results of a numerical simulation of the stochastic equation (6.4), from which we obtain the steady-state distribution $P_{\rm ss}(\alpha, \beta)$ for $\nu = 2$ and $N_{\rm th}/n_0 = 10$. In the following we write $\alpha = re^{i\theta_\alpha}$ and $\beta = ze^{i\theta_\beta}$ and make use of the fact that the system dynamics is invariant under a global phase rotation. The exact marginal distributions $P_{\rm ss}(\alpha)$ and $P_{\rm ss}(\beta)$ are then fitted by approximate distributions of the form

$$P(\alpha) \sim re^{-\frac{(r-r_0)^2}{\Delta\alpha^2}}, \qquad P(\beta) \sim ze^{-\frac{(z-z_0)^2}{\Delta\beta^2}}, \tag{6.26}$$

which allows us to extract a radial shift r_0 and z_0 and the range of fluctuations $(\Delta\alpha)^2$ and $(\Delta\beta)^2$ for both modes (see Appendix A for further details on the numerical simulations). From these values plotted in figure 6.4 a) we see that the thermal noise now completely washes out the features

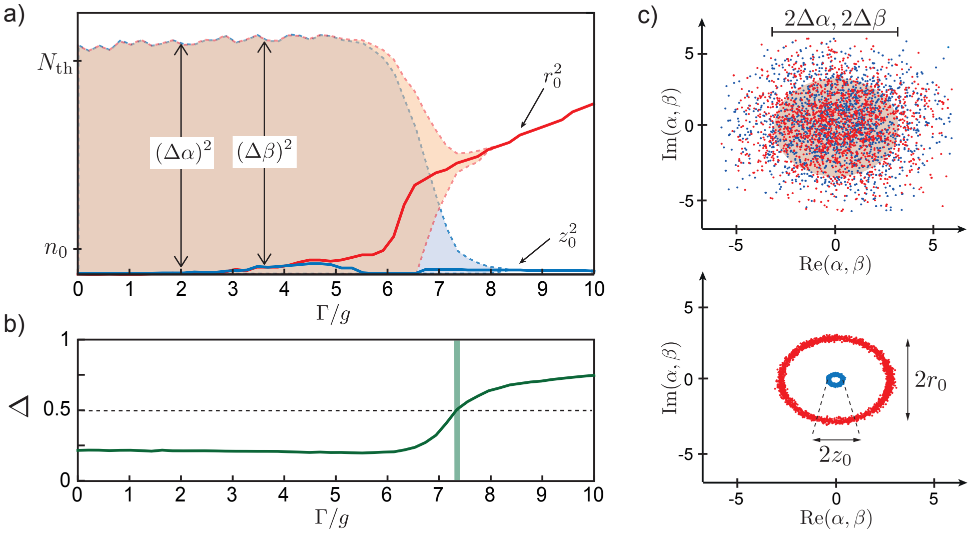

Figure 6.4 – $\mathcal{PT}$-symmetry breaking in the limit of large thermal noise, $N_{\rm th} \gg n_0$. a) Steady-state distributions of α and β for $N_{\rm th}/n_0 = 10$ and $\gamma/g = 10^{-3}$. The values of r_0 and z_0 (solid lines) represent the radial distance of the distribution maxima from the origin and shaded areas indicate the range of fluctuations. b) Plot of the $\mathcal{PT}$-symmetry parameter Δ defined in equation (6.27). c) Steady-state distribution of α (red dots) and β (blue dots) in the thermal ($\Gamma/g = 2$, left plot) and in the symmetry-broken ($\Gamma/g = 10$, right plot) phases.

associated with the $\mathcal{PT}$-symmetric phases **I** and **II**, and for a large range of Γ the system reaches a steady state (phase **T**), which is to a good approximation thermal, i.e., $r_0 = z_0 = 0$ and $(\Delta\alpha)^2 \simeq (\Delta\beta)^2 \simeq N_{\rm th}$. Only after a critical value of $\Gamma/g|_{\mathbf{T}\to\mathbf{III}} \approx 7.5$ are the fluctuations suddenly strongly suppressed. In this regime the system relaxes into an asymmetric coherent state with $r_0 > z_0$ approximately given by the amplitudes $|\alpha_{\rm ss}|$ and $|\beta_{\rm ss}|$ given in equation (6.25) and $(\Delta\alpha)^2, (\Delta\beta)^2 \sim \gamma N_{\rm th}\Gamma/g^2, \gamma N_{\rm th}/\Gamma \ll 1$.

Before we proceed, let us connect this transition to the phenomenon of $\mathcal{PT}$-symmetry breaking—hitherto defined only for individual states. To do so we introduce the $\mathcal{PT}$-symmetry parameter

$$\Delta = \frac{\langle(|\alpha| - |\beta|)^2\rangle_{\rm ss}}{\langle|\alpha|^2\rangle_{\rm ss} + \langle|\beta|^2\rangle_{\rm ss}} \leq 1, \tag{6.27}$$

which vanishes for a random set of states $\psi_i = (\alpha_i, \beta_i)^T$ if and only if each state satisfies $\mathcal{PT}\psi_i =$

$e^{i\theta_i}\psi_i$, with some real phase θ_i. Figure 6.4 b) shows that indeed Δ changes at the transition point from $\Delta \simeq \Delta_{\text{th}} = 0.215$ for a thermal state to $\Delta \to 1$ in the symmetry-broken phase. Note that also in the low-noise limit we obtain $\Delta = \Delta_{\text{th}} > 0$ in phase **I** and therefore only phase **II**, where $\Delta \simeq 0$, has a strictly $\mathcal{PT}$-symmetric steady state.

One of the most striking features visible in figures 6.4 a) and c) is that in sharp contrast to a conventional lasing transition, the emerging coherent-state amplitudes after the $\mathcal{PT}$-symmetry breaking point are even smaller than the original level of thermal noise. This surprising effect can be understood as follows. Although at each instant in time the amplitudes $\alpha(t)$ and $\beta(t)$, and therefore the gain and loss rates $\Gamma_+(\alpha)$ and $\Gamma_-(\beta)$, can be quite different, the average dissipation rate $\bar{\Gamma} = \langle \Gamma_- - \Gamma_+ \rangle_{\text{ss}}$ when evaluated in the thermal phase vanishes, $\bar{\Gamma} \sim \mathcal{O}(\gamma) \sim 0$. What remains (on average) is the weak coupling to the high-temperature environment. In contrast, in the symmetry-broken phase we have $\langle |\alpha| \rangle_{\text{ss}} \gg \langle |\beta| \rangle_{\text{ss}}$. Therefore, there is a strong imbalance between loss and gain on average, i.e., $\bar{\Gamma} \sim \mathcal{O}(\Gamma) > 0$, and the resulting net cooling effect suppresses fluctuations. Thus, this transition in the average dissipation rate of a stationary system can be seen as the counterpart of the transition from real to imaginary eigenvalues in the conventional definition of $\mathcal{PT}$-symmetry breaking. What we are still missing, however, is a simple criterion, which tells us why the system favors one or the other steady state.

To clarify the mechanism behind the symmetry-breaking transition we focus on the symmetry-broken regime $\Gamma/g \gg 1$, where we can assume that the amplitude of the gain mode $|\alpha(t)| \approx |\alpha_{\text{ss}}|$ and the relative phase $\phi \simeq \pi/2$ are approximately constant. We then obtain the equation of motion for the amplitude of the loss mode, $z = |\beta|$ (an equivalent analysis predicts a single stable minimum for the gain mode and much lower thermal activation rates for the relative phase ϕ),

$$\partial_t z = -\partial_z U(z) + \sqrt{\gamma N_{\text{th}}}\eta_z(t), \tag{6.28}$$

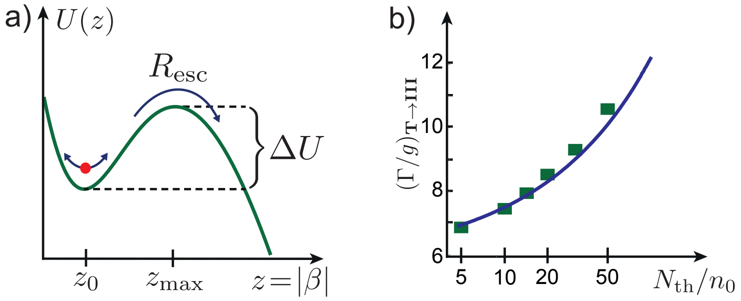

Figure 6.5 – a) Effective potential for the amplitude $z = |\beta|$ of the loss mode for $\Gamma/g = 12$. b) Dependence of the symmetry breaking point $\Gamma/g|_{\mathbf{T}\to\mathbf{III}}$ on N_{th}. The solid line represents the prediction from our analytic model and the squares show the transition points obtained from the condition $\Delta = 0.5$ in numerical simulations.

where $\langle \eta_z(t)\eta_z(t')\rangle = \delta(t-t')$ and (for $\gamma \to 0$)

$$U(z) = -\frac{n_0\Gamma}{2(1+z^2/n_0)} - g|\alpha_{\mathrm{ss}}|z\sin(\phi) - \frac{\gamma N_{\mathrm{th}}}{2}\log(z). \tag{6.29}$$

The function $U(z)$ is an effective potential for z, which is sketched in Fig. 6.5 a). This potential has a local minimum at $z_0 = |\beta_{\mathrm{ss}}|$ (corresponding to the steady state given in equation (6.25) for $N_{\mathrm{th}} \to 0$), which is separated by a finite barrier ΔU from the unstable region $z > z_{\max}$. In the presence of noise, a system initially located at $z \approx z_0$ can escape over this barrier via thermally activated processes with a characteristic rate $R_{\mathrm{esc}} \simeq R_0 e^{-\frac{2\Delta U}{\gamma N_{\mathrm{th}}}}$, where $R_0 = \sqrt{-U''(z_{\min})U''(z_{\max})/(4\pi^2)}$ [127]. This rate increases as Γ is reduced and once R_{esc} exceeds the bare damping γ, any configuration with fixed α and β is rapidly destabilized and the transition to a quasi-thermal state with strongly fluctuating amplitudes occurs. In figure 6.5 b) we compare the transition point $\Gamma/g|_{\mathbf{T}\to\mathbf{III}}$ obtained from the condition $\gamma = R_{\mathrm{esc}}$ with the numerically evaluated values for various $N_{\mathrm{th}}/n_0 \gg 1$. The plot shows that $\mathcal{PT}$-symmetry breaking in the large-noise regime is very well described by this thermal activation model.

6.6 ARRAYS

Finally, the above analysis can be generalized to the case of a coupled resonator array, illustrated in figure 6.6 a). In such a system, the resonator amplitudes α_n and β_n —where n is the number of the unit cell (resonator pair)— obey coupled equations of the form

$$\begin{pmatrix} \dot{\alpha}_n \\ \dot{\beta}_n \end{pmatrix} = \begin{pmatrix} \Gamma & -ig \\ -ig & -\Gamma \end{pmatrix} \begin{pmatrix} \alpha_n \\ \beta_n \end{pmatrix} - ig' \begin{pmatrix} \beta_{n-1} \\ \alpha_{n+1} \end{pmatrix}, \tag{6.30}$$

where now we have included a different coupling g' between the unit cells. By assuming periodic boundary conditions and inserting plain-wave solutions of the form

$$\alpha_n = Ae^{ikn-i\omega t}, \qquad \beta_n = Be^{ikn-i\omega t}, \tag{6.31}$$

where $k = 2\pi j/N$, with N being the number of resonator pairs in the system, we obtain the eigenvalues

$$\omega_\pm(k) = \pm\sqrt{|g_k|^2 - \Gamma^2}, \qquad g_k = g + g'e^{ik}. \tag{6.32}$$

This is similar as above, but for each mode the transition point is now determined by the coupling g_k. The transition occurs at different point for each quasi-momentum as illustrated in Figs. 6.6 b) and c). Note that for $g = g'$ and $N/2$ even, we have $g_{k=\pi} = 0$. In this case the transition occurs for arbitrarily small values of Γ.

Similarly to the case of a pair of coupled resonators, we now show that $\mathcal{PT}$-symmetry breaking in the steady state exists also for extended systems. In particular, we generalize the analysis and

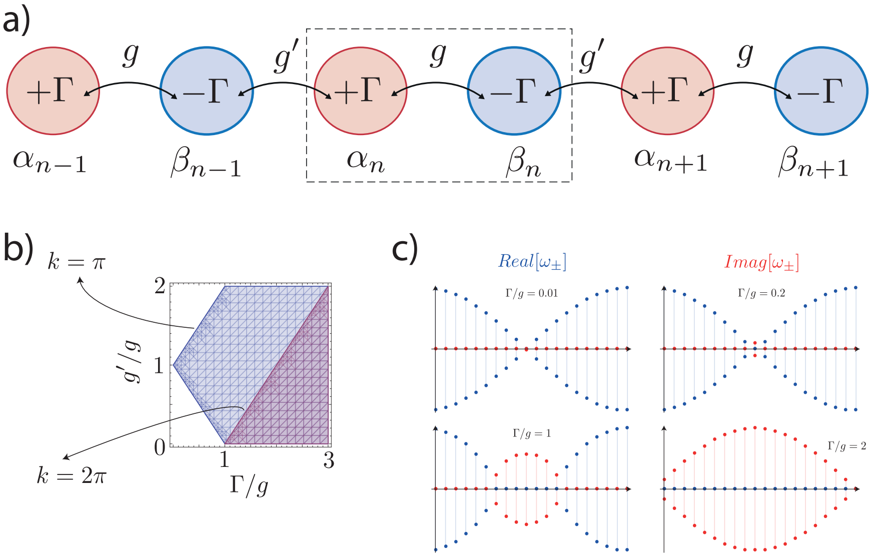

Figure 6.6 – a) Schematic representation of an array of coupled resonators with a parity-time-symmetric unit cell. b) Phase portrait showing the first and the last momenta that go unstable as we increase Γ/g, for various values of the coupling ratio g'/g. c) Real (blue) and imaginary (red) part of the eigenvalues, for various values of Γ/g.

consider coupled equations for each unit cell of the form

$$\begin{pmatrix} \dot{\alpha}_n \\ \dot{\beta}_n \end{pmatrix} = \begin{pmatrix} \Gamma_+(\alpha_n) & -ig \\ -ig & \Gamma_-(\beta_n) \end{pmatrix} \begin{pmatrix} \alpha_n \\ \beta_n \end{pmatrix} - ig' \begin{pmatrix} \beta_{n-1} \\ \alpha_{n+1} \end{pmatrix} + \begin{pmatrix} F_{n,+}(t) \\ F_{n,-}(t) \end{pmatrix}, \tag{6.33}$$

where g' is the coupling between the unit cells and $F_{n,\pm}(t)$ are independent thermal noise processes. Figure 6.7 summarizes the numerical results for the steady state of an array of $N=12$ resonators with periodic boundary conditions and $\nu=2$. The observed features can be understood from the plane wave ansatz [134, 135] $\alpha_n = A_k e^{ikn}$, $\beta_n = B_k e^{ikn}$, where $k = 4\pi j/N$. This ansatz maps equation (6.33) onto a two-mode problem for A_k and B_k, which is equivalent to equation (6.4), but with the replacement $g \mapsto g_k = |g + g' e^{ik}|$. By considering now each of the modes separately, we see that all the transition points identified above occur first for the mode with the largest value of ratio $\Gamma/|g_k|$, or equivalently, the smallest value of $|g_k|$. Since in our model g and g' are assumed to

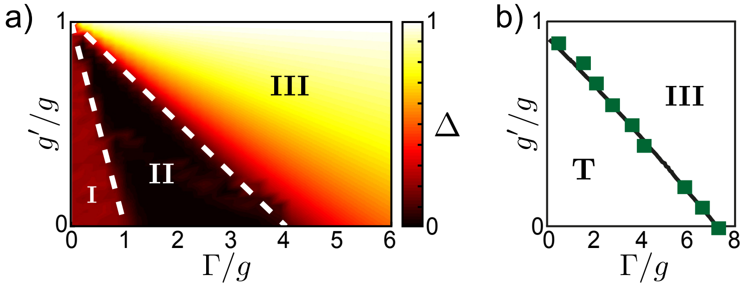

Figure 6.7 – Steady state of a $\mathcal{PT}$-symmetric array of $N = 12$ resonators. a) The different phases are characterized by the symmetry parameter Δ of a single unit cell and the white-dashed lines indicate the phase boundaries obtained from a plane wave ansatz. b) The solid line shows the analytic prediction for the phase boundary between the thermal and symmetry-broken phase and the green squares are the transition points obtained numerically. For both plots $\gamma/g = 10^{-3}$ and $\nu = 2$, such that the line $g' = 0$ corresponds to the setting considered in figures 6.3 a) and 6.4.

be real and positive, this minimal coupling is alway achieved for the $k = \pi$ mode, which therefore determines the symmetry-breaking properties of the array [136, 137]. For an even number of unit cells and the special case $g = g'$, i.e., $g_k = 0$, the gain and the loss modes completely decouple, and the $\mathcal{PT}$-symmetry breaking transitions, both in the linear and nonlinear regime, already occur at $\Gamma|_{\mathbf{I}\to\mathbf{II}} \simeq \Gamma|_{\mathbf{II}\to\mathbf{III}} \simeq \Gamma|_{\mathbf{T}\to\mathbf{III}} \simeq 0$. For linear $\mathcal{PT}$-symmetry chains this instability at $\Gamma = 0$ has already been pointed in previous works [49, 136, 137]. For all intermediate parameters the phase boundaries in figure 6.7 are obtained from the analytic results for the two-mode problem, but with g replaced by $g - g'$. We see that the single-mode ansatz captures well the relevant physics both in the low- and high-noise regime. Note that, however, in the 'thermal' phase the behavior of the array can actually be much more complicated, since the system may undergo noise-induced jumps between multiple metastable configurations.

7

Summary and outlook

In this doctoral thesis, we have described the strain-induced coupling of nitrogen-vacancy centers to individual vibrational modes of diamond nano-mechanical resonators. We have analyzed cooling and amplification schemes for manipulating the state of these mechanical modes and have shown that it is possible to efficiently achieve ground-state cooling as well as to drive the resonator into a large-amplitude coherent state, a state commonly known as a phonon laser. In addition, we have presented a new approach for realizing mechanical ground-state cooling and schemes for manipulating the state of mechanical beams, by making use of the intrinsic reservoir consisting of the continuum of longitudinal compression modes. We have shown that a single silicon-vacancy center in a diamond nano-scale beam can be used to effectively engineer a mechanical reservoir. This reservoir can be used to perform ground-state cooling, or to prepare squeezed and entangled states of low-freqeuncy bending modes. This can be advantageous in cases where optical dissipation channels are not available or need to be avoided. Finally, we have shown that the combination of cooling and lasing schemes can lead to interesting new effects. In particular, we have analyzed the breaking of parity-time symmetry in the steady state of coupled mechanical systems with loss and gain. We have shown how nonlinearities due to saturation effects and the influence of thermal or quantum noise lead to surprising new phenomena. These new phenomena are not expected from the conventional eigenvalue analysis of idealized parity-time-symmetric systems. This result opens up a whole new discussion on realising and investigating further microscopic systems that possess parity-time symmetry.

This dissertation has answered timely questions in the fields of nano-mechanical systems and parity-time-symmetric systems. Several experimental groups are currently working on the implementation of the proposed cooling schemes [for a recent review see [65]]. However, it has also raised new questions and opened up relevant discussions. In particular, in the case of diamond beams further investigations are necessary in the direction of obtaining efficient schemes for strain-induced coupling between two diamond impurities. Achieving this, can lead to new schemes for quantum information processing with solid state spin qubits. Also, the realisation that already very simple systems with balanced loss and gain are proven to be more complex than previously known, provides an important incentive for further research. Towards this direction, the next step would be to further investigate *quantum* systems possessing this symmetry as well as parity-time-symmetric arrays.

Acknowledgments

I want to thank my supervisor Peter Rabl for his great support, help and valuable feedback from the first day to the very end of my doctorate. Under his supervision and teaching, I was able to quickly launch and master my research line. Working with Peter also had a positive impact to my general conception of sciences and professionalism. My sincere thanks also goes to all my colleagues and professors with whom I had the pleasure to collaborate during these four years. The list includes my dear friend and colleague T. J. Milburn, who unexpectedly passed away a few months before this thesis was written, M.-A. Lemonde, S. Portolan, S. D. Bennett, K. G. Makris, J. Huber, A. Norambuena, J. R. Maze, S. Rotter, and M. D. Lukin.

Last but not the least, I would like to thank my family. This includes my father Vasileios, who unfortunately passed away two months after I started my doctorate, my mother Sofia to whom I am deeply thankful for her support throughout my entire life, my sister Olga, my wife Edina who makes my life better in every way and my son Benjamin.

A

Appendix

A.1 NUMERICAL SIMULATIONS

For the numerical results presented in figures. 6.4 and 6.5 in the main text we have simulated the stochastic equations (6.4) (and the corresponding extended set of equations for the array) using the Euler-Maruyama method (see section 15 of [127]). Since we are interested in the steady state of the system, we collect data (complex numbers $\alpha(t)$ and $\beta(t)$) after a time of $5 \times \tau_0$ where $\tau_0 = 1/\gamma$ is approximately the time scale in which the steady state is approached. Over a period of $45 \times \tau_0$ we select 4000 random data points. We repeat the procedure 80 times with random initial conditions.

From the numerical data we obtain the marginal steady-state distributions $P_{\rm ss}(\alpha)$ and $P_{\rm ss}(\beta)$ for the two modes. Since the system is invariant under a combined rotation of α and β in phase space, also the marginal distributions are radially symmetric. Figure A.1 shows examples of the resulting radial distribution $P_{\rm ss}(r = |\alpha|)$ for the gain mode, before, close to, and after the transition.

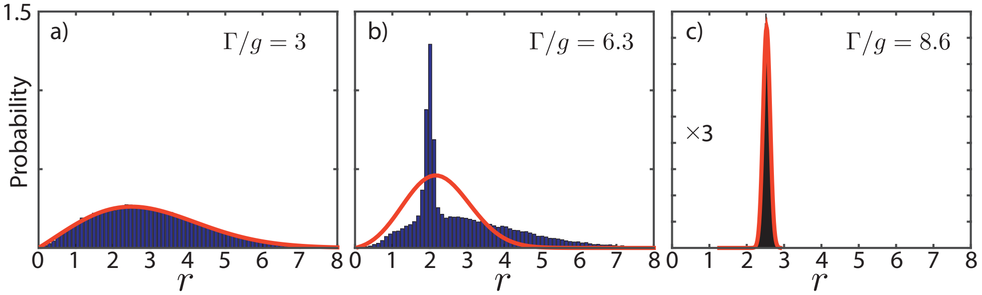

Figure A.1 – Histograms of the real amplitude $r = |\alpha|$ of the resonator with gain and the fitting distribution (red line)—described by equation (A.1)—for three different values of the ratio Γ/g. a) Fitting distribution in the thermal regime, for $\Gamma/g = 3$. b) Fitting distribution in the vicinity of the thermally-activated transition, for $\Gamma/g = 6.3$. c) Fitting distribution in the lasing regime, for $\Gamma/g = 8.6$. Note that the y-axis of the last plot has been scaled by 1/3.

To obtain a simple characterization of the system's steady state, we fit the radial distribution $P_{\mathrm{ss}}(r = |\alpha|)$ by a distribution of the form

$$P_{r_0,\sigma}(r) = \mathcal{N} \times r \times e^{-\frac{(r-r_0)^2}{\sigma^2}}, \tag{A.1}$$

where $\mathcal{N}$ is a normalization constant. It corresponds to a thermal state for $r_0 = 0$ and $\sigma = \sqrt{N_{\mathrm{th}}}$ and approaches the distribution of a coherent state with random phase in the limit $\sigma \ll r_0$. The optimal values for r_0 and σ are obtained by minimization of the squared difference

$$\chi^2(r_0,\sigma) = \sum_{i=1}^{N} \left(H_i - P_{r_0,\sigma}(r_i)\right)^2, \tag{A.2}$$

where H_i represents the hight of the i'th bar of the histogram.

While this fitting procedure yields accurate values for the radial displacement of the distribution maximum, r_0, we find that the corresponding values for the width σ do not very well capture the broad thermal background in the vicinity of the transition [see figure A.1 b)]. Therefore, we use instead the quantity

$$(\Delta\alpha)^2 = \langle|\alpha|^2\rangle - r_0^2, \tag{A.3}$$

where the average $\langle|\alpha|^2\rangle$ is calculated directly from the data set, to represent the range of fluctuations.

Bibliography

[1] M. Aspelmeyer, T. J. Kippenberg, and F. Marquardt. Cavity optomechanics. *Rev. Mod. Phys.*, 86:1391, 2014.

[2] Andrew N. Cleland. *Foundations of Nanomechanics: From Solid-State Theory to Device Applications.* Advanced Texts in Physics. Springer-Verlag Berlin Heidelberg., 2003.

[3] J. Chan. Laser cooling of a nanomechanical oscillator into its quantum ground state. *Nature*, 478:89, 2011.

[4] J. D. Teufel and et al. Sideband cooling of micromechanical motion to the quantum ground state. *Nature (London)*, 475:359, 2011.

[5] I. Wilson-Rae, N. Nooshi, W. Zwerger, and T. J. Kippenberg. Theory of ground state cooling of a mechanical oscillator using dynamical backaction. *Phys. Rev. Lett.*, 99:093901, 2007.

[6] F. Marquardt, J. P. Chen, A. A. Clerk, and S. M. Girvin. Quantum theory of cavity-assisted sideband cooling of mechanical motion. *Phys. Rev. Lett.*, 99:093902, 2007.

[7] C. Genes, D. Vitali, P. Tombesi, S. Gigan, and M. Aspelmeyer. Ground-state cooling of a micromechanical oscillator: Comparing cold damping and cavity-assisted cooling schemes. *Phys. Rev. A*, 77:033804, 2008.

[8] I. Wilson-Rae, P. Zoller, and A. Imamoglu. Laser cooling of a nanomechanical resonator mode to its quantum ground state. *Phys. Rev. Lett.*, 92:075507, 2004.

[9] S. Zippilli, G. Morigi, and A. Bachtold. Cooling carbon nanotubes to the phononic ground state with a constant electron current. *Phys. Rev. Lett.*, 102:096804, 2009.

[10] I. Martin, A. Shnirman, L. Tian, and P. Zoller. Ground-state cooling of mechanical resonators. *Phys. Rev. B*, 69:125339, 2004.

[11] P. Zhang, Y. D. Wang, and C. P. Sun. Cooling mechanism for a nanomechanical resonator by periodic coupling to a cooper pair box. *Phys. Rev. Lett.*, 95:097204, 2005.

[12] K. Jaehne, K. Hammerer, and M. Wallquist. Ground-state cooling of a nanomechanical resonator via a cooper-pair box qubit. *New J. Phys.*, 10:095019, 2009.

[13] J. Wrachtrup and F. Jelezko. Quantum information processing in diamond. *J. Phys.: Condens. Matter*, 18:S807, 2006.

[14] M. W. Dohertya, N. B. Mansonb, P. Delaneyc, F. Jelezko, J. Wrachtrupe, and L. C. L. Hollenberga. The nitrogen-vacancy colour centre in diamond. *Phys. Rep.*, 528:1, 2013.

[15] G. Balasubramanian and et al. Ultralong spin coherence time in isotopically engineered diamond. *Nat. Mater.*, 8:383, 2009.

[16] F. Jelezko, T. Gaebel, I. Popa, A. Gruber, and J. Wrachtrup. Observation of coherent oscillations in a single electron spin. *Phys. Rev. Lett.*, 92:076401, 2004.

[17] P. Ovartchaiyapong, L. M. A. Pascal, B. A. Myers, P. Lauria, and A. C. Bleszynski Jayich. High quality factor single-crystal diamond mechanical resonators. *Appl. Phys. Lett.*, 101:163505, 2012.

[18] Y. Tao, J. M. Boss, B. A. Moores, and C. L. Degen. Single-crystal diamond nanomechanical resonators with quality factors exceeding one million. *Nat. Commun.*, 5(3638), 2014.

[19] P. Rabl, S. J. Kolkowitz, F. H. L. Koppens, J. G. E. Harris, P. Zoller, and M. D. Lukin. A quantum spin transducer based on nanoelectromechanical resonator arrays. *Nat. Phys.*, 6:602, 2010.

[20] S. J. M. Habraken, K. Stannigel, M. D. Lukin, P. Zoller, and P. Rabl. Continuous mode cooling and phonon routers for phononic quantum networks. *New J. Phys.*, 14:115004, 2012.

[21] A. Albrecht, A. Retzker, F. Jelezko, and M. B. Plenio. Coupling of nitrogen vacancy centres in nanodiamonds by means of phonons. *New J. Phys.*, 15:083014, 2013.

[22] S. D. Bennett, N. Y. Yao, J. Otterbach, P. Zoller, P. Rabl, and M. D. Lukin. Phonon-induced spin-spin interactions in diamond nanostructures: Application to spin squeezing. *Phys. Rev. Lett.*, 110:156402, 2013.

[23] C. D. Clark, H. Kanda, I. Kiawi, and G. Sittas. Silicon defects in diamond. *Phys. Rev. B*, 51:16681, 1995.

[24] A. Sipahigil and et al. Quantum interference of single photons from remote nitrogen-vacancy centers in diamond. *Phys. Rev. Lett.*, 108:143601, 2012.

[25] E. Neu and et al. Low-temperature investigations of single silicon vacancy colour centres in diamond. *New J. Phys.*, 15:043005, 2013.

[26] A. Dietrich and et al. Isotopically varying spectral features of siliconvacancy in diamond. *New J. Phys.*, 16:113019, 2014.

[27] L. G. Remus, M. P. Blencowe, and Y. Tanaka. Damping and decoherence of a nanomechanical resonator due to a few two-level systems. *Phys. Rev. B*, 80:174103, 2009.

[28] Ö. O. Soykal, R. Ruskov, and C. Tahan. Sound-based analogue of cavity quantum electrodynamics in silicon. *Phys. Rev. Lett.*, 107:235502, 2011.

[29] R. Ruskov and C. Tahan. On-chip cavity quantum phonodynamics with an acceptor qubit in silicon. *Phys. Rev. B*, 88:064308, 2013.

[30] T. Ramos, V. Sudhir, K. Stannigel, P. Zoller, and T. J. Kippenberg. Nonlinear quantum optomechanics via individual intrinsic two-level defects. *Phys. Rev. Lett.*, 110:193602, 2013.

[31] M. J. Burek. Free-standing mechanical and photonic nanostructures in single-crystal diamond. *Nano Lett.*, 12:6084, 2012.

[32] B. J. M. Hausmann, J. T. Choy, T. M. Babinec, B. J. Shields, I. Bulu, M. D. Lukin, and M. Loncar. Diamond nanophotonics and applications in quantum science and technology. *Phys. Status Solidi A*, 209:1619, 2012.

[33] D. Leibfried, R. Blatt, C. Monroe, and D. Wineland. Quantum dynamics of single trapped ions. *Rev. Mod. Phys.*, 75:281, 2003.

[34] S. D. Bennett and A. A. Clerk. Laser-like instabilities in quantum nano-electromechanical systems. *Phys. Rev. B*, 74:201301, 2006.

[35] D. A. Rodrigues, J. Imbers, and A. D. Armour. Quantum dynamics of a resonator driven by a superconducting single-electron transistor: A solid-state analogue of the micromaser. *Phys. Rev. Lett.*, 98:067204, 2007.

[36] J. Hauss, A. Fedorov, C. Hutter, A. Shnirman, and G. Schön. Single-qubit lasing and cooling at the rabi frequency. *Phys. Rev. Lett.*, 100:037003, 2008.

[37] K. Vahala, M. Herrmann, S. Knünz, V. Batteiger, G. Saathiff, T. W. Hänsch, and Th. Udem. A phonon laser. *Nat. Phys.*, 5:682, 2009.

[38] I. S. Grudinin, H. Lee, O. Painter, and K. J. Vahala. Phonon laser action in a tunable two-level system. *Phys. Rev. Lett.*, 104:083901, 2010.

[39] S. André and et al. Single-qubit lasing in the strong-coupling regime. *Phys. Rev. A*, 82:053802, 2010.

[40] I. Mahboob, K. Nishiguchi, A. Fujiwara, and H. Yamaguchi. Phonon lasing in an electromechanical resonator. *Phys. Rev. Lett.*, 110:127202, 2013.

[41] J. Kabuss, A. Carmele, T. Brandes, and A. Knorr. Optically driven quantum dots as source of coherent cavity phonons: A proposal for a phonon laser scheme. *Phys. Rev. Lett.*, 109:054301, 2012.

[42] N. Lörch, J. Qian, A. A. Clerk, F. Marquardt, and K. Hammerer. Laser theory for optomechanics: limit cycles in the quantum regime. *Phys. Rev. X*, 4:011015, 2014.

[43] K. G. Makris, R. El-Ganainy, D. N. Christodoulides, and Z. H. Musslimani. Beam dynamics in pt symmetric optical lattices. *Phys. Rev. Lett.*, 100:103904, 2008.

[44] Z. H. Musslimani, K. G. Makris, R. El-Ganainy, and D. N. Christodoulides. Optical solitons in pt periodic potentials. *Phys. Rev. Lett.*, 100:030402, 2008.

[45] A. Guo and et al. Observation of pt-symmetry breaking in complex optical potentials. *Phys. Rev. Lett.*, 103:093902, 2009.

[46] C. E. Rüter, K. G. Makris, R. El-Ganainy, D. N. Christodoulides, M. Segev, and D. Kip. Observation of parity–time symmetry in optics. *Nat. Phys.*, 6:192, 2010.

[47] A. Regensburger, C. Bersch, M.-A. Miri, G. Onishchukov, D. N. Christodoulides, and U. Peschel. Parity–time synthetic photonic lattices. *Nature (London)*, 488:167, 2012.

[48] B. Peng and et al. Parity–time-symmetric whispering-gallery microcavities. *Nat. Phys.*, 10:394, 2014.

[49] L. Feng, Z. J. Wong, R.-M. Ma, Y. Wang, and X. Zhang. Single-mode laser by parity-time symmetry breaking. *Science*, 346:972, 2014.

[50] H. Hodaei, M.-A. Miri, M. Heinrich, D. N. Christodoulides, and M. Khajavikhan. Parity-time–symmetric microring lasers. *Science*, 346:975, 2014.

[51] C. Hang, G. Huang, and V. V. Konotop. Pt symmetry with a system of three-level atoms. *Phys. Rev. Lett.*, 110:083604, 2013.

[52] D. Haag, D. Dast, A. Löhle, H. Cartarius, J. Main, and G. Wunner. Nonlinear quantum dynamics in a pt-symmetric double well. *Phys. Rev. A*, 89:023601, 2014.

[53] T. E. Lee and C.-K. Chan. Heralded magnetism in non-hermitian atomic systems. *Phys. Rev. X*, 4:041001, 2014.

[54] H. Jing, S. K. Özdemir, X.-Y. Lü, J. Zhang, L. Yang, and F. Nori. Pt-symmetric phonon laser. *Phys. Rev. Lett.*, 113:053604, 2014.

[55] X.-W. Xu, Y.-X. Liu, C. P. Sun, and Y. Li. Mechanical pt symmetry in coupled optomechanical systems. *Phys. Rev. A*, 92:013852, 2015.

[56] X.-Y. Lü, H. Jing, J.-Y. Ma, and Y. Wu. Pt-symmetry-breaking chaos in optomechanics. *Phys. Rev. Lett.*, 114:253601, 2015.

[57] K. V. Kepesidis, S. D. Bennett, S. Portolan, M. D. Lukin, and P. Rabl. Phonon cooling and lasing with nitrogen-vacancy centers in diamond. *Phys. Rev. B*, 88:064105, 2013.

[58] K. V. Kepesidis, M.-A. Lemonde, A. Norambuena, J. R. Maze, and P. Rabl. Cooling phonons with phonons: acoustic reservoir-engineering with silicon-vacancy centers in diamond. *Phys. Rev. B*, 94:214115, 2016.

[59] K. V. Kepesidis, T. J. Milburn, J. Huber, K. G. Makris, S. Rotter, and P. Rabl. Pt-symmetry breaking in the steady state of microscopic gain–loss systems. *New J. Phys.*, 18:095003, 2016.

[60] L. D. Landau, L. P. Pitaevskii, A. M. Kosevich, and E. M. Lifshitz. *Theory of Elasticity (Third Edition).* Butterworth-Heinemann, Oxford, third edition edition, 1986.

[61] D. F. Walls and G. J. Milburn. *Quantum Optics.* Springer-Verlag, Berlin Heidelberg, 2nd edition, 1994 2008.

[62] P. Lambropoulos and D. Petrosyan. *Fundamentals of Quantum Optics and Quantum Information.* Springer, Berlin, 2007.

[63] M. Schlosshauer. *Decoherence and the quantum-to-classical transition.* Springer-Verlag Berlin Heidelberg, 2007, Corrected Second Printing 2008.

[64] T. J. Milburn and P. Rabl. Advanced quantum optics. Lecture notes: 132.501 - TU Wien, 2013/2014.

[65] D. Lee, K. W. Lee, J. V. Cady, P. Ovartchaiyapong, and A. C. Bleszynski Jayich. Topical review: Spins and mechanics in diamond. arXiv:1609.00418, 2016.

[66] J. R. Maze, A. Gali, E. Togan, Y. Chu, A. Trifonov, E. Kaxiras, and M. D. Lukin. Properties of nitrogen-vacancy centers in diamond: the group theoretic approach. *New J. Phys.*, 13:025025, 2011.

[67] M. W. Doherty, N. B. Manson, P. Delaney, and L. C. L. Hollenberg. The negatively charged nitrogen-vacancy centre in diamond: the electronic solution. *New J. Phys.*, 13:025019, 2011.

[68] J. P. Goss, P. R. Briddon, and M. J. Shaw. Density functional simulations of silicon-containing point defects in diamond. *Phys. Rev. B*, 76:075204, 2007.

[69] C. Hepp, T. Müller, V. Waselowski, J. N. Becker, B. Pingault, H. Sternschulte, D. Steinmüller-Nethl, A. Gali, J. R. Maze, M. Atatüre, and C. Becher. Electronic structure of the silicon vacancy color center in diamond. *Phys. Rev. Lett.*, 112:036405, 2014.

[70] T. A. Abtew, Y. Y. Sun, Bi-Ching Shih, P. Dev, S. B. Zhang, and P. Zhang. Dynamic jahn-teller effect in the nv-center in diamond. *Phys. Rev. Lett.*, 107:146403, 2011.

[71] J. C. Slonczewski. Theory of the dynamical jahn-teller effect. *Phys. Rev.*, 131:1596, 1963.

[72] K.-M. C. Fu, C. Santori, P. E. Barclay, L. J. Rogers, N. B. Manson, and R. G. Beausoleil. Observation of the dynamic jahn-teller effect in the excited states of nitrogen-vacancy centers in diamond. *Phys. Rev. Lett.*, 103:256404, 2009.

[73] I. B. Bersuker. *The Jahn-Teller Effect.* Cambridge University Press, Cambridge, 2006.

[74] G. Davies and M. F. Hamer. Optical studies of the 1.945 ev vibronic band in diamond. *Proc. R. Soc. A*, 348:285, 1976.

[75] P. Treutlein, C. Genes, K. Hammerer, M. Poggio, and P. Rabl. *Cavity Optomechanics.* Springer, Berlin, 2014.

[76] H. J. Mamin, C. T. Rettner, M. H. Sherwood, L. Gao, and D. Rugar. High field-gradient dysprosium tips for magnetic resonance force microscopy. *Appl. Phys. Lett.*, 100:013102, 2012.

[77] Y. Tao, A. Eichler, T. Holzherr, and C. L. Degen. Ultrasensitive mechanical detection of magnetic moment using a commercial disk drive write head. *Nat. Commun.*, 100:12714, 2016.

[78] J. P. Goss, R. Jones, S. J. Breuer, P. R. Briddon, and S. Oberg. The twelve-line 1.682 ev luminescence center in diamond and the vacancy-silicon complex. *Phys. Rev. Lett.*, 77:3041, 1996.

[79] F. Tinkham. *Group Theory and Quantum Mechanics.* Mc-Graw Hill, New York, 2003.

[80] C. Hepp. *Electronic Structure of the Silicon Vacancy Color Center in Diamond.* PhD thesis, University of Saarland, 2014.

[81] K. W. Lee, D. Lee, P. Ovartchaiyapong, J. Minguzzi, J. R. Maze, and A. C. Bleszynski Jayich. Strain coupling of a mechanical resonator to a single quantum emitter in diamond. *Phys. Rev. Applied*, 6:034005, 2016.

[82] P. Rabl. Cooling of mechanical motion with a two-level system: The high-temperature regime. *Phys. Rev. B*, 82:165320, 2010.

[83] C. W. Gardiner and P. Zoller. *Quantum Noise.* Springer-Verlag, Berlin Heidelberg, 2nd edition, 1991 2000.

[84] E. Togan and et al. Quantum entanglement between an optical photon and a solid-state spin qubit. *Nature (London)*, 466:09256, 2010.

[85] Ph. Tamarat and et al. Stark shift control of single optical centers in diamond. *Phys. Rev. Lett.*, 97:083002, 2006.

[86] H. Bernien, L. Childress, L. Robledo, M. Markham, D. Twitchen, and R. Hanson. Two-photon quantum interference from separate nitrogen vacancy centers in diamond. *Phys. Rev. Lett.*, 108:043604, 2012.

[87] J. I. Cirac, R. Blatt, P. Zoller, and W. D. Phillips. Laser cooling of trapped ions in a standing wave. *Phys. Rev. A*, 46:2668, 1992.

[88] L. Giannelli, R. Betzholz, L. Kreiner, M. Bienert, and G. Morigi. Laser and cavity cooling of a mechanical resonator with a nitrogen-vacancy center in diamond. arXiv:1607.06656v2, 2016.

[89] K. Beha, A. Batalov, N. B. Manson, R. Bratschitsch, and A. Leitenstorfer. Optimum photoluminescence excitation and recharging cycle of single nitrogen-vacancy centers in ultrapure diamond. *Phys. Rev. Lett.*, 109:097404, 2012.

[90] P. Siyushev, H. Pinto, M. Vörös, A. Gali, F. Jelezko, and J. Wrachtrup. Optically controlled switching of the charge state of a single nitrogen-vacancy center in diamond at cryogenic temperatures. *Phys. Rev. Lett.*, 110:167402, 2013.

[91] K. Huang and A. Rhys. Theory of light absorption and non-radiative transitions in f-centres. *Proc. R. Soc. A*, 204:406, 1950.

[92] J. F. Poyatos, J. I. Cirac, and P. Zoller. Quantum reservoir engineering with laser cooled trapped ions. *Phys. Rev. Lett.*, 77:4728, 1996.

[93] B. Kraus, H. P. Büchler, S. Diehl, A. Kantian, A. Micheli, and P. Zoller. Preparation of entangled states by quantum markov processes. *Phys. Rev. A*, 78:042307, 2008.

[94] S. G. Schirmer and X. Wang. Stabilizing open quantum systems by markovian reservoir engineering. *Phys. Rev. A*, 81:062306, 2010.

[95] M. Müller, S. Diehl, G. Pupillo, and P. Zoller. Engineered open systems and quantum simulations with atoms and ions. *Adv. Atom. Mol. Opt. Phys.*, 61:1, 2012.

[96] J. I. Cirac, A. S. Parkins, R. Blatt, and P. Zoller. ”dark” squeezed states of the motion of a trapped ion. *Phys. Rev. Lett.*, 70:556, 1993.

[97] D. Kienzler and et al. Quantum harmonic oscillator state synthesis by reservoir engineering. *Science*, 347:6217, 2015.

[98] A. D. Stone M. Devoret A. Roy, Z. Leghtas and M. Mirrahimi. Continuous generation and stabilization of mesoscopic field superposition states in a quantum circuit. *Phys. Rev. A*, 91:013810, 2015.

[99] S. Clark, A. Peng, M. Gu, and S. Parkins. Unconditional preparation of entanglement between atoms in cascaded optical cavities. *Phys. Rev. Lett.*, 91:177901, 2003.

[100] H. Krauter and et al. Entanglement generated by dissipation and steady state entanglement of two macroscopic objects. *Phys. Rev. Lett.*, 107:080503, 2011.

[101] C. A. Muschik, E. S. Polzik, and J. I. Cirac. Dissipatively driven entanglement of two macroscopic atomic ensembles. *Phys. Rev. A*, 83:052312, 2011.

[102] S. Diehl, A. Micheli, A. Kantian, B. Kraus, H. P. Buchler, and P. Zoller. Quantum states and phases in driven open quantum systems with cold atoms. *Nat. Phys.*, 4:878, 2008.

[103] H. Weimer, M. Muller, I. Lesanovsky, P. Zoller, and H. P. Buchler. A rydberg quantum simulator. *Nat. Phys.*, 6:382, 2010.

[104] J. T. Barreiro and et al. An open-system quantum simulator with trapped ions. *Nature (London)*, 470:486, 2011.

[105] P. Rabl, A. Shnirman, and P. Zoller. Generation of squeezed states of nanomechanical resonators by reservoir engineering. *Phys. Rev. B*, 70:205304, 2004.

[106] A. Kronwald, F. Marquardt, and A. A. Clerk. Arbitrarily large steady-state bosonic squeezing via dissipation. *Phys. Rev. A*, 88:063833, 2013.

[107] E. E. Wollman and et al. Quantum squeezing of motion in a mechanical resonator. *Science*, 349:6251, 2015.

[108] Y.-D. Wang and A. A. Clerk. Reservoir-engineered entanglement in optomechanical systems. *Phys. Rev. Lett.*, 110:253601, 2013.

[109] H. Tan, G. Li, and P. Meystre. Dissipation-driven two-mode mechanical squeezed states in optomechanical systems. *Phys. Rev. A*, 87:033829, 2013.

[110] A. Tomadin, S. Diehl, M. D. Lukin, P. Rabl, and P. Zoller. Reservoir engineering and dynamical phase transitions in optomechanical arrays. *Phys. Rev. A*, 86:033821, 2012.

[111] E. R. MacQuarrie, T. A. Gosavi, N. R. Jungwirth, S. A. Bhave, and G. D. Fuchs. Mechanical spin control of nitrogen-vacancy centers in diamond. *Phys. Rev. Lett.*, 111:227602, 2013.

[112] P. Ovartchaiyapong, K. W. Lee, B. A. Myers, and A. C. Bleszynski Jayich. Dynamic strain-mediated coupling of a single diamond spin to a mechanical resonator. *Nat. Commun.*, 5(4429), 2014.

[113] A. Barfuss, J. Teissier, E. Neu, A. Nunnenkamp, and P. Maletinsky. Strong mechanical driving of a single electron spin. *Nat. Phys.*, 11:820, 2015.

[114] S. Meesala and et al. Enhanced strain coupling of nitrogen-vacancy spins to nanoscale diamond cantilevers. *Phys. Rev. Applied*, 5:034010, 2016.

[115] D. A. Golter, T. Oo, M. Amezcua, K. A. Stewart, and H. Wang. Optomechanical quantum control of a nitrogen-vacancy center in diamond. *Phys. Rev. Lett.*, 116:143602, 2016.

[116] P. Rabl, P. Cappellaro, M. V. G. Dutt, L. Jiang, J. R. Maze, and M. D. Lukin. Strong magnetic coupling between an electronic spin qubit and a mechanical resonator. *Phys. Rev. B*, 79:041302, 2009.

[117] O. Arcizet, V. Jacques, A. Siria, P. Poncharal, P. Vincent, and S. Seidelin. A single nitrogen-vacancy defect coupled to a nanomechanical oscillator. *Nat. Phys.*, 7:879, 2011.

[118] S. Kolkowitz and et al. 0 0 report coherent sensing of a mechanical resonator with a single-spin qubit. *Science*, 335:1603, 2012.

[119] K. D. Jahnke and et al. Electron–phonon processes of the silicon-vacancy centre in diamond. *New J. Phys.*, 17:043011, 2015.

[120] C. A. Klein and G. F. Cardinal. *Diamond and Related Materials*, 2:918, 1993.

[121] L.-M. Duan, G. Giedke, J. I. Cirac, and P. Zoller. Inseparability criterion for continuous variable systems. *Phys. Rev. Lett.*, 84:2722, 2000.

[122] R. Simon. Peres-horodecki separability criterion for continuous variable systems. *Phys. Rev. Lett.*, 84:2726, 2000.

[123] M. J. Hartmann and M. B. Plenio. Steady state entanglement in the mechanical vibrations of two dielectric membranes. *Phys. Rev. Lett.*, 101:200503, 2008.

[124] C. M. Bender and S. Boettcher. Real spectra in non-hermitian hamiltonians having pt symmetry. *Phys. Rev. Lett.*, 80:5243, 1998.

[125] C. M. Bender. Making sense of non-hermitian hamiltonians. *Rep. Prog. Phys.*, 70:947, 2007.

[126] H. Ramezani, T. Kottos, R. El-Ganainy, and D. N. Christodoulides. Unidirectional nonlinear pt-symmetric optical structures. *Phys. Rev. A*, 82:043803, 2010.

[127] C. Gardiner. *Stochastic Methods.* Berlin: Springer, 4th edition, 2009.

[128] H. Schomerus. Quantum noise and self-sustained radiation of pt-symmetric systems. *Phys. Rev. Lett.*, 104:233601, 2010.

[129] G. S. Agarwal and Kenan Qu. Spontaneous generation of photons in transmission of quantum fields in pt-symmetric optical systems. *Phys. Rev. A*, 85:031802, 2012.

[130] B. He, S.-B. Yan, J. Wang, and M. Xiao. Quantum noise effects with kerr-nonlinearity enhancement in coupled gain-loss waveguides. *Phys. Rev. A*, 91:053832, 2015.

[131] N. V. Alexeeva, I. V. Barashenkov, K. Rayanov, and S. Flach. Actively coupled optical waveguides. *Phys. Rev. A*, 89:013848, 2014.

[132] B. Peng and et al. Loss-induced suppression and revival of lasing. *Science*, 346:328, 2014.

[133] M. Brandstetter and et al. Reversing the pump dependence of a laser at an exceptional point. *Nat. Commun.*, 5:4034, 2014.

[134] N. Lazarides and G. P. Tsironis. Gain-driven discrete breathers in pt-symmetric nonlinear metamaterials. *Phys. Rev. Lett.*, 110:053901, 2013.

[135] M. C. Cross and P. C. Hohenberg. Pattern formation outside of equilibrium. *Rev. Mod. Phys.*, 65:851, 1993.

[136] O. Vazquez-Candanedo, J. C. Hernández-Herrejón, F. M. Izrailev, and D. N. Christodoulides. Gain- or loss-induced localization in one-dimensional pt-symmetric tight-binding models. *Phys. Rev. A*, 89:013832, 2014.

[137] I. V. Barashenkov, L. Baker, and N. V. Alexeeva. Pt-symmetry breaking in a necklace of coupled optical waveguides. *Phys. Rev. A*, 87:033819, 2013.

About the author

PERSONAL INFORMATION

Kosmas Kepesidis

Erich-Klausener-Str. 11, 40474 Düsseldorf (Germany)
+4915158071941
cosmasquantum@gmail.com
https://www.linkedin.com/in/kosmas-kepesidis-78697996

WORK EXPERIENCE

1 Nov 2016–Present

Professional | Forensics

Deloitte Deutschland, Düsseldorf (Germany)

May 2012–31 Oct 2016

Research Assistant | Physics

Technische Universität Wien, Vienna (Austria)

Jan 2012–Apr 2012

Research Assistant | Physics

Technische Universität München, Munich (Germany)

EDUCATION AND TRAINING

Jan 2013–Present

Doctoral Degree (Dr. rer. nat.) in Technical Physics

EQF level 8

Technische Universität Wien, Vienna (Austria)

Oct 2009–Sep 2011

Master's Degree (M.Sc.) in Physics

EQF level 7

Ludwig-Maximilians-Universität München, Munich (Germany)

Oct 2004–Jan 2009

Bachelor's Degree (B.Sc.) in Physics

EQF level 6

University of Crete, Heraklion (Greece)

ADDITIONAL INFORMATION

Publications

- Cooling phonons with phonons: acoustic reservoir-engineering with silicon-vacancy centers in diamond, K. V. Kepesidis, M.-A. Lemonde, A. Norambuena, J. R. Maze, P. Rabl, Phys. Rev. B 94, 214115 (2016), American Physical Society

- PT-symmetry breaking in the steady state of microscopic gain-loss systems, K. V. Kepesidis, T. J. Milburn, J. Huber, K. G. Makris, S. Rotter, P. Rabl, New Journal of Physics 18, 095003 (2016), IOP Publishing

- Phonon cooling and lasing with nitrogen-vacancy centers in diamond, K. V. Kepesidis, S. D. Bennett, S. Portolan, M. D. Lukin and P. Rabl, Phys. Rev. B 88, 064105 (2013), American Physical Society

- Bose-Hubbard model with localized particle losses, K. V. Kepesidis and M. J. Hartmann, Phys. Rev. A 85, 063620 (2012), American Physical Society